EVALUATION OF PROMPT GAMMA-RAY DATA AND NUCLEAR STRUCTURE OF NIOBIUM-94 WITH STATISTICAL MODEL CALCULATIONS

DISSERTATION

Presented in Partial Fulfillment of the Requirements for the Degree Doctor of

Philosophy in the Graduate School of the Ohio State University

By

Danyal Turkoglu, M.S.

Graduate Program in Nuclear Engineering

The Ohio State University

2014

Dissertation Committee:

Professor Lei Cao, Advisor

Professor Tunc Aldemir

Professor Tom Blue

Dr. Shamsuzzoha Basunia

ABSTRACT

Precise knowledge of prompt γ-ray intensities following neutron capture is critical for elemental and isotopic analyses, homeland security, modeling nuclear reactors, etc. A recently-developed database of prompt γ-ray production cross sections and nuclear structure information in the form of a decay scheme, called the Evaluated Gamma-ray Activation File (EGAF), is under revision. Statistical model calculations are useful for checking the consistency of the decay scheme, providing insight on its completeness and accuracy. Furthermore, these statistical model calculations are necessary to estimate the contribution of continuum γ-rays, which cannot be experimentally resolved due to the high density of excited states in medium- and heavy-mass nuclei. Decay-scheme improvements in EGAF lead to improvements to other databases (Evaluated Nuclear Structure Data File, Reference Input Parameter Library) that are ultimately used in nuclear-reaction models to generate the Evaluated Nuclear Data File (ENDF).

Gamma-ray transitions following neutron capture in ^{93}Nb have been studied at the cold-neutron beam facility at the Budapest Research Reactor. Measurements have been performed using a coaxial HPGe detector with Compton suppression. Partial γ-ray production capture cross sections at a neutron velocity of 2200 m/s have been deduced relative to that of the 255.9-keV transition after cold-neutron capture by ^{93}Nb. With the measurement of a niobium chloride target, this partial cross

section was internally standardized to the cross section for the 1951-keV transition after cold-neutron capture by ^{35}Cl. The resulting (0.1377 ± 0.0018) barn (b) partial cross section produced a calibration factor that was 23% lower than previously measured for the EGAF database. The thermal-neutron cross sections were deduced for the ^{93}Nb(n,γ)^{94m}Nb and ^{93}Nb(n,γ)^{94g}Nb reactions by summing the experimentally-measured partial γ-ray production cross sections associated with the ground-state transitions below the 396-keV level and combining that summation with the contribution to the ground state from the quasi-continuum above 396 keV, determined with Monte Carlo statistical model calculations using the DICEBOX computer code. These values, σ_m and σ_0, were (0.83 ± 0.05) b and (1.16 ± 0.11) b, respectively, and found to be in agreement with literature values. Comparison of the modeled population and experimental depopulation of individual levels confirmed tentative spin assignments and suggested changes where imbalances existed.

Dedicated to my family

ACKNOWLEDGMENTS

First and foremost, I would like to thank my advisor, Professor Lei R. Cao, for his guidance throughout my graduate career at the Ohio State University. We came to the university at the same time and accomplished a lot, including the design and construction of a new neutron beam facility. His technical expertise and many ideas have made my experience fulfilling.

I would like to thank Dr. Shamsuzzoha Basunia for his kind mentoring and serving on my committee as an external member – and Dr. Aaron Hurst for his assistance and guidance. I would also like extend my appreciation to Dr. Richard Firestone for funding my visit to Lawrence Berkeley National Laboratory and giving me the opportunity to work on this project. I am grateful to Dr. László Szentmiklósi and Dr Boglárka Maróti of the Hungarian Academy of Sciences Centre for Energy Research for conducting the measurements at the Budapest Research Reactor.

Lastly, I would like to thank Professor Tunc Aldemir and Professor Thomas Blue for their time and effort participating in my committee. I would also like to thank the Nuclear Regulatory Commission for supporting this research through fellowships.

VITA

1986 .... Born in Merced, CA USA

2005 .... Rutherford High School

2009 .... B.S. Chemical Engineering,
University of Florida

2011 .... M.S. Nuclear Engineering,
The Ohio State University

2009-2013 .... NRC Fellow,
The Ohio State University

2013-present .... Graduate Research Assistant,
The Ohio State University

PUBLICATIONS

D Turkoglu, S Basunia, A Hurst, R Firestone, L Szentmiklosi, L Cao. "**^{93}Nb thermal neutron capture cross section from prompt γ-ray intensities**," in *Transactions of the American Nuclear Society*. Anaheim, CA, vol. 111, pp 560-563, Nov. 2014.

J Qiu, L Cao, P Mulligan, D Turkoglu, S Nagpure, C Marcello, A Co. "**The Potential of Using Li-Ion Batteries for Radiation Detection**," *IEEE Transactions on Nuclear Science*, vol. 60, no. 2, pp. 662-667, 2013.

D Turkoglu, S Glover, H Spitz, L Cao. "**Applying Method of Integral Thermal Neutron Cross-Section Measurement Using Activated Prompt Gamma**

Rays to Non-1/v Isotopes," in *Transactions of the American Nuclear Society*, Washington, DC, vol 109, pp 118-120, Nov. 2013.

D Turkoglu, L Cao. "**A Preliminary Study of ^{157}Gd Thermal Neutron Capture Cross Section with Activated Prompt Gamma Rays**," in *Transactions of the American Nuclear Society*, Atlanta, GA, vol. 108, pp. 270-273, June 2013.

D Turkoglu, L Cao, Rod Lewandowski. "**A low-cost neutron radiography device**," *Physics Procedia*, vol. 43, pp. 54-65, 2013.

D Turkoglu, J Burke, R Lewandoswki, L Cao. "**Characterization of a New External Neutron Beam Facility at The Ohio State University**," in *Journal of Radioanalytical and Nuclear Chemistry*, vol. 291, no. 2, pp. 321-327, 2012.

P Mulligan, L Cao, D Turkoglu. "**A multi-detector, digitizer based neutron depth profiling deice for characterizing thin film materials**," *Review of Scientific Instruments*, vol. 83, no. 7, pp. 073303, 2012.

R Lewandowski, L Cao, D Turkoglu "**Noise Evaluation of a digital neutron imaging device**," *Nuclear Instruments and Methods in Physics Research Section A: Accelerators, Spectrometers, Detectors and Associated Equipment*, vol. 674, pp. 46-50, 2012.

D Turkoglu, P Kandlakunta, P Mulligan, L Cao, J Zhang, BT Sang, RG Downing. "**Development of a Neutron Depth Profiling Facility for Characterizing Advanced Reactor Materials**," in *Transactions of the American Nuclear Society*, Hollywood, FL, vol. 104, pp. 302-303, June 2011.

D Turkoglu, J Strah, P Kandlakunta, L Cao. "**Development of an External Neutron Beam Facility at The Ohio State University**," in *Transactions of the American Nuclear Society*, Las Vegas, NV, vol. 103, pp. 231-232, Nov. 2010.

FIELDS OF STUDY

Major Field: Nuclear Engineering

TABLE OF CONTENTS

LIST OF TABLES

LIST OF FIGURES

xvi

LIST OF ACRONYMS

BA   Brink-Axel
BSFG   Back-Shifted Fermi Gas
CS   Capture state
CTF   Constant Temperature Formula
EGAF   Evaluated Gamma-ray Activation File
EGLO   Enhanced Generalized Lorentzian
ENDF   Evaluated Nuclear Data File
ENSDF   Evaluated Nuclear Data Structure File
FWHM   Full-width at half maximum
GDER   Giant dipole electric resonance
GS   Ground state
HPGe   High-purity germanium
ICC   Internal conversion coefficient
IAEA   International Atomic Energy Agency
LeGe   Low-energy germanium
LD   Level density
PGNAA   Prompt Gamma-ray Neutron Activation Analysis
PGNAM   Prompt γ-ray Neutron Activation Method
PSF   Photon Strength Function
RIPL   Reference Input Parameter Library

LIST OF SYMBOLS

A_γ	Peak area
D_0	Average level spacing
ϵ	Detection efficiency
E_{crit}	Critical energy
E_γ	γ-ray energy
E_L	Level energy
E_n	Neutron energy
f^{XL}	Photon strength function
F_γ	γ-ray self-absorption correction factor
Γ	Partial radiation width
Γ_0	Total radiative width
J	Spin
π	Parity
J^π	Spin-parity
J^π_{CS}	Spin-parity of capture state
ρ	Level density
P_γ	γ-ray emission probability
$P(GS)$	Probability of direct feeding of ground state from the continuum
S_n	Neutron-separation energy
σ	Cross section
σ_0	Thermal neutron capture cross section
σ_m	Thermal neutron capture cross section for $^{93}\mathrm{Nb}(\mathrm{n},\gamma)^{94m}\mathrm{Nb}$
σ_γ	Partial γ-ray production cross section
XL	Multipolarity of transition

CHAPTER 1

INTRODUCTION

Slow-neutron capture produces prompt γ-rays with energies characteristic of nuclear structure. Prompt Gamma-ray Neutron Activation Analysis (PGNAA) exploits these unique signatures for nondestructive elemental and isotopic analysis. Until recently, the lack of a reliable neutron-capture γ-ray database limited the accuracy in applying the PGNAA technique. In the late 1990s, precise thermal-neutron capture γ-ray cross sections σ_γ were measured for all elements with Z=1-83, 90, and 92, except for He and Pm, with guided neutron beams at the Budapest Research Reactor [7]. These comprehensive measurements led to an International Atomic Energy Agency (IAEA) Coordinated Research Project (CRP) to develop a database of the σ_γ data, evaluated together with additional information from literature, called the Evaluated Gamma-ray Activation File (EGAF) [8]. EGAF organizes the data in a decay scheme following the format of the Evaluated Nuclear Structure Data File (ENSDF) [9], and is, thus, the synthesis of nuclear structure from ENSDF and experimental γ-ray energies and intensities intended for application purposes. The challenge in creating the database is that the decay schemes are only complete for light-mass elements (with atomic number $Z < 20$). Complex γ-ray spectra arise in measurement of medium- and heavy-mass elements, which, in most cases, have hundreds of characteristic γ-rays for each naturally-occurring isotope. These nuclei, with densities of states that increase with excitation energy, have level spacings at high-excitation energies that are below

what the best-resolution detectors can resolve. Since these continuum γ-rays cannot be experimentally resolved, a statistical model is used to estimate their contributions to the decay scheme. Additionally, only data for the isotopes with the largest cross sections and/or abundances could be obtained with natural targets. Thus, a pressing need exists for validation and revision of EGAF through measurements with enriched target isotopes and statistical modeling of γ-ray cascades for validation. Along with revised, more-accurate γ-ray data libraries – the process allows for optimization of capture-state spin distributions and improved nuclear structure information [10] that will be disseminated to ENSDF and the Reference Input Parameter Library (RIPL) [11]. ENSDF and RIPL are used in nuclear-reaction calculations that generate the Evaluated Nuclear Data File (ENDF) [12]. Ultimately, this benefits a variety of fields from analytical chemistry to national security applications and modeling of nuclear reactors [13].

The traditional methods for determining the total radiative thermal neutron-capture cross section, σ_0, include pile oscillation and time-of-flight transmission, both of which require precise knowledge of the neutron spectrum, and activation analysis, which requires an accurate decay-scheme normalization. Large corrections due to epithermal (1 eV to 10 keV) neutrons are typically necessary to determine σ_0. The EGAF database can be also used to determine σ_0, if the decay scheme is complete, as $\sigma_0 = \sum \sigma_\gamma(GS) = \sum \sigma_\gamma(CS)$ for transitions feeding the ground state (GS) or de-exciting the capture state (CS). For those with incomplete decay schemes, the feeding from continuum γ-rays must be accounted for in order to determine σ_0 from the σ_γ data. The continuum feeding can be determined with statistical model calculations using the Monte Carlo computer code DICEBOX [14], as first demonstrated for the palladium isotopes by Krtička et al [15]. DICEBOX generates simulated neutron capture decay schemes based on nuclear level density and photon strength

function models. The simulated intensities of transitions populating low-lying levels are normalized to the experimental cross sections de-exciting those levels in order to determine the unobserved cross section feeding the ground state. The combination of this simulated feeding of the ground state and the experimentally-observed cross section feeding the ground state gives σ_0. The statistical uncertainty in the relative continuum feeding, arising from Porter-Thomas fluctuations in the partial radiation widths [16], is higher than the precision of an experiment, but the measured cross section from the low-lying levels dominate the total cross section. The sensitivity of this technique was shown to be comparable to those of other methods of cross section measurement for the palladium isotopes, even when using an incomplete decay scheme with only a few experimentally-observed transitions [15]. The method, which may be referred to as the Prompt γ-ray Neutron Activation Method (PGNAM), has since been applied to bismuth [17], potassium [18], tungsten [19], europium [20], gadolinium [21] and rhenium [22] isotopes. Of these nuclei, $^{152,154}_{63}$Eu and $^{186}_{75}$Re are the only odd-odd nuclei (with an odd number protons and odd number of neutrons); with these studies and this work with odd-odd $^{94}_{41}$Nb, the overall trend can be established for statistical modeling of γ-rays from neutron capture states of odd-odd nuclei using DICEBOX.

Niobium alloys, such as niobium-bearing zirconium (Zr-1Nb) [23][24], are used in nuclear reactors as fuel cladding material due to high corrosion and radiation resistance [25][26]. Additionally, a novel, accident-tolerant fuel incorporates a high-thermal conductivity material, such as niobium, as discs inside annular fuel [27]. The focus of this work is applying the methodology used for measuring and evaluating prompt γ-ray data for the EGAF to the niobium element. Enriched samples were not needed for this task since niobium is a monoisotope, ^{93}Nb, with a medium-mass ($Z = 41$). The niobium σ_0 has been previously measured with the pile oscillator and

activation techniques; the currently accepted value is 1.15±0.05 barns (b) [28]. Niobium neutron capture reaction ^{93}Nb$(n, \gamma)^{94m,g}$Nb produces a metastable state ^{94m}Nb, with a half-life of 6.263 minutes, that is the lowest-lying state with an excitation energy of 40.9 keV above the ground state and the ground state, ^{94}Nb, with a half-life of 20,300 years [6].

The ^{94}Nb nucleus has received considerable theoretical and experimental consideration. The level scheme of ^{94}Nb has been built based on the reactions listed in the following:

- ^{93}Nb$(n, \gamma)^{94}$Nb:

    - Thermal neutron capture [29][30][31][8],

    - Resonance neutron capture [32],

    - Primary γ-ray measurement [33];

- ^{93}Nb$(d, p)^{94}$Nb [34];

- ^{94}Zr$(p, n\gamma)^{94}$Nb [35][36];

- ^{82}Se$(^{19}Fe, \alpha 3n\gamma)^{94}$Nb [37].

In the decay scheme, only the ground state and first excited-state have firm spin (J) and parity (π) assignments, while the other levels remain tentatively or ambiguously assigned. Thus, RIPL recommends that the decay scheme is complete only for the first excited-state of ^{94}Nb.

1.1 Scope

With very weak γ-ray intensities, a 4.5 gram (g) niobium oxide (Nb$_2$O$_5$) sample was used for the γ-ray peak list in the previous EGAF measurement [38]. Comparison

of normalized intensities of EGAF data to the ENSDF data, which is based on a measurement of a 50 microgram metal target [31], revealed that the low-energy γ-ray intensities were lower than the ESNDF data. The likely explanation was that γ-ray self-absorption, which is difficult to accurately correct for in large-mass samples, caused the discrepancies in the low-energy EGAF data. Consequently, the ^{94}Nb prompt γ-ray spectrum of Nb_2O_5 sample – with a small-mass for less significant γ-ray self-absorption – was measured for this work with a cold-neutron beam at the Budapest Research Reactor. Additionally, niobium chloride ($NbCl_5$) was measured for the standardization of the ^{94}Nb σ_γ relative to chlorine. After creation of a new EGAF, the DICEBOX statistical model code was used to check the consistency of the decay scheme and γ-ray intensities. This work expands on previous evaluations of the ^{94}Nb nuclear structure with DICEBOX used to confirm/find the J^π assignment for individual levels such that the modeled population determined with the statistical model matches the experimentally-determined depopulation of the level. Finally, the cross section of the metastable state, σ_m, and the thermal neutron-capture cross section, σ_0, were calculated from the experimental data of transitions feeding the metastable and ground states and the contribution from the continuum γ-rays.

1.2   Dissertation Overview

Chapter 2 provides the background on the problem analyzed. This begins with the theoretical background about neutron capture and nuclear decay via γ-ray emission. The second part introduces prompt γ-ray neutron activation analysis (PGNAA) and its history of prompt γ-ray data. The last part chronicles the ^{94}Nb nuclear structure evaluation. Chapter 3 provides an overview of the methodology used in this work, including: spectrum analysis, internal standardization and statistical model calculations. Chapter 4 describes the experiments, data analysis and statistical model

calculations. The results are also provided throughout this chapter. Lastly, Chapter 5 provides the conclusions of this work and the recommended future work.

CHAPTER 2

BACKGROUND

This chapter addresses the background relevant to this work. The first section addresses the theoretical background pertaining to compound nucleus formation as a result of slow-neutron capture and its subsequent decay via γ-ray emission. The next section introduces prompt γ-ray neutron activation analysis (PGNAA) and its history of prompt γ-ray data. The last section chronicles the ^{94}Nb nuclear structure evaluation.

2.1 Theory

2.1.1 Neutron Capture

A nucleus that absorbs a neutron forms a compound nucleus with an excitation energy equal to the binding energy (S_n) plus the kinetic energy of the neutron, E_n. Slow neutrons (with energies in the meV range) carry negligible momentum and, thus, form the capture state with a well-defined energy value that is practically equal to the binding energy. With the compound nucleus at high-excitation energy, the most likely decay mechanism is via statistical emission of γ-rays with energies up to the neutron separation energy. The process of neutron capture and prompt γ-ray decay of the compound nucleus is illustrated in Figure 2.1.

The cross section, σ, characterizes the probability of a reaction with the unit barn,
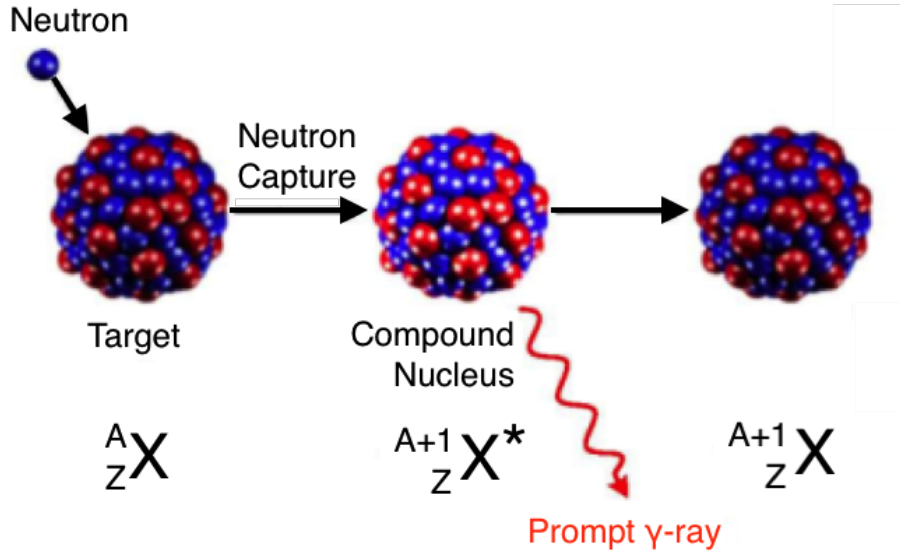
Figure 2.1: Illustration of prompt γ-ray emission following neutron capture

where 1 barn $= 10^{-24}$ cm^2. Whereas elastic scattering of thermal neutrons is close to the actual geometric cross section of a nucleus, capture reactions may differ by several orders of magnitude in either direction [39]. The cross section depends on the incident neutron energy, as shown for the ^{93}Nb(n,γ)^{94}Nb reaction in Fig. 2.2. The behavior of the cross sections in the slow-neutron region typically follows an inverse proportionality to the neutron velocity v – the so-call "1/v law" where $\sigma(v) = \sigma_0 \dfrac{v_0}{v}$ or equivalently, $\sigma(E) = \sigma_0 \sqrt{\dfrac{E_0}{E}}$. Since these neutron energies are the most important due to their higher reaction rates, the capture cross sections for the nuclides are tabulated for monochromatic neutrons with a 2200 m/s velocity – or equivalently, 0.0253 eV of kinetic energy – and called the thermal neutron capture cross sections denoted by σ_0.

8
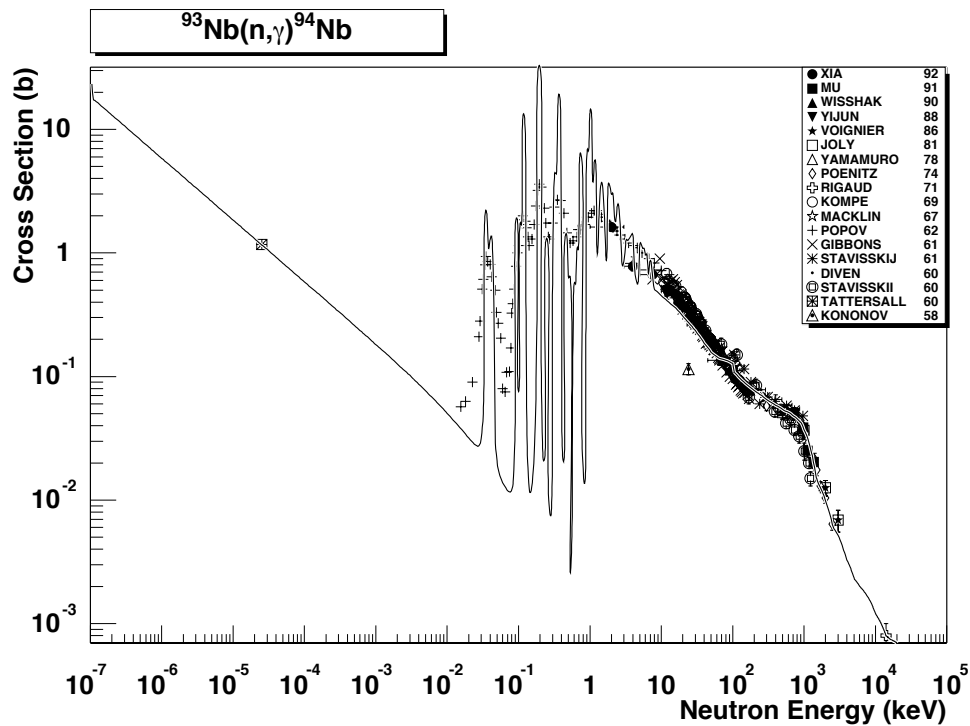
Figure 2.2: ^{93}Nb differential neutron capture cross section [2]

2.1.2 Gamma-ray Decay

Gamma-ray decay occurs when a nucleus in an excited state releases excess energy via emission of electromagnetic radiation, *i.e.*, a photon. Gamma-ray transitions start at a high-lying excited state and feed a lower-lying state of the nucleus. The typical decay of the compound nuclear takes place on the order 10^{-16} seconds with the nucleus reaching its ground state in about 10^{-12} to 10^{-9} seconds with the emission of 2-4 gamma rays in a cascade. The gamma-ray cascade concludes when all excess energy of the excited nucleus is released. Gamma-rays are called prompt if decay times

following neutron capture are much shorter than the resolving time of the detection system. Since the detection of γ-rays with defined energies is useful for identifying elements, the partial γ-ray production cross section, σ_γ, is useful for characterizing the production of a γ-ray with energy E_γ for one atom of the examined isotope. The σ_γ is defined as

$$\sigma_\gamma = \theta \sigma_0 P_\gamma, \tag{2.1}$$

where θ is the natural abundance of the given isotope, in the element of interest, σ_0 is the isotopic capture cross section and P_γ is the emission probability of the γ-ray with energy E_γ.
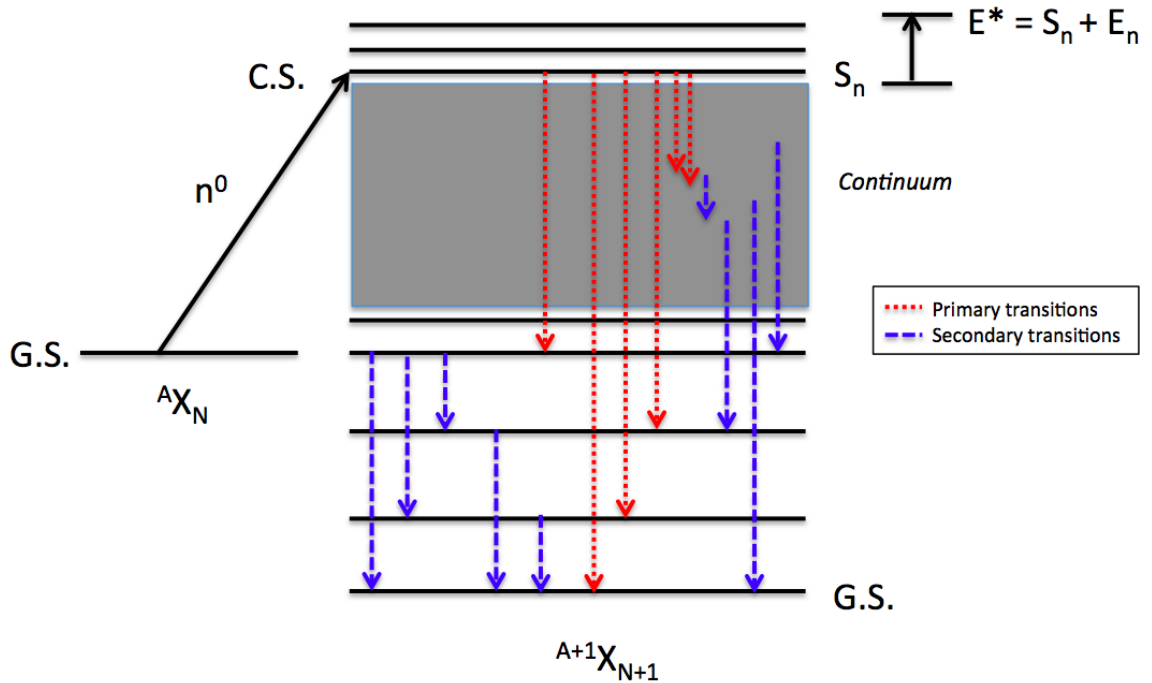
Figure 2.3: Illustration of the primary and secondary γ-ray transitions

The γ-ray transitions can be classified into two categories: 1) primary transitions that depopulate the capture state and 2) secondary transitions between levels below the capture state. These are depicted in Figure 2.3, where a target nucleus $^{A}X_N$ at its ground state (G.S.) absorbs a neutron n to form the capture state (C.S.) of nucleus $^{A+1}X_{N+1}$ at high-excitation energies and de-excites to its ground state via γ-ray emissions. The gray box represents the continuum where individual levels are indistinguishable due to high densities of levels. Another important category for γ-ray transitions is that for ground state transitions. From the conservation of energy law, the sum of emission probabilities P_γ for all primary and ground-state transitions must be unity:

$$\sum_i P_{\gamma,i} = 1. \tag{2.2}$$

Since the emission probability P_γ is related to the σ_γ, this can be written alternatively as:

$$\theta \sum_i P_{\gamma,i} = \sigma. \tag{2.3}$$

Primary and secondary transitions are difficult to identify due to the complexity of γ-ray spectra, making these tests really only applicable in practice to light isotopes. A more useful test is the binding-energy test, which is based on the principle that the sum of all γ-ray energies weighted by their emission probabilities must be equal to the binding energy S_n for the nucleus [39]:

$$S_n = \sum_i E_{\gamma,i} P_{\gamma,i} \tag{2.4}$$

$$\sigma = \theta \sum_i \frac{E_{\gamma,i}}{S_n} \sigma_{\gamma,i}. \tag{2.5}$$

A particularly useful case of the binding-energy test is for identifying cascades with two γ-rays with total energy, corrected for nucleus recoil, that is equal to S_n. Additionally, the sum of all γ-ray emission probabilities, $\sum_i P_{\gamma,i}$, yields the *multiplicity*, or average number of transitions, in the de-excitation of the compound nucleus.

The laws of energy and momentum conservation apply to γ-ray emission as shown in Equation 2.6, where E_i is the initial excited state, E_f is the final excited state, E_R is the nucleus recoil energy, and $\vec{p}_R$ and $\vec{p}_\gamma$ are the momenta of the recoiling nucleus and γ-ray, respectively.

$$E_i = E_f + E_\gamma + E_R \tag{2.6}$$

$$0 = \vec{p}_R + \vec{p}_\gamma \tag{2.7}$$

The transition energy, ΔE, is the energy difference in the initial and final states, $E_i - E_f$. The conservation laws lead to the γ-ray energy, E_γ, for a transition energy given in Equation 2.8. The second term is the correction for nucleus recoil, where m is the mass of the recoiling nucleus.

$$\Delta E = E_\gamma + \frac{E_\gamma^2}{2mc^2} \tag{2.8}$$

Another important consideration in γ-ray emission is that the initial and final states of the nucleus have defined angular momentum and parity. Thus, the photon connecting the two states must conserve both parity and angular momentum. Each photon has a definite parity and carries an exact integer number of angular momentum units ($\hbar$). The conservation of parity and angular momentum have different effects on the possible properties of the emitted photon. The change in angular momentum is $l = \Delta I = (I_i - I_f)\hbar$, with $I_i\hbar$ and $I_f\hbar$ being the angular momenta of initial and final states of the nucleus. The transition in which $\Delta I = 0$ is forbidden because

each photon must carry at least one unit of angular momentum. While the emitted photon should have a minimum intrinsic spin of $l\hbar$ units to connect the two nucleus states, the coupling rules for angular momenta allow the photon to carry away up to a maximum of $l = (I_i + I_f)\hbar$ units. Therefore, the angular momentum carried by the photon, given known spins of the initial and final states of the nucleus, can take a value in the range $|(I_i - I_f)|\hbar \leq l \leq |(I_i - I_f)|\hbar$. The *multipolarity* of the photon is the quantification of the angular momentum carried by the photon. The smallest change $l = |(I_i - I_f)|\hbar$ is usually observed [40].

An odd-A target nucleus like ^{93}Nb has a half-integer initial spin I. The addition of a neutron via neutron capture yields two possible spin states for the capture state: $I + 1/2$ and $I - 1/2$. The values of $\sigma_\gamma(+)$ and $\sigma_\gamma(-)$ are the 2200 m/s radiative neutron capture cross sections due to positive-energy resonances with spins $I + 1/2$ and $I - 1/2$, respectively [28]. Thus, the apportionment of these two possible spin states $I + 1/2$ and $I - 1/2$ are:

$$J_{CS}(I - 1/2) = \frac{\sigma(-)}{\sigma(-)\sigma(+)} \tag{2.9}$$

$$J_{CS}(I + 1/2) = \frac{\sigma(+)}{\sigma(-)\sigma(+)}. \tag{2.10}$$

Negative-energy (with respect to the neutron separation energy) bound resonances can also contribute to both these spin states, represented by $\sigma_\gamma(B)$. In this case, the experimental capture cross section $\sigma_\gamma(exp.)$ satisfies the relation

$$\sigma_\gamma(exp.) = \sigma(-) + \sigma(+) + \sigma_\gamma(B). \tag{2.11}$$

At high-excitation levels, the γ-ray decay probabilities behave statistically, as evident by the fluctuations in partial radiative widths, $\Gamma_{i\gamma f}$, that characterize the probabilities of γ-ray decay with an energy E_γ. The Porter-Thomas distribution [16] describes the $\Gamma_{i\gamma f}$ as a Gaussian distribution with the mean value given as

$$\langle \Gamma_{if} \rangle = \frac{f^{XL}(E_\gamma) E_\gamma^{2L+1}}{\rho(E_i, J_i^{\pi_i})}. \tag{2.12}$$

Here, $\rho(E_i, J_i^{\pi i})$ is the level density (LD) near the initial level i with spin-parity J^{π} and $f^{XL}(E_{\gamma})$ is the photon strength function (PSF) for a transition of type X and multipolarity L to the final level f.

Normally, unique level spin cannot be assigned on the basis of (n,γ) data with energies and intensities obtained from a single detector. However, the multipolarity of a transition, which allows the determination of level spin, can be ascertained from the angular distribution of radiation. The angular distribution of γ-rays must be isotropic since the emitting nuclei are randomly oriented. Anisotropic angular distributions can only be observed when preferred nuclear orientation is established prior to photon emission. Two techniques to establish this condition rely on angular correlation with either an external magnetic field or another particle or photon emitted in sequentially with the same nucleus [40]. The conceptually-simplest technique for observation of angular correlations is to measure the angular distribution of radiation from an excited nucleus relative to an external, applied, magnetic field, which provides the reference axis. The nuclear orientation in the magnetic field is maintained by cooling the sample to a temperature, typically, on the order of 10 mK. The more common technique for observing angular correlations is based on detecting the relative direction of coincident radiation by detecting the direction of radiation that feeds an excited state and then observing the angular distribution relative to that direction. The process could be with a γ-ray from a higher-lying excited state or an α or β particle from a parent nucleus. This first photon or particle, which provides the reference axis, must also unequally populate the magnetic substates of the intermediate state so that there is an anisotropic angular distribution [40]. These techniques identify the order of the multipolarity (i.e., dipole, quadrapole, etc.), but leave ambiguity about the parity of the radiation – whether it was produced by an electric or a magnetic transition in the nucleus. The parity of the radiation corresponds to the plane of polarization of the

electromagnetic radiation, which can be determined from knowledge of the direction of the plane of the electric vector of the photons relative to the plane containing two coincident photons [40].

2.1.3 Internal Conversion

Internal conversion, a competing process to γ-ray decay, occurs when an excited nucleus interacts electromagnetically with an orbital electron and ejects it [40]. The internal conversion electron (ICE) energy, E_{ICE}, is the transition energy, $E_{transition}$, minus the binding energy of the orbital electron, $E_{b.e.}$, as

$$E_{ICE} = E_{transition} - E_{b.e.}. \tag{2.13}$$

The internal conversion coefficient (ICC), α, characterizes the competition between this decay process and γ-ray emission. It is the ratio of the number of internal conversion decays, Δ_{IC}, to the number of γ-ray decays, Δ_γ. This ICC is defined for each electron shell (i.e., the K, L, and M shells, etc), such that the total ratio, α_{total}, is the sum of the ICCs for each shell as

$$\alpha_{total} = \alpha_K + \alpha_L + \alpha_M = \alpha \frac{\Delta_{IC}}{\Delta_\gamma}. \tag{2.14}$$

Using the Band-Raman Internal Conversion Coefficient calculator (BrIcc) [41], the ICCs can be calculated using principles of atomic physics since it depends primarily on the density of the atomic electrons at the center of the nucleus. The number and type of conversion electrons emitted in the decay is also sensitive to the electric or magnetic nature of the radiation. Thus, measurements of the conversion coefficients can be used to differentiate the character of the radiation.

2.2 Prompt gamma-ray neutron activation analysis

Prompt γ-rays are characteristic, making the the detected gamma-ray energies signatures of the particular nuclides that emit them, and their intensities are proportional to the number of atoms under irradiation [39]. For these reasons, prompt gamma-ray neutron activation analysis (PGNAA) is a powerful, non-destructive technique for multi-elemental and isotopic analyses typically employed to measure the chemical composition of samples. The elemental coverage of PGNAA is complementary to instrumental neutron activation analysis (INAA) in the ability to measure elements that do not form neutron capture products that emit delayed γ-rays, such as low-Z, high abundance elements and the high cross section elements (B, Cd, Sm, and Gd) [42]. The PGNAA technique is widely applicable to a broad range fields, including the following with examples given:

- Energy

    - Quantitatively assess hydrogen concentration in zirconium alloys [43]. Hydrogen embrittlement of zircaloy nuclear fuel cladding is one of the main issues in long reactor power cycles.

    - Characterization of produced water in the petroleum industry. [44]

- Security

    - Detection of nuclear threats through the interrogation of cargo containers [45]

- Medicine

    - Determination of boron concentration in blood and tissue samples [46]. Uptake of boron in patients following Boron Neutron Capture Therapy cancer treatment.

– Detection of gadolinium following contrast-enhanced MRI [47][48]

- Archeology

    – Determination of geological origin of different rocks employed for the man-
    ufacture of prehistoric stone tools. [49]

Until recently, a major obstacle in the application of the PGAA method for quanti-
tative multi-element analysis was the lack of a high-quality database of characteristic
prompt gamma-ray energies and intensities. During the era of sodium iodide (NaI)
detectors, which have relatively poor energy resolution compared with modern detec-
tors, Groshev et al [50][51] published the first compilation of prompt γ-ray energies
and intensities while Greenwood et al [52] published the first spectrum catalog. With
the advent of high-resolution germanium detectors in the 1960s, Rasmussen [53] and
Orphan [54] measured capture γ-ray spectra for all elements. These data were later
compiled and published in 1981 by Lone et al [55] in a database of over 10,000 γ-rays,
which was used for many years despite the inadequacies inherent to those early mea-
surements. Prompt γ-ray data are also compiled from the literature in the Evaluated
Nuclear Structure Data File (ENSDF) [9]. These data were used primarily to extract
nuclear structure information and were not evaluated for applied use. In the early
2000s, Reedy and Frankel [56] carefully reevaluated the literature for light elements
from hydrogen to zinc and provided this information in ENSDF format. The Lone
et al, ENSDF, and Reedy gamma-ray intensities are normalized to units of γ-rays
per 100 neutron captures. In the 1990s new capture gamma-ray measurements were
performed for all stable elements by Molnar et al at the Budapest Reactor. An Inter-
national Atomic Energy Agency (IAEA) Coordinated Research Project (CRP) was

organized to evaluate these data. The IAEA CRP produced the Evaluated Gamma-ray Activation File (EGAF) [8], a database of more than 35,000 neutron-capture γ-rays.

The second phase of the EGAF project is an international collaboration with the IAEA led by the nuclear data groups at Lawrence Berkeley National Laboratory and Lawrence Livermore National Laboratory. The long-term goals of this effort are to measure prompt and delayed neutron γ-ray cross sections, σ_γ, with guided neutron beams at the Budapest and Garching FRM II research reactors on isotopically enriched and selected radioactive targets [57]. The new EGAF database will contain the γ-ray cross sections, σ_γ, total radiative thermal neutron cross sections, σ_0, activation data including γ-ray energies, E_γ, transition probabilities, P_γ, half-lives, $T_{1/2}$, and recommended neutron separation energies, S_n [57]. In addition, EGAF will provide adopted level and γ-ray data, as well as improved evaluations of the nuclear structure information, for the ENSDF and Reference Input Parameter Library (RIPL) [11], which are required for nuclear-reaction calculations that are used to generate the Evaluated Nuclear Data File (ENDF) [12].

2.3 ^{94}Nb Nuclear Structure

The ^{94}Nb nucleus has been extensively studied both theoretically and experimentally. One reason for this is a theoretical description of this odd-odd nucleus within the framework of the shell model as a ^{90}Zr core – which has a magic number of neutrons (50) and semi-magic number of protons (40) – to which one proton and three neutrons are coupled [29][34][30]. From this consideration, the lowest-energy configuration, giving rise to 20 positive-parity states, was expected to be the $\pi(1g_{9/2})^1 v(2d_{5/2})^3$, where π and v refer to proton and neutron, respectively. These states arise from the neutron partial configurations with $J = \dfrac{5}{2}, \dfrac{3}{2}$ and $\dfrac{9}{2}$ coupling with the single $1g_{9/2}$ proton to

give rise to 6, 4 and 10 states, respectively. In this proton-neutron multiplet structure, the six lowest-lying states in $[\pi(1g_{9/2})^1, v(2d_{5/2})^3_{5/2}]$ have positive parity and spins from 2^+ to 7^+. These are believed to be the lowest-excitation energy states [34][30][31]: 0.0 keV, 6^+; 40.9 keV, 3^+; 58.7 keV, $(4)^+$; 78.7, $(7)^+$; 113.4 keV, $(5)^+$; and 334.1 keV, which was suggested to be the 2^+ member [36][31]. The next potential positive-parity multiplets could be $[\pi(1g_{9/2})^1, v(2d_{5/2})^3_{3/2}]$ with $J^\pi = 3^+, 4^+, 5^+, 6^+$ and $[\pi(1g_{9/2})^1, v(2d_{9/2})^3_{9/2}]$ with $J^\pi = 0^+, 1^+, 2^+, 3^+, 4^+, 5^+, 6^+, 7^+, 8^+, 9^+$ [31]. Negative-parity multiplets could be formed with the promotion of a $2p_{1/2}$ proton to the $1g_{9/2}$ orbit as $[\pi(2p_{1/2})^{-1}_{1/2}(1g_{9/2})^2_0, v(2d_{5/2})^3_{3/2}]$. In this scenario, the interaction of a proton hole to the neutron partial configurations, $\pi(2p_{1/2})^{-1}_{1/2} \otimes v(2d_{5/2})^3_{3/2, \, 5/2, \, 9/2}$, should give rise to six negative-parity states. These are three doublets with $J^\pi = 1^-, 2^-$, $J^\pi = 2^-, 3^-$ and $J^\pi = 4^-, 5^-$. Considering the promotion of a proton from the closed $2p_{1/2}$ orbit strikes at the assumption of a ^{90}Zr core, experimental evidence suggests that protons are promoted part of the time from the $2p_{1/2}$ orbit to the $1g_{9/2}$ orbit in the ground state of ^{90}Zr [58][30].

The first detailed work was by Gruber et al [29] using a bent crystal spectrometer to investigate the low-lying levels of ^{94}Nb with the ^{93}Nb$(n, \gamma)^{94}$Nb reaction. Around the same time, Sheline et al used the ^{93}Nb$(d, p)^{94}$Nb [34] reaction to also study the low-lying levels. Following these works, Jurney et al [30] contructed a more complete level scheme for the low-lying states of ^{94}Nb based on new ^{93}Nb$(n, \gamma)^{94}$Nb and γ-γ coincidence measurements (up to 700 keV), as well as considering the previous ^{93}Nb$(d, p)^{94}$Nb data by Sheline et al [34]. These measurements established the locations for a large number of states despite limitations in detector resolution, spectrometer response and efficiency for the Ge(Li) spectrometer. Chrien et al established 11 new levels with γ-ray spectra from neutron capture by seven resonances. Haste and Thomas [59] also conducted similar studies of resonance neutron capture. Around

the same time, Hagen et al [35] and Fedorets et al [36] used the ^{94}Zr$(p, n\gamma)^{94}$Nb reaction, which preferentially populates low-spin states, to identify additional states at 302, 450, 666 and 785 keV. These measurements included γ-γ coincidence for determination of the angular distributions. Additionally, tentative J^π assignments were made based on the comparison of the total neutron production cross sections for the levels to those computed using the Hauser-Feshbach model with spin-parities varied from 0^+ to 4^-.

Bogdanovic et al [31] re-examined the low-energy (n,γ) spectrum using a combination of high-resolution spectrometers. This was followed by the measurement of primary γ-rays by Kennett et al in which high-statistical precision was obtained by irradiating niobium powder for 450 hours in tangential beam of the 2 MW McMaster research reactor [33]. The low-energy spectrum up to 3 MeV was also measured y Kennett et al using a filtered neutron beam, but not reported since both the energies and intensities agreed with those measured by Bogdanovic et al [31]. More recently, the complete (n,γ) spectrum was measured for the EGAF as part of efforts to internally standardize the γ-ray spectra all natural occurring isotopes [7][8]. However, comparison of the normalized intensities of these data to those of Bogdanovic et al [31] reveal that the low-energy γ-rays were significantly self-absorbed. Thus, a new measurement of a small-mass niobium oxide target was made for this work.

CHAPTER 3

METHODOLOGY

The methodology used in this work is discussed in this chapter. It begins with the discussion of γ-ray spectra analysis for determining γ-ray energies and intensities. The subsequent section focuses on correcting the intensities for γ-ray self-absorption. The next sections focus on the standardizing these intensities into γ-ray production cross sections σ_γ and creating an EGAF. The last part discusses statistical model calculations with the computer code DICEBOX for the assessing the consistency of the EGAF and determining the thermal-neutron radiative capture cross section σ_0.

3.1 Spectrum Analysis

At the time of the sample spectrum measurement, the detector system needs to be calibrated for energy and detection efficiency. The non-linearity and efficiency curves are updated regularly at the Budapest Research Reactor and are discussed in the next chapter. The computer software Hypermet-PC [60] is employed for peak fitting as it provides the capability of automatic analysis of the γ-ray spectrum [61]. Figure 3.1 exemplifies the ability of Hypermet-PC to resolve γ-ray peaks in complicated spectra. After loading the spectrum, the first step is the energy and resolution calibrations with two peaks of well-defined singlets, one of which is in the low-energy region of the spectrum and the other is in the high-energy spectrum. With increasing γ-ray

energy, the resolution in terms of full-width at half maximum (FWHM) increases. The resolution calibration aids in the automatic spectral fitting in Hypermet-PC. A two-point energy calibration with a low-energy peak and a high-energy peak with known energies translates channel number to energy. This assumes that the detector response is linear with γ-ray energy, which is not true in practice. For a high degree of accuracy in the peak energies, which are the centroids of the peaks, a non-linearity correction is required.
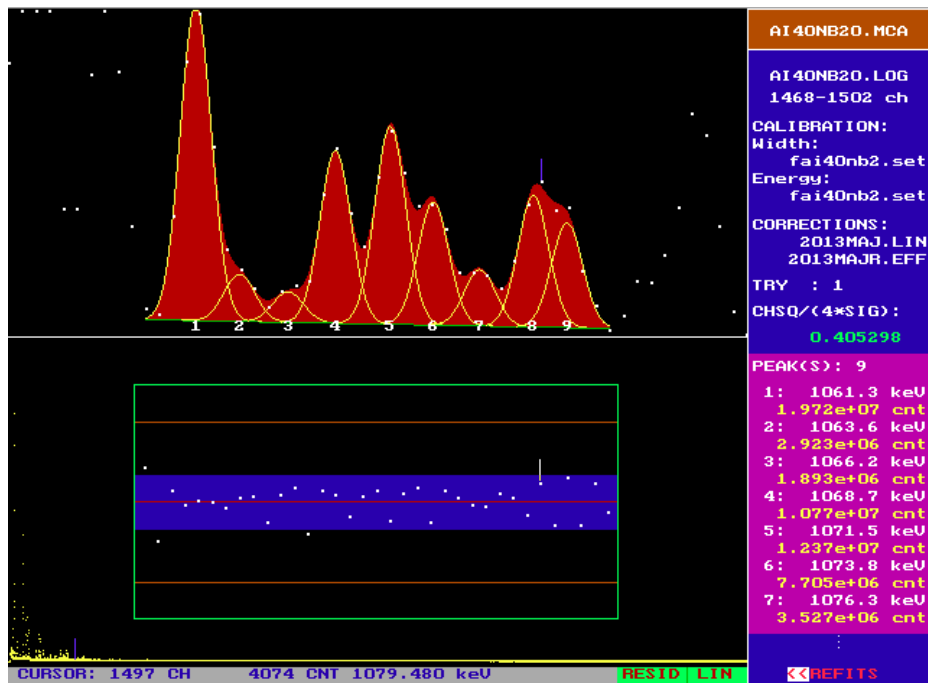
Figure 3.1: Peak fitting using Hypermet-PC

The Hypermet code describes a peak as being asymmetric with a Gaussian distribution and a skew component; the background on which the peak sits is peak-dependent background on a parabolic baseline. The background can be peak dependent with higher background on the low-energy side – represented by a Heaviside

function convoluted by a Gaussian – that is the result of low-angle Compton scattering of γ-rays in the detector and with tailing that is the result of improper charge collection. The skew is also from improper charge collection, but is a feature of the peak unlike the tail. Both the skew and tail terms are represented as exponentially-modified Gaussian functions with exponential decays convoluting a Gaussian on the low-energy side. Two parameters control the skew of the Gaussian fit: A and B are the amplitude and the slope, respectively, of the exponential decay [62]. The A parameter is determined by the Hypermet algorithm for the best peak fit while the B parameter should be tuned for a particular detector system and remains constant throughout the spectrum. Figure 3.2 shows a peak fit with $B = 0.35$ and $B = 0.5$; the peak area is 0.8% lower for $B = 0.35$.

(a) $B = 0.35$ (b) $B = 0.5$
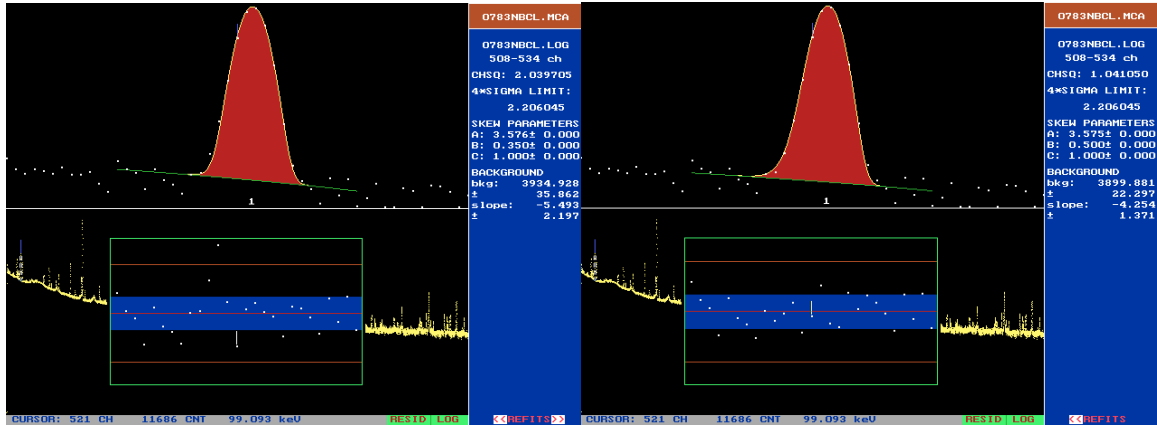
Figure 3.2: The effect of the parameter B, the slope of the skew, on peak fitting.

After calibrating the energy resolution and the skew parameters, Hypermet-PC is used for automatic fitting of all peaks found in the entire spectrum. This serves to identify all major peaks, but the peaks should be inspected for quality. In particular,

the peak should visually represent the data and have reasonable residuals, which are the differences between the channel total and the sum of the peak and background fits. In some instances, the residuals appear to have a Gaussian shape; this can be corrected by adding the estimated peak centroid to the peak list and refitting the region. The goodness-of-fit is represented as the ratio of the reduced chi square to the 4σ limit. The uncertainty of peaks can be improved through refitting the region with added/removed peaks, adjusting the characteristics of the background (step, curve and tail), fine tuning the peak characteristics (width, skew), and adjusting upper and lower boundary of the region of interest. After all peaks are satisfactorily fit, a peak list is generated that includes the following for all peaks: goodness-of-fit $(\chi^2/(1+4\sigma))$, channel, energy and its uncertainty, FWHM and its uncertainty, and the efficiency-corrected peak area and its uncertainty. The uncertainty in peak energy has contributions from the peak fitting, non-linearity and energy calibration. The uncertainty in the efficiency-corrected peak area has contributions from the efficiency calibration, peak fitting and counting statistics. Of these γ-rays in the peak list, those that come from the background (not the sample) are identified and removed from placement in the decay scheme by measuring, in the same configuration, the γ-ray spectra without the sample. The generation of a background peak list with peak count rates is sometimes needed to estimate the contribution to a known peak from the background interference. The peak intensities should be corrected for γ-ray self-absorption, as discussed in the next section.

3.2 Gamma-ray Self-absorption Correction

In irradiating a bulk (finite size) sample with a neutron beam, geometry factors affect the observed γ-ray intensity emanating from different points. In the case of a homogeneous sample, the active volume describes the actual volume from where

γ-rays originate and may be detected while an effective volume represents the integral of the geometry factors over the whole sample [62]. These ideas can be reduced to one dimension in the case of samples with plate geometry; the reaction rate and geometry factor can be described as a function of depth with the thickness representing the active volume, while the effective thickness represents the integral/average of the reaction rate and geometry factor over the entire thickness. The idea of the effective thickness is useful for estimating neutron self-shielding – where the neutron flux decreases with increasing depth in the sample – and γ-ray self-absorption, where γ-rays originating deeper (as seen by the detector) in the sample are attenuated more. With thick samples, high-density materials, and/or high-Z materials – the attenuation may be very significant, especially for low-energy γ-rays (< 500 keV) [63]. The exponential attenuation law

$$\frac{I}{I_0} = e^{-(\mu/\rho)\rho x} \tag{3.1}$$

describes the emerging intensity I of photons with incident intensity I_0 that penetrates a layer of material with thickness x and and density ρ. The mass attenuation coefficients (μ/ρ) are tabulated for elements with heavy-reliance on theory [64]. This attenuation law equation is applicable to the attenuation of γ-rays through uniform layers of materials that act as windows (e.g., thin aluminum or magnesium window of a vacuum chamber) or shielding material (e.g., lithium polymer used to shield γ-ray spectrometers from neutrons). However, the efficiency calibration of the detection system accounts for this attenuation. Self-absorption of γ-rays within the sample is found by integrating the attenuation law, yielding the self-absorption factor F_γ as

$$F_\gamma = \frac{1 - e^{-(\mu/\rho)\rho x}}{(\mu/\rho)\rho x}. \tag{3.2}$$

In instances when the sample is thin, this expression can be approximated as $F_\gamma = e^{-(\mu/\rho)\rho(\frac{1}{2}x)}$, where the effective thickness is half the actual sample thickness. It should

be noted that this assumes a constant reaction rate in the sample (i.e., no neutron self-shielding). F_γ is used to correct the measured peak areas $A_\gamma(E_\gamma)$ for γ-ray self-absorption as

$$A_\gamma(E_\gamma)(corrected) = \frac{A_\gamma(E_\gamma)}{F_\gamma} \tag{3.3}$$

Unless pressed into a pellet, powder samples sealed in a Teflon bag have undefined geometry. This makes estimating the actual sample thickness and accounting for the inhomogeneity in the thickness difficult. An alternative technique for determining the effective thickness for the purpose of γ-ray self-absorption correction employs the spectrum measurement of a second sample with minimal self-absorption and a defined geometry, e.g., a metal foil with a thickness less than 100 micrometers. After the small correction for γ-ray self-absorption, the intensity ratio of an intense, low-energy (<100 keV) peak (with significant self-absorption) to a high-energy (>500 keV) peak provides a reference for determining the effective thickness of the bulk sample. The effective thickness is iterated until the sample's ratio matches that of the reference.

The next section focuses on the standardization of the peak intensities into cross section data relative to a well-known comparator [7].

3.3   Internal Standardization

Internal standardization, with the analyte and comparator contained in the same sample, is to be used to find the partial γ-ray production cross section $\sigma_{\gamma,x}(E_{\gamma,x})$ for a γ-ray peak of energy $E_{\gamma,x}$ for analyte isotope x relative to that of a well-known $\sigma_{\gamma,c}(E_{\gamma,c})$ for a γ-ray peak of energy $E_{\gamma,c}$ for the comparator isotope c. When both the analyte and comparator are $1/v$ absorbers, this technique is convenient for bypassing the detailed characterization of the time- and spatial-dependency of the neutron flux

and reducing the impact of potential systematic effects such as neutron scattering, target characteristics, target-detector geometry, and detector dead-time because the conditions are largely the same for both the analyte and comparator. When dealing with non-$1/v$ isotopes, a generalized approach is required to account for the neutron-spectral influence on the reaction rates [65][4]. The generalized equation for internal standardization is derived in this section.

The equation for the reaction rate R (s^{-1}) is simplest for the case of a mono-energetic, parallel beam impinging on a homogeneous and thin sample of isotope x as

$$R = n_x \sigma_x \phi \qquad (3.4)$$

where n_x is the number of atoms of the examined isotope in the neutron beam, σ_x is the cross section of isotope x for neutron capture at a given energy (cm^2) and ϕ is the neutron flux $(cm^{-2}s^{-1})$. Extending the reaction rate to a general neutron beam, the reaction rate is given as Equation 3.5, where E_n is neutron energy.

$$R = n_x \int_0^\infty \sigma_x(E_n)\phi(E_n)dE_n \qquad (3.5)$$

The partial capture γ-ray production cross section σ_γ is given as Equation 3.6, where P_γ is the fraction of capture events resulting in a gamma ray of energy E_γ, θ is the natural abundance, and σ_x is the cross section of isotope x. Following the same energy-dependence as the capture cross section, it characterizes the probability per atom of the production of a γ-ray with energy E_γ.

$$\sigma_\gamma = \theta_x \sigma P_\gamma = \sigma_x P_\gamma \qquad (3.6)$$

The production rate of γ-rays with energy E_γ from the sample is then given as R_γ in

$$R_\gamma = RP_\gamma = n_x P_\gamma \int_0^\infty \sigma_x(E_n)\phi(E_n)dE_n. \qquad (3.7)$$

27

The count rate ρ_γ of the γ-ray takes into account the detection efficiency $\epsilon(E_\gamma)$ of the detector for the given γ-ray with energy E_γ as

$$\rho_\gamma = \epsilon(E_\gamma)R_\gamma = \epsilon(E_\gamma)n_x P_\gamma \int_0^\infty \sigma_x(E_n)\phi(E_n)dE_n. \tag{3.8}$$

The integral in Equation 3.8 is more convenient in the velocity variable (using the definition of flux $\phi(v) = n(v)v$, where n is the neutron density) and can be split up into two integrals as shown in Equation 3.9, where v_{Cd} is cadmium cutoff velocity corresponding to the cadmium cutoff energy.

$$\int_0^\infty \sigma_x(E_n)\phi(E_n)dE_n = \int_0^{v_{Cd}} \sigma_x(v)n(v)v\ dv + \int_{v_{Cd}}^\infty \sigma_x(v)n(v)v\ dv \tag{3.9}$$

The differential absorption cross section of cadmium drops six orders of magnitude in the span of 70 eV starting at about 0.2 eV [39]. With this property, a cadmium filter is useful for separating the contribution to activation of the slow and epithermal neutrons. The cadmium ratio R_{Cd}, defined by Equation 3.10, is an experimentally-determined parameter characterizing the contribution of the epithermal neutrons to the activation of the isotope x.

$$R_{Cd} = \frac{\int_0^\infty \sigma_x(v)n(v)v\ dv}{\int_{v_{Cd}}^\infty \sigma_x(v)n(v)v\ dv} \tag{3.10}$$

The cadmium cutoff velocity v_{Cd} depends on the thickness of cadmium and neutron spectrum of the beam. It can be determined for the parallel beam by Equation 3.11, where Σ_{Cd} is the macroscopic neutron absorption cross section of cadmium and t is the thickness of the cadmium filter.

$$\int_{v_{Cd}}^\infty \sigma_x(v)n(v)v\ dv = \int_0^\infty \sigma_x(v)n(v)e^{-\Sigma_{Cd}t}v\ dv \tag{3.11}$$

The effective g-factor $\hat{g}$ corrects for the spectral influence of the neutron beam on the reaction rate. This effect is significant for strong non-1/v absorbers but cancels out

for comparison of $1/v$ absorbers. The effective g-factor is given by Equation 3.12, where n_{th} is the neutron density integrated up to the cadmium cutoff velocity.

$$\hat{g} = \frac{1}{\sigma_0 v_0} \frac{\int_0^{v_{Cd}} \sigma_x(v)n(v)v\ dv}{\int_0^{v_{Cd}} n(v)dv} = \frac{1}{\sigma_0 v_0} \frac{\int_0^{v_{Cd}} \sigma_x(v)n(v)v\ dv}{n_{th}} \tag{3.12}$$

Utilizing the cadmium ratio and effective g-factor, Equation 3.9 becomes Equation 3.13, and the count rate ρ_γ simplifies to Equation 3.14.

$$\int_0^\infty \sigma_x(E_n)\phi(E_n)dE_n = \hat{g}\sigma_0 v_0 n_{th}\frac{R_{Cd}}{R_{Cd}-1} \tag{3.13}$$

$$\rho_\gamma = \epsilon(E_\gamma)n_x\hat{g}\sigma_{\gamma,x}v_0 n_{th}\frac{R_{Cd}}{R_{Cd}-1} \tag{3.14}$$

Comparison to a comparator with well-known $\sigma_{\gamma,c}$, such as ^{35}Cl or ^{1}H, by taking the ratio of count rates for specific gamma ray energies yields

$$\frac{\rho_{\gamma,x}}{\rho_{\gamma,c}} = \frac{\epsilon(E_{\gamma,x})n_x\hat{g}_x\sigma_{\gamma,x}(\frac{R_{Cd}}{R_{Cd}-1})_x}{\epsilon(E_{\gamma,c})n_c\hat{g}_c\sigma_{\gamma,c}(\frac{R_{Cd}}{R_{Cd}-1})_c}, \tag{3.15}$$

which can be rearranged to solve for the unknown $\sigma_{\gamma,x}$ as

$$\sigma_{\gamma,x} = \sigma_{\gamma,c}\frac{A_{\gamma,x}}{A_{\gamma,c}}\frac{\epsilon(E_{\gamma,c})n_c\hat{g}_c(\frac{R_{Cd}}{R_{Cd}-1})_c}{\epsilon(E_{\gamma,x})n_x\hat{g}_x(\frac{R_{Cd}}{R_{Cd}-1})_x}. \tag{3.16}$$

Here, A_γ is the peak area in the spectrum, which is the product of the peak count rate ρ_γ and the detector live-time. Equation 3.14 consists of experimentally measurable variables (A_γ, ϵ, R_{Cd} and P_γ) and calculable variables ($\hat{g}$ and n_{th}) with $\sigma_{\gamma,x}$ as the unknown.

Using ^{93}Nb$(n\gamma)^{94}$ as an example, internal standardization with a NbCl$_5$ sample yields the σ_γ of the ^{94}Nb standardization peak relative a well-known chlorine peak. The 1951.1-keV peak, from ^{36}Cl in the ^{35}Cl$(n,\gamma)^{36}$Cl reaction, is the adopted comparator peak for chlorine; its elemental σ_γ is 6.51(4) b. The spectrum measurement of a metal or oxide Nb sample yields a peak list with γ-ray peaks resulting primarily from the ^{93}Nb$(n\gamma)^{94}$Nb reaction. The corrected peak intensities are normalized

29

into σ_γ data using the σ_γ of the standardization peak. This step is accomplished through multiplication of the peak intensities with the calibration factor (in units of barn/count), which is the ratio of the standardization σ_γ to its corrected peak area. After this step, the σ_γ data can be organized into the decay scheme in the form of EGAF.

The main advantage of conducting standardization measurements with guided-neutron beams is that there is little to no contribution from epithermal neutrons. These contribute to resonance neutron capture with excitation energies of the capture state above the neutron separation energy and affect the reaction rate, which has to be corrected for. An advantage of using cold-neutrons beams over thermal-neutron beams is less of a deviation from $1/v$ behavior in the cold-neutron region. This is because there are, for some isotopes, large resonances close to thermal energies that can have significantly higher cross sections than the 2200 m/s cross section. A prime example of this is ^{149}Sm(n, γ) differential cross section, which has a large resonance at 0.0973(2) eV [28]. Figure 3.3 shows the differential cross section compared with $1/v$ behavior. A thermal-neutron beam (and a reactor neutron spectrum) would result in a enhanced reaction rate relative to the tabulated thermal neutron capture cross section because of the resonance. In other words, the effective g-factor would be greater than 1. In the cold-neutron region below 0.0253 eV, the reaction rate for ^{149}Sm is depressed relative to $1/v$ behavior – i.e., the effective g-factor is less than 1. The differential cross section settles into behavior resembling $1/v$ at some energy below 0.0253 eV, but the inverse proportionality is not with the 2200 m/s cross section. In the case of ^{149}Sm(n, γ), the effective g-factor at specific energies – the ratio of the $1/v$ cross section to the actual cross section – asymptotically approaches a constant value of 0.597. The reaction rate in a cold neutron beam is depressed by as much as 40%
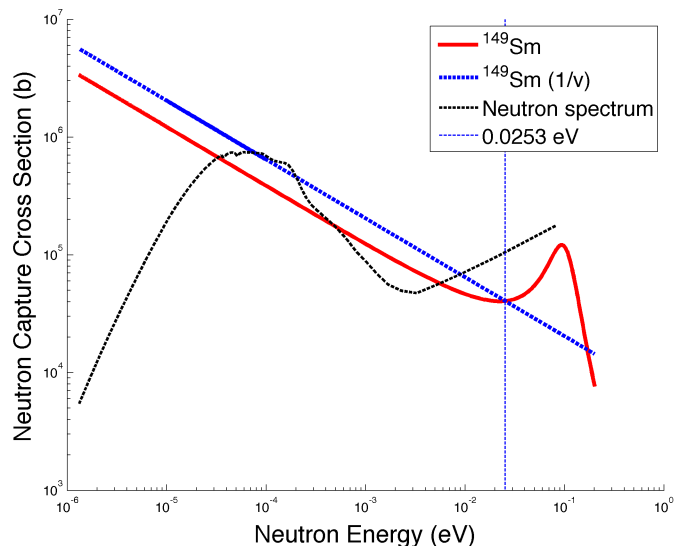
Figure 3.3: The ^{149}Sm(n, γ) differential cross section in the thermal energies compared with $1/v$ behavior.

relative to a $1/v$ absorber. Thus, the effective g-factor is an important consideration in standardization.

3.4   Creating Decay Scheme

Most decay schemes, at least for low-lying levels, are well developed and available in the ENSDF [9], which evaluators have created from all available experimental data and nuclear structure information. The information in ENSDF includes level energies, branching ratios for transitions depopulating the levels, known multipolarities of transitions, internal conversion coefficients (ICCs), and spin and parity assignments for levels. The level energies are determined from linear least-squares fitting of transitions, corrected for nuclear recoil, between levels. The ICCs are calculated from the Band-Raman Internal Conversion Coefficient (BrIcc) calculator. This information, if sufficiently detailed, is initially adopted for creation of the EGAF [8]. The EGAF is

essentially the same as the ENSDF except the branching ratios are replaced with the σ_γ data. In some cases, the accuracy of the level energies can be improved with the new experimental data using the binding-energy test.

A level-intensity balance – the comparison of the total intensity feeding a level and the total intensity depopulating the level – provides a preliminary check of the decay scheme consistency. For medium- and heavy- nuclei, the depopulating intensity should exceed the feeding intensity because of the missing contributions of the continuum γ-rays. When the contrary is true, γ-rays depopulating the level could be missing and/or γ-rays can be misplaced in the decay scheme such that they feed the level. In some instances, the imbalance can be accounted for with spectral interferences or poor peak fits. It can be difficult to narrow down to the cause of imbalances. However, statistical model calculations, as discussed in the next section, provide a powerful technique for building a consistent decay scheme starting from the lowest-lying levels.

3.5   Statistical Model Calculations

Decay schemes are mostly complete for light isotopes (Z < 20). For medium and heavy isotopes, experimental measurements are insufficient in establishing the nuclear structure due to the high density of states. The γ-ray cascades from the decay of highly-excited levels in medium and heavy nuclei can generally proceed via many intermediate levels – as many at $10^5 - 3 \times 10^6$ in the case of heavy nuclei [14]. The γ-rays populating and depopulating these levels are extremely difficult to experimentally resolve since the average-level spacing is below the best-resolution γ-ray spectrometer (2 keV for a HPGe detector system). The set of these levels is referred to as the continuum. However, their contributions to the level scheme can effectively be estimated from calculations using the generalization of the extreme statistical model

– proposed by Bohr in his concept of the compound nucleus [66] – in which the intensities in a γ-ray cascade are treated as statistical variables. Simulation of the γ-ray decay process has been developed to predict experimentally-accessible characteristics of the γ cascade, such as the energies of emitted γ-rays, the γ-ray multiplicity and the populations of individual levels [14].

A major challenge in the statistical treatment of γ-ray cascades was the incorporation of partial radiation width fluctuations of radiative transitions and the implication that these have on the statistical independence of each cascade step. The fluctuations are well understood as following a Porter-Thomas distribution [16] – a χ^2 distribution with one degree of freedom (i.e., Gaussian distribution). The computer code, DICE-BOX [14], employs the Monte Carlo technique to simulate γ-ray cascades with the cascade proceeding via energy bins (rather than defined energy levels). DICEBOX offered the possibility of a full quantitative control over the influence of partial radiation widths fluctuations on uncertainties of the modeled cascade-related quantities. The partial radiation widths, Γ_{if}^{XL}, correspond to the transition probabilities from state i to state f with multipolarity XL and are centered on a meal value given as

$$\langle \Gamma_{if}^{XL} \rangle = \frac{f^{XL}(E_\gamma) E_\gamma^{2L+1}}{\rho(E_i, J_i^{\pi_i})}. \tag{3.17}$$

DICEBOX assumes a critical energy E_{crit} defined as the breakpoint between the discrete levels and the quasi-continuum. Below E_{crit}, all levels and γ-rays are taken from experiment in the form of the EGAF, where all energies, spins and parities and γ-ray de-excitations are regarded as complete and accurate; above E_{crit}, a set of levels is generated as a random discretization of *a priori* known level density formula $\rho(E, J^\pi)$. Each γ-ray cascade simulation begins at the capture state $S_n + E_n$ MeV above the ground state, where S_n is the separation energy and E_n is the neutron energy. The capture state has a total capture cross section $\sigma(E_n)$, total radiative width Γ_0 and has the presumed known spin-parity J_{CS}^π.

The code divides the quasi-continuum region into a specified (usually hundreds) number of finite width energy bins and assigns a density of states to each bin according to well-known empirical models that calculate partial radiation widths for sampling in this quasi-continuum. As individual levels within a bin are too numerous to measure, the widths Γ_{if} linking state i to state f are assumed to follow the fundamental relationship

$$\Gamma_{if} = \sum_{X,L} y_{XL}^2 (E_i - E_f)^{2L+1} \frac{f^{XL}(E_i - E_f)}{\rho(E_i, J_i^{\pi_i})}. \tag{3.18}$$

Here, y_{XL} represents the sampling of the Porter-Thomas distribution. The two primary variables in the calculation of transition probabilities are the strength functions f^{XL} and the level density $\rho(E_i, J_i^{\pi_i})$, both of which are assumed to be known from empirical models. These are discussed in the subsequent sections. A nuclear realization is the set of levels resulting from the discretization of the level-density formula, together with the full set of random partial radiation widths for all needed pairs of levels (i, f) obtained using Equation 3.18. Each nuclear realization consists of thousands of randomly generated capture-state decay cascades. Many nuclear realizations are generated and averaged to get the statistical variation of the models. DICEBOX only considers PSFs for electric dipole ($E1$), magnetic dipole ($M1$) and electric quadrapole ($E2$) transitions. $E1$ transitions are dominant, followed by $M1$ transitions, while $E2$ transitions are much less significant.

3.5.1 Levels Density

The level density of a nucleus, and in this case of the compound nucleus, is defined as the number of energy levels within a given interval of energy. Level densities are one of the key ingredients for nuclear reaction cross section calculations. At low excitation energies, the energy levels of the nucleus are spaced at intervals much larger than the

widths of the states themselves. As excitation energy increases, the number of levels increases, and eventually the nuclear levels are no longer well separated. This region is referred to as the continuum region, and the level density function

$$\rho(E) = \frac{dN(E)}{dE},$$ (3.19)

where $N(E)$ is the cumulative number of levels below an excitation energy E. Nuclear level densities are determined with reliable experimental data, such as the cumulative numbers of low-lying levels and the average spacings between neutron resonances. Two models for the level density, the constant temperature formula (CTF) [67] and the back-shifted Fermi gas (BSFG) [67][68] models, were considered for this work.

Constant Temperature Formula

The CTF model, as the name implies, assumes a constant temperature over the entire range of nuclear excitation energy with the form

$$\rho(E, J) = \frac{f(J)}{T} exp[\frac{E - E_0}{T}].$$ (3.20)

The nuclear temperature, T, is interpreted as the critical temperature necessary for breaking nucleon pairs. The energy back-shift, E_0, is related to proton- and neutron-pairing energies. The spin-distribution factor [67], $f(J)$, employed in these models is given as

$$f(J) = \frac{2J + 1}{2\sigma_c^2} exp(-\frac{(J + 1/2)^2}{2\sigma_c^2}),$$ (3.21)

where $\sigma_c = 0.98 \cdot A^{0.29}$, with A being the mass number of the nucleus, is the spin cut-off factor [1]. It denotes the probability that a randomly chosen energy level has spin J.

Back-Shifted Fermi Gas Model

The BSFG model assumes that the nucleus behaves like a fluid of fermions in the form

$$\rho(E, J) = f(J) \frac{exp(2\sqrt{a(E - E_1)})}{12\sqrt{2}\sigma_c a^{1/4}(E - E_1)^{5/4}}, \tag{3.22}$$

where the spin cut-off factor, σ_c, has an energy dependence given by

$$\sigma_c^2 = 0.0146 \cdot A^{5/3} \cdot \frac{1 + \sqrt{1 + 4a(E - E_1)}}{2a}. \tag{3.23}$$

The parameter, E_1, accounts for the extra amount of energy required to separate fermions, which tend to form pairs, and corresponds to the back-shift in excitation energy. The parameter a represents the shell-model level density parameter that varies approximately with $0.21 \cdot A^{0.87} MeV^{-1}$ [69].

3.5.2 Photon Strength Functions

The other component of the statistical model used in DICEBOX is the photon strength function (PSF), also referred to as the radiative strength function. The PSF is fundamentally a statistical average of the cross section over a large number of levels or resonances of the same spin and parity. It is directly related to σ_{abs} measured by photon absorption experiments. The relationship from the Brink-Axel hypothesis [70] is given as

$$f^{XL}(E_\gamma) = \frac{1}{(2L + 1)\,(\pi\hbar c)^2} \frac{\sigma_{abs}^{(XL)}}{E_\gamma}. \tag{3.24}$$

The PSF is related to the average partial radiation width from an initial state i to a final state f given in the expression

$$\langle \Gamma_{if}^{XL} \rangle = \frac{f^{XL}(E_\gamma) E_\gamma^{2L+1}}{\rho(E_i, J_i^{\pi_i})}, \tag{3.25}$$

where XL denotes the multipolarity of the emitted γ-ray. The transition probabilities decrease sharply with increasing L. Magnetic transitions are less likely than electric ones. Thus, the $E1$, $M1$ and $E2$ transitions contribute the most to any process with the $E1$ PSF being the most important to consider. A high-energy transition with a change in parity is necessarily $E1$ regardless of its intensity since the next allowed multipolarity, $M2$, has never been observed.

Electric Dipole PSF

Electric dipole ($E1$) primary γ-ray transitions dominate decay following thermal neutron capture. The simplest model for the $E1$ PSF is the single-particle (SP) model in the form

$$f_{SP}^{E1} = C\frac{A^{2/3}}{D_s},$$

(3.26)

where $C = 6.8 \times 10^{-8} MeV^{-2}$ and D_0 is the spacing of $l = 0$ single-particle states. This model is energy independent.

The $E1$ PSF is dominated by the low-energy tail of the giant dipole electric resonance (GDER). Theoretical models of the $E1$ PSF describing the GDER are based on parameterizations of the corresponding giant dipole resonance, which is observed in photonuclear reactions with transition probabilities described as a function of γ-ray energy. The GDER can be understood as being caused by the collective dipole vibration of proton and neutron fluids within the nucleus. Brink hypothesized that the nature of the resonance was independent of excitation energy. Consequently, the PSF would be a function of the transition energy rather than a function of excitation energy. Assuming the validity of this hypothesis, the principle of detailed balance for (γ,n) and (n,γ) reactions allows the PSF for the GDER to be written in the standard Lorentzian form, also called the Brink-Axel (BA) model [70][71],

$$f_{BA}^{E1}(E_\gamma) = \frac{1}{3(\pi\hbar c)^2} \cdot \frac{\sigma_G E_\gamma \Gamma_G^2}{(E_\gamma^2 - E_G^2) + E_\gamma^2 \Gamma_G^2},$$

(3.27)

where parameters E_G, Γ_G and σ_G are the energy, width and the cross section that describe the shape of the $E1$ PSF near the maximum of the GDER.

The generalized Lorentzian (GLO) model violates the Brink hypothesis with a dependence on the γ-ray energy and the excitation energy of final state, E_{ex}, that is represented by the nuclear temperature Θ as

$$\Theta = \sqrt{(E_{ex} - \Delta)/a}, \tag{3.28}$$

where Δ is the pairing energy and a is the shell model level-density parameter. For odd-odd nuclei, $\Delta = 0.5 \cdot |P_d|$, where $|P_d|$ is the deuteron-pairing energy. The GLO model has the form

$$f^{E1}_{GLO}(E_\gamma, \Theta) = \frac{\sigma_G \Gamma_G}{3(\pi \hbar c)^2} [F_K \frac{4\pi^2 \Theta^2}{E_G^5} + \frac{E_\gamma \Gamma(E_\gamma, \Theta)}{(E_\gamma^2 - E_G^2) + E_\gamma^2 \Gamma_G^2} (E_\gamma, \Theta)]. \tag{3.29}$$

Here, F_K is the Fermi-liquid parameter. In this model, GDERs built on excited states vary in both shape and size from those built on the ground state because the width of the resonance is also a function of the nuclear temperature as

$$\Gamma_G(E_\gamma, \Theta) = \frac{\Gamma_G}{E_G^2} (E_\gamma^2 + 4\pi^2 \Theta^2). \tag{3.30}$$

In the enhanced generalized Lorentzian (EGLO) version, the $\Gamma_G(E_\gamma, \Theta)$ is modified as

$$\Gamma'_G(E_\gamma, \Theta) = [k_0 + (1 - k_0) \frac{(E_\gamma - E_0)}{(E_G - E_0)}] \Gamma_G(E_\gamma, \Theta), \tag{3.31}$$

where the reference energy, E_0, and enhancement factor k_0 provide the modification of the GLO model. The $\Gamma'_G(E_\gamma, \Theta)$ is substituted into Equation 3.29 for the evaluation of $f^{E1}_{EGLO}(E_\gamma, \Theta)$.

Magnetic dipole strength model

Only the single-particle (SP) model, f_{SP}^{M1}, was considered for $M1$ transitions. It treats the $M1$ strength as an energy-independent constant. Kennett et al. [33] found the average $M1$ strength, $(2.5 \pm 0.4) \times 10^{-8} MeV^{-3}$, to be in agreement with the observation of McCullagh et al. [72] that a value of $\langle f_{M1} \rangle = (3.0 \pm 0.4) \times 10^{-8} MeV^{-3}$ adequately describes all available data from mass 19 to 238. Kennett et al. also noted that the paucity of odd-parity levels prevented analysis of the $E1$ strength, but observed that the lack of any primary transitions with a strengths greater than 1% would seem to indicate that the $E1$ strength is equal to or less than that of for $M1$. As shown in Figure 4.14, the $E1$ strength using the EGLO model is in the range of $0.5 - 3 \times 10^{-8} MeV^{-3}$ below the neutron-separation energy (7.227 MeV). In this study, the value of f_{SP}^{M1} was treated as an adjustable parameter in the DICEBOX simulations to obtain good agreement between the DICEBOX-predicted and experimentally derived value of the total radiative capture width $\langle \Gamma_0 \rangle$. The value $f_{SP}^{M1} = 1.2 \times 10^{-8} MeV^{-3}$, coupled with the EGLO PSF model, produced a derived $\langle \Gamma_0 \rangle$ in agreement with the literature value.

Electric quadrupole strength

A giant quadrupole electric resonance (GQER) model has been used to describe the PSF for $E2$ multipoles. The following convention was used to determine the global parameterization used to determine the set of resonance parameters: $E_G = 63A^{-1/3}$ MeV [73], $\Gamma_G = (6.11 - 0.012A)$ MeV, and $\sigma_G = 1.5 \times 10^{-4} \dfrac{Z^2 E_G^2 A^{-1/3}}{\Gamma_G}$ mb. Quadrapole strength contributes far less than dipole strengths. Transitions corresponding to higher multipoles, including $M2$, are not considered in modeling the capture-state decay in this work.

3.5.3 Decay Scheme Evaluation

DICEBOX is useful as a consistency check of the decay scheme, particularly the nuclear structure information [14] and experimental data [15]. The modeled populations of the levels below E_{crit} depend upon the assumed experimental decay scheme, the capture-state spin composition ($J = J_{gs}$(target)$\pm 1/2$ for odd-odd and odd-A targets), and the choice of adopted level density (LD) and photon strength function (PSF) models. The experimental depopulation (experimental data below E_{crit}) is compared to the modeled population in a population-depopulation (DP) plot for each level below E_{crit}. Figure 3.4 shows an example PD plot. The J^π assignments of the levels are used to label the levels. The vertical axis shows the calculated population per neutron capture to a given level as determined by DICEBOX. The horizontal axis is the experimentally-determined intensities depopulating the level normalized to the total radiative thermal-neutron capture cross section σ_0 determined in Equation 3.33 This is calculated using

$$P_L^{exp} = \sum_{i=1}^{N} \frac{\sigma_{\gamma i}(1 + \alpha_i)}{\sigma_0},$$
(3.32)

where N denotes the number of γ-rays depopulating the level. Uncertainties in the population along the vertical axis correspond to Porter-Thomas fluctuations from independent nuclear realizations, while those along the horizontal axis are due to the experimental uncertainty in the measured cross sections depopulating the levels.

The experimental γ-ray cross sections depopulating the low-lying levels below E_{crit} are used to re-normalize the simulated population per neutron capture, from DICEBOX, to absolute cross sections feeding these levels. The total radiative thermal neutron-capture cross section σ_0 is determined as

$$\sigma_0 = \sum \sigma^{exp}(1 + \alpha)(GS) + \sum \sigma_\gamma^{sim}(GS) = \frac{\sum \sigma_\gamma^{exp}(1 + \alpha)(GS)}{1 - P(GS)},$$
(3.33)
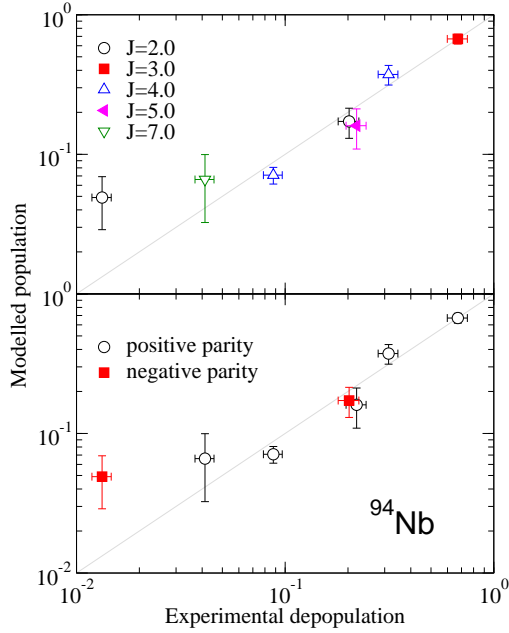
Figure 3.4: Example population-depopulation plot.

where $\sum \sigma^{exp}(1+\alpha)(GS)$ represents the sum of experimental transition cross sections feeding the ground state. Figure 3.5 illustrates this summation for a decay scheme, where the contribution of ground state feeding from the continuum is grouped together. The simulated contribution from the quasi-continuum above E_{crit} feeding the ground state, $\sum \sigma_\gamma^{sim}(GS)$, may also be written as the product of σ_0 and the simulated ground-state population per neutron capture, $P(GS)$, given by DICEBOX as shown in Equation 3.33.
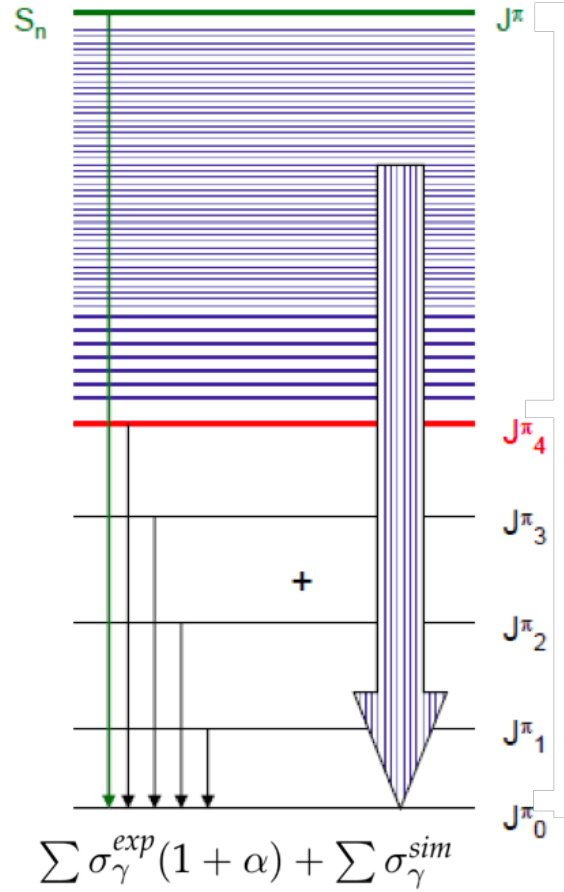
Figure 3.5: Illustration of σ_0 determination as the combination of experimental and simulated ground-state feeding.

The PD plot compares the intensity balance through all states up to E_{crit}. Scatter around the population = depopulation line is a measure of the quality and completeness of the experimental data and provides a test of the ability of the statistical model to simulate the experimental decay scheme. Model dependence in the PD plot can manifest in spin-dependent deviations while an isolated deviation is indicative of any number of errors in the experimental data and nuclear structure evaluation. For levels with higher modeled population than experimental depopulation, these include:

- Missing γ-ray depopulating the level

- Lower than actual γ-ray intensity

- Lower than actual ICC: This could be indicative of an incorrect multipolarity assignment or mixing ratio for mixed transitions. Since transitions with lower-order multipoles have smaller ICCs, this would mean that the multipole is of lower-order or the mixing ratio is lower than actual.

- Incorrect spin-parity assignment. Since feeding of levels close to the capture-state spin-parity is favored by selection rules (and the assumptions in DICE-BOX), the actual spin could be further from that of the capture-state so that the modeled population is reduced.

Conversely, for levels with higher experimental depopulation than modeled population, these include:

- Extraneous γ-ray depopulating the level

- Higher than actual γ-ray intensity

- Higher than actual ICC: This could be indicative of an incorrect multipolarity assignment or mixing ratio for mixed transitions since lower-order multipoles have smaller ICCs.

- Incorrect spin-parity assignment: The actual spin could be closer to that of the capture-state so that the modeled population is higher.

The advantage in using DICEBOX for evaluation of the decay scheme – if the statistical model is able to simulate the experimental decay scheme – is that the focus can be on the low-lying levels below E_{crit} rather than entire decay scheme, which is highly interdependent and complicated. The low-lying levels are spaced farther apart on average and there are fewer levels that they can feed, which makes

identifying transitions between them easier. With N_{max} being the number of levels, including the ground state, below E_{crit}, the DICEBOX evaluation process should start with $N_{max} = 2$ (the ground state and lowest-lying level) and increase N_{max} by one level if the PD plot is consistent. As few as 10 nuclear realizations each with 10,000 cascade events is sufficient for a quick simulation, though the lowest-populating levels will have large uncertainties in modeled population. More detailed work, such as for the determination of σ_0, should have 50 nuclear realizations with 50,000 cascade events. If it is apparent that statistical model reproduces the experimental decay scheme up to N_{max}, then increasing to $N_{max} + 1$ should maintain the consistency. If a major deviation occurs for the highest level in the $N_{max} + 1$ simulation, missing γ-rays or incorrect γ-ray intensities (e.g., due to background interference) should be first investigated. In dealing with low-lying levels, the major transitions from each level are usually correctly placed by coincidence measurements and/or the binding-energy test. If no solution is found investigating the experimental data, a tentative spin assignment can be hypothesized as ± 1 (depending on selection rules and known multipolarities) and/or a tentative parity assignment can be changed and tested with a subsequent simulation.

The process in creating the EGAF would ideally proceed sequentially from spectra measurements through producing the decay scheme in EGAF format with standardized σ_γ. Unfortunately, these are tedious steps that are subject to revision for a number of reasons. This procedure is represented in a flow chart shown in Figure 3.6 (adapted from Ref. [22]), where the purple rectangles represent processing steps and the yellow diamond is a decision point .

All possible combinations of PSF and LD models should be considered in assessing the consistency of the level scheme, though the calculations can be narrowed to one
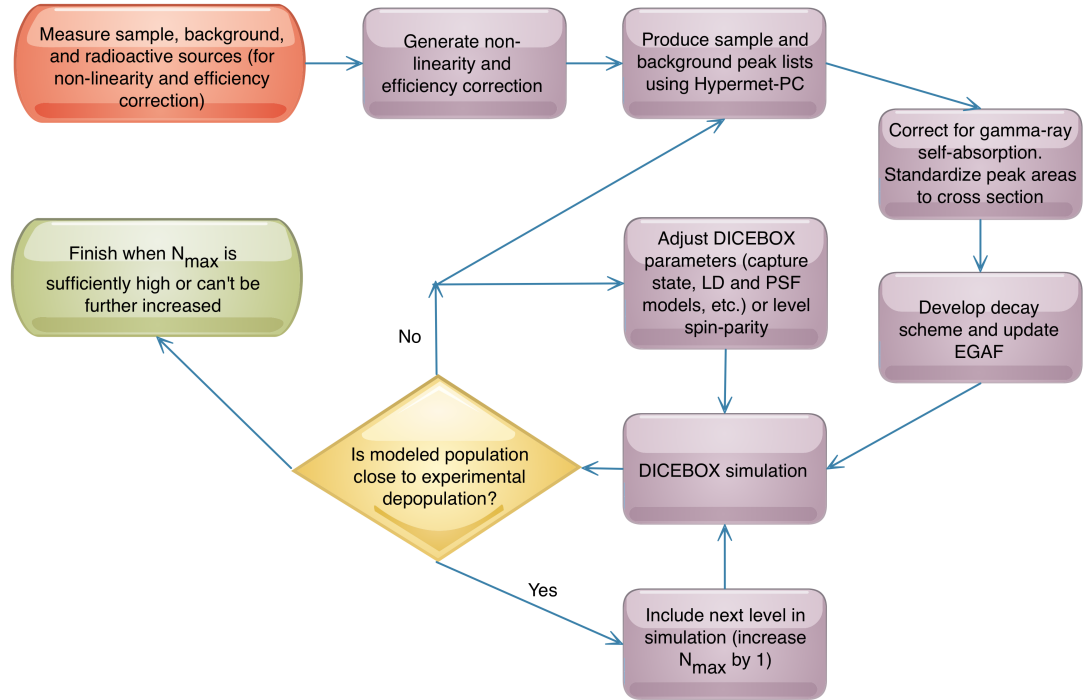
Figure 3.6: The general data analysis procedure represented in a flow chart.

PSF/LD combination. The process of creating the EGAF iterates until conditions are met, which include:

- The modeled population closely matches experimental depopulation for most, if not all, levels below E_{crit}.

- N_{max}, the number of experimentally-determined levels included in the DICE-BOX simulation, is sufficiently high.

- The PSF model adequately represents the (n, γ) cross section data in the quasi-continuum with the total radiative width, Γ_0, from DICEBOX results similar to the literature value.

- the LD model is deemed adequate by the average level spacing, D_0, from DICE-BOX results match literature.

- σ_0 is similar to the literature values, unless there is ample reason for a discrepancy.

  Since this methodology offers an independent measurement of σ_0, the last criterion is only used for comparative purposes, not as the final solution that is iteratively found. In the next chapter, this methodology is applied for the creation and evaluation of the ^{93}Nb(n,γ)^{94}Nb EGAF.

CHAPTER 4

RESULTS AND DISCUSSION

This chapter provides a case study in applying the methodology for measuring prompt γ-ray data and evaluation the decay scheme with statistical model calculations. It is oganized into three parts. The first section focuses on the experiment and data analysis of the $NbCl_5$ and Nb_2O_5 prompt γ-ray spectra measurements. The second part focuses on the statistical model calculations with DICEBOX. A third part gives prelimary results to final high-resolution measurements of $NbCl_5$ and Nb_2O_5 that were performed after completion of the first two parts and with limited time to complete the analyses.

4.1 Experiment and Data Analysis

This section provides information about the prompt γ-ray spectra acquisitions of the niobium chloride ($NbCl_5$) and niobium oxide (Nb_2O_5) samples. The first part discusses the experimental setup. The subsequent sections discuss the estimation of the *effective* thickness for the correction of γ-ray self-absorption and the effective g-factor. Thereafter, the standardization of a niobium prompt γ-ray intensities relative to one from chlorine capture is discussed.

47
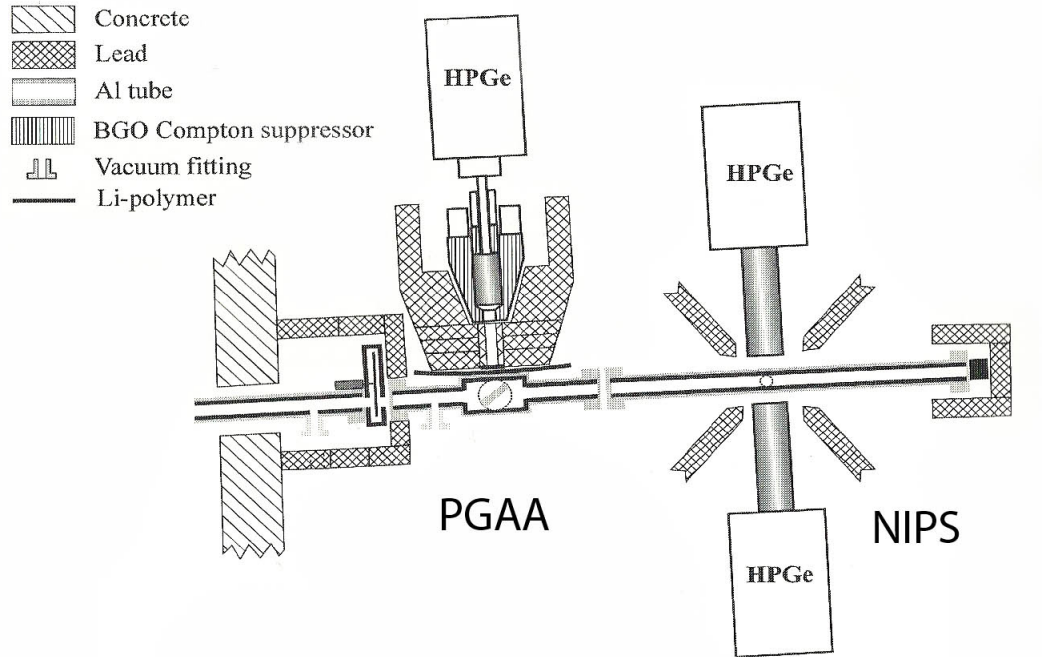
Figure 4.1: The PGAA and NIPS facilities at the Budapest Research Reactor [3].

4.1.1 Experimental Setup

The Nb_2O_5 and $NbCl_5$ experimental data were measured at the prompt gamma-ray activation analysis (PGAA) facility at the 10-MW Budapest Research Reactor with guided cold-neutron beams. The target station, where both primary and secondary γ-rays can be measured in low-background conditions, is located about 35 meters from reactor at the end of a slightly curved, nickel-coated super-mirror guide [3]. A liquid-hydrogen cold source provides moderation of the reactor neutrons. The resulting cold-neutron beam had a thermal-equivalent neutron flux of 7.7×10^7 n $\cdot$ $cm^{-2} \cdot s^{-1}$ at the times of the experiments. The beam is divided in order to serve two experimental facilities: the PGAA facility and the Neutron-Induced Prompt-gamma Spectroscopy. The schematic of these facilities is shown in Figure 4.1.
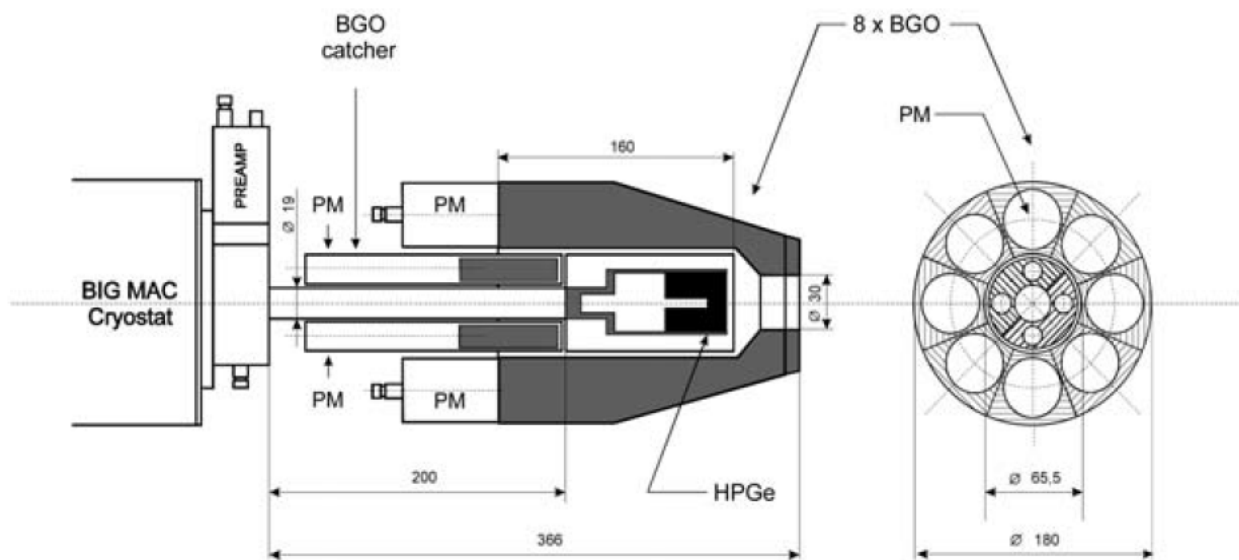
Figure 4.2: The cross-sectional view of the HPGe-BGO γ-ray spectrometer at the Budapest Research Reactor [4].

Prompt γ-rays from the targets were measured with an n-type high-purity, 25% efficient, high-purity germanium (HPGe) detector with closed-end coaxial geometry located 23.5 cm from the target. The detector is Compton-suppressed by a bismuth germanate (BGO)-scintillator guard detector annulus surrounded by 10-cm-thick lead shielding. The cross-sectional view of the detector system is shown in Figure 4.2. The processed and digitized pulse height signals were recorded in a computer-driven multi-channel analyzer.

The Nb_2O_5 and $NbCl_5$ samples, shown in Figure 4.3, were powders suspended in a Teflon bags. The Nb_2O_5 target had a mass of 0.47144 gram and 99.5% purity. The powder sample had approximate dimensions of 8 mm × 24 mm, a thickness less than 1 mm and 4.47 g/cm^3 theoretical density. It was irradiated for 23.9 hours with

a 1.4% dead time. A 39.6-hour count of the background accompanied the Nb_2O_5 measurement for identification of background γ-rays.

The $NbCl_5$ target had a 0.2-gram mass and 99.995% purity. Trace analysis results using inductively coupled plasma mass spectrometry and an assay using silver-nitrate titration confirmed the purity and stoichiometry, respectively. The approximate dimensions were 6 mm × 16 mm with a 1.2-mm thickness and theoretical density of 2.75 g/cm^3. This target was irradiated for 15.6 hours with a 4.8% dead time. A collimator of 10 mm × 10 mm was in place, reducing the visibility of the beam to the sample. The undefined geometry and inhomogeneous thickness were inconsequential for the purpose of internal standardization of a stoichiometric compound because the conditions were the same for both the analyte and comparator isotopes (^{93}Nb and ^{35}Cl, respectively). They do make γ-ray self-absorption correction more precarious, though. The subsequent section discusses estimating the *effective* thicknesses of the samples for correction of γ-ray self-absorption.

(a)   (b)
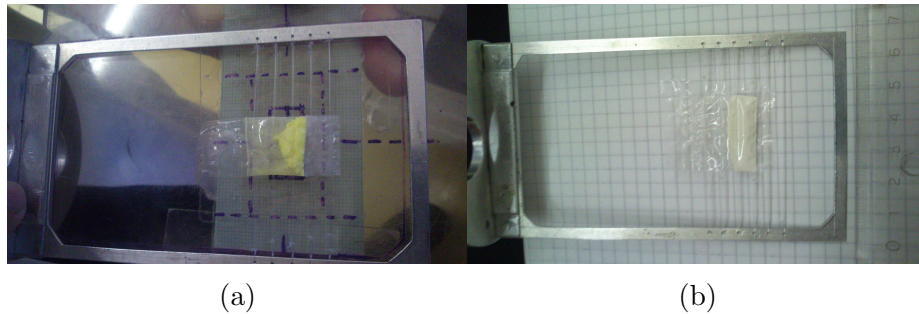
Figure 4.3: The (a) $NbCl_5$ and (b) Nb_2O_5 samples

The counting efficiency and energy calibrations were calibrated from 0.05 − 11 MeV with radioactive sources (^{133}Ba, ^{152}Eu, ^{207}Bi, ^{226}Ra and ^{241}Am) and (n,γ) reaction γ-rays from nitrogen and chlorine targets. The energy calibration was conducted

50

with one peak in the low-energy region and the other in the high-energy region. For these, the 499.426(8)-keV and 5101.33(12)-keV γ-rays were used. The γ-ray spectroscopy software package Hypermet-PC [60] was used to generate the efficiency and non-linearity curves and to perform peak-fitting analysis of the complex γ-ray specta. The efficiency and non-linearity curves for the Nb_2O_5 and $NbCl_5$ experiments are shown in Figures 4.4 and 4.5, respectively.
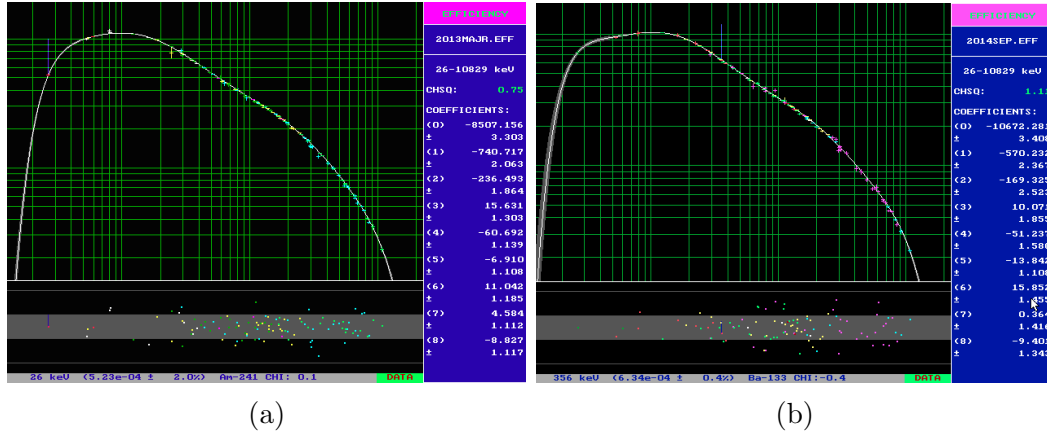
Figure 4.4: Efficiency calibration curves used for the (a) Nb_2O_5 and (b) $NbCl_5$ measurements.
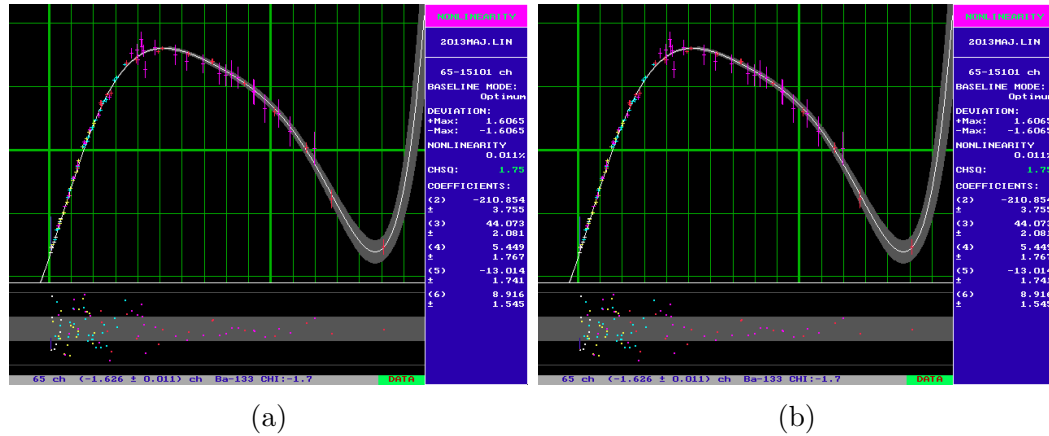
Figure 4.5: Non-linearity curves for the (a) Nb_2O_5 and (b) $NbCl_5$ measurements.

4.1.2 γ-ray Self-Absorption Correction

Though the samples were low density and kept thin, the low-energy γ-rays were atten-
uated within the sample. The powder samples had non-uniform thicknesses that were
unable to be measured, only estimated. Thus, the *effective* sample thicknesses of the
Nb_2O_5 and $NbCl_5$ samples were determined for the purpose of γ-ray self-absorption
correction. This was achieved by iterating the effective thickness until both a low-
energy γ-ray (with significant self-absorption) and a higher-energy (with insignificant
self-absorption) matched the γ-ray intensities from ENSDF. The data and prescribed
method for γ-ray attenuation were from Reference [64]. The ENSDF data are based
on a measurement by Bogdanovic et al [31] of a 50 microgram metal niobium foil
with dimensions $(12 \times 12 \times 0.05)$ mm^3, which had minimal self-absorption. The
reaction rate as a function of depth in the sample was considered, but the neutron
flux was assumed constant throughout the sample on the basis of the low absorption
cross sections of the isotopes involved.

The effective Nb_2O_5 target thickness was determined by considering the intensity

ratio of the low-energy γ-rays with well-resolved peaks – the 78.7-, 99.4- and 113.4-keV γ-rays – to that of the 499.4-keV γ-ray. Table 4.1 shows the comparison of these ratios for the ENSDF data and for this Nb_2O_5 measurement with no self-absorption correction and for correction with effective thicknesses of 0.2 mm. The ratios for the Nb_2O_5 measurement with a 0.2 mm effective thickness were within the experimental error of the ENSDF data. The γ-ray self-absorption curve, which is normalized intensity I/I_0 versus γ-ray energy, is shown in Figure 4.6 for the 0.2 mm effective thickness. For comparitive purposes, the theoretical thickness was 0.6 mm using the sample dimensions (8 mm $\times$ 24 mm), mass (0.47 g) and density (4.47 g/cm^3); assuming that the reaction rate was constant within the sample, an estimation for the effective thickness was 0.3 mm – half the thickness considering that the center of the sample would be the average depth for γ-ray emission.

Table 4.1: Comparison of the intensity ratios of low-energy γ-rays to the 499.4-keV γ-ray for the ENSDF data and the Nb_2O_5 measurement with no self-absorption correction and for correction with effective thicknesses of 0.2 mm.

E_γ (keV)	ENSDF	Nb_2O_5 Uncorrected	Nb_2O_5 0.2 mm thickness
78.7	0.548 ± 0.020	0.496 ± 0.004	0.553 ± 0.005
99.4	4.593 ± 0.116	4.387 ± 0.032	4.646 ± 0.034
113.4	2.410 ± 0.066	2.342 ± 0.015	2.437 ± 0.016

A further check of the effective thickness was performed by considering only the 78.7-, 99.4- and 113.4-keV γ-rays. Considering the drastic difference in γ-ray self-absorption between 78.7-keV and 113.4-keV, which was 6.5% as seen in Figure 4.6, the intensity ratios of the 78.7- and 99.4-keV peaks to the 113.4-keV peak were considered. Table 4.2 shows the caparison ratios for the ENSDF data and the uncorrected and
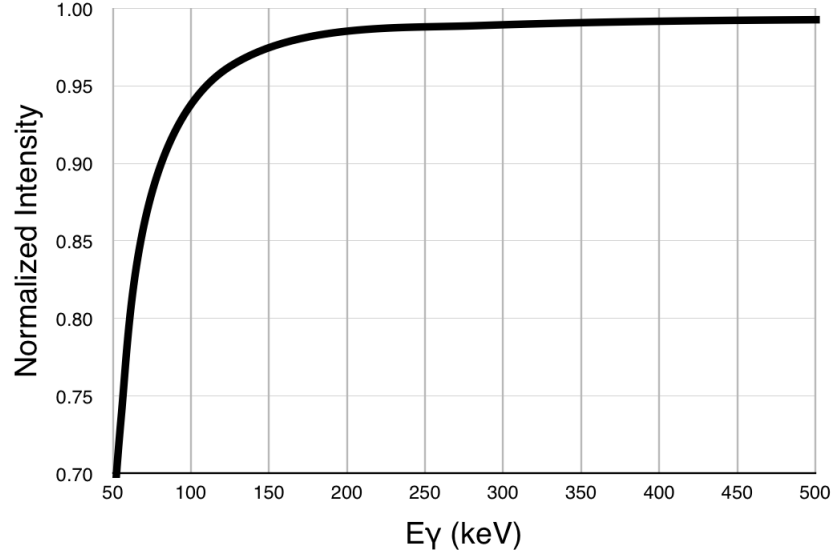
Figure 4.6: The Nb_2O_5 γ-ray self-absorption curve using the 0.2 mm effective thickness.

corrected (using the 0.2 mm effective thickness) Nb_2O_5 data. The agreement of the Nb_2O_5 data using the 0.2 mm effective thickness with the ENSDF data was excellent, further substantiating the 0.2 mm effective thickness.

Table 4.2: Comparison of the intensity ratios of the 78.7-keV and 99.4-keV γ-rays to the 113.4-keV γ-ray for the ENSDF data and the Nb_2O_5 measurement with no self-absorption correction and for correction with effective thicknesses of 0.2 mm.

E_γ (keV)	ENSDF	Nb_2O_5 Uncorrected	Nb_2O_5 0.2 mm thickness
78.7	0.227 ± 0.009	0.212 ± 0.002	0.227 ± 0.002
99.4	1.906 ± 0.057	1.873 ± 0.015	1.906 ± 0.015

Ideally, the standardization peak would be of high energy (>500 keV) so that the γ-ray self-absorption would be negligible. As discussed in a following section

about standardization, the 255.9-keV γ-ray had the only suitable peak in the NbCl$_5$ spectrum for standardization. The NbCl$_5$ sample, a low-density powder (2.75 g/cm^3) in a thin geometry (1.2 mm estimated thickness), was expected to have minor γ-ray self-absorption for this peak. Thus, an effective thickness needed to be estimated for the purpose of γ-ray self-absorption correction. Prompt γ-rays from chlorine neutron capture were considered for estimating the effective thickness, but few peaks under 500 keV were both intense and interference free. Since the 99.4- and 113.4-keV γ-rays have a sharp difference in γ-ray attenuation by NbCl$_5$ and lie on the flat portion of the efficiency curve, the intensity ratio of these two peaks were used for estimating the effective thickness of the NbCl$_5$ sample. The 99.4- and 113.4-keV γ-ray peaks, shown in Figure 4.7, both had good peak fits without background interferences. The effective thickness for the purpose of γ-ray self-absorption correction was found by iterating the effective thickness until the ratio of the 99.4-keV peak area to the 113.4-keV peak area was similar to the ENSDF intensity ratio. As seen in Table 4.3, the ratio, after γ-ray self-absorption was corrected with a 0.6 mm effective thickness, matched that of ENSDF. The selected effective thickness, 0.6 mm, resulted in a 1.3% increase in the 255.9-keV σ_γ. It should be noted that the uncertainty introduced in finding the effective thickness was less significant than the uncertainty in the peak area: adjusting the effective thickness by ± 0.1 mm results in a change in σ_γ of $\pm 0.2\%$, which is less than the 0.8% uncertainty in the peak area.

Table 4.3: Comparison of the intensity ratios of the 99.4-keV γ-ray to the 113.4-keV γ-ray for the ENSDF data and the NbCl$_5$ measurement with no self-absorption correction and for correction with effective thicknesses of 0.6 mm.

E_γ (keV)	ENSDF	NbCl$_5$ Uncorrected	NbCl$_5$ 0.6 mm thickness
99.4	1.906 ± 0.057	1.879 ± 0.027	1.911 ± 0.028
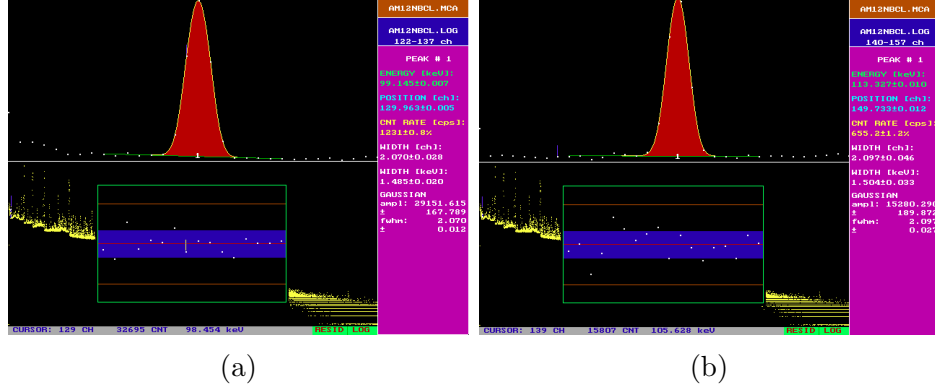
Figure 4.7: The (a) 99.4- and (b) 113-keV peaks in the NbCl$_5$ spectrum

4.1.3 Effective g-factor

The cold-neutron spectrum at the PGAA-NIPS facility was recently measured with the time-of-flight method [5]. The availability of these data allow for a minor correction in the deviation of the ^{93}Nb(n,γ) cross section from $1/v$ behavior by calculating the effective g-factor. The deviation from the $1/v$ cross section – extrapolated using $\sigma = \sigma_0 \dfrac{v_0}{v}$ – to the actual cross section from ENDF/B-VII.1 [12] is

$$\delta_0 = \frac{\sigma(v)v}{\sigma(v_0)v_0}. \tag{4.1}$$

Figure 4.8 shows the plot of δ_0 for the ^{93}Nb(n,γ) and ^{35}Cl(n,γ) reactions along with the differential cold-neutron spectrum. Qualitatively, this plot reveals that ^{93}Nb reaction rate is slightly depressed in a cold-neutron beam and potentially enhanced in a thermal-neutron beam, while ^{35}Cl exhibits $1/v$ behavior below 0.0253 eV. The effective g-factors for ^{93}Nb and ^{35}Cl, calculated using Equation 3.12, were 0.994 and 1.000, respectively. Thus, the reaction rate of ^{93}Nb was depressed 0.6% relative to that of ^{35}Cl. The effective g-factor 0.994 ± 0.001 was applied the ^{94}Nb standardization peak.
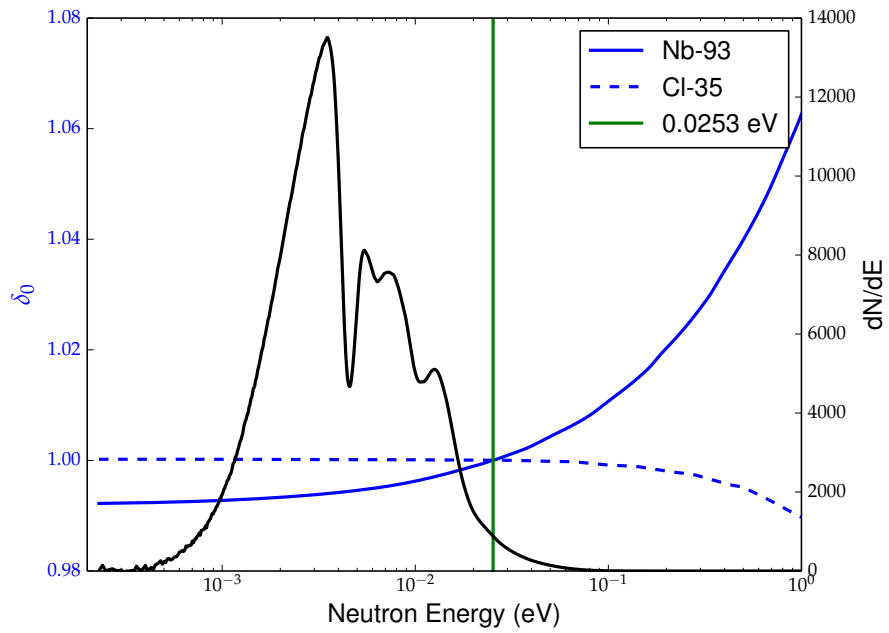
Figure 4.8: The deviation from $1/v$ behavior, δ_0, for the ^{93}Nb(n,γ) and ^{35}Cl(n,γ) reaction cross sections and the differential cold-neutron spectrum at the Budapest Research Reactor PGAA facility [5].

The non-1/v behavior of the ^{93}Nb(n,γ) reaction, according to Figure 4.8, could have been the cause of the discrepancy between the cold-neutron beam standardization performed in this work and the thermal-neutron beam measurement by Révay and Molnár [7]. This topic is touched upon in the next section about standardization. Furthermore, previous σ_0 measurements may not have been corrected for the non-1/v behavior of ^{93}Nb, as discussed in the next session about standardization.

4.1.4 Standardization

The standardization of the niobium capture γ-rays relative to the 1951.1-keV γ-ray from ^{36}Cl is discussed in this section. The previous standardization by Révay and Molnár [7] at the Budapest Research Reactor measured NbCl$_5$ in a thermal-neutron beam for the standardization of niobium prompt γ-ray data. A 0.5 gram NbCl$_5$ sample with 0.6 g $\cdot$ cm^{-2} thickness in a plate geometry was measured for 81,864 seconds. The 499.4-keV γ-ray peak of ^{94}Nb was standardized to the 1951.1-keV γ-ray comparator peak of ^{36}Cl. The σ_γ for the 499.4-keV γ-ray peak was determined to be 0.065 $\pm$ 0.005 b [7]. The NbCl$_5$ spectrum from this measurement was considered in this work for comparison to the new measurement.

In investigating the 499.4-keV peak for standardization, several complications were found that diminish its quality as the standardization peak. As shown in Figure 4.9, a background peak at 500.1 keV (from germanium neutron capture) with a count rate of (61.8 $\pm$ 3.8) cps was found to be interfering with the 499.4-keV peak. The 499.4-keV peak area, with a count rate of (340.9 $\pm$ 9.2) cps, could be comprised by as much as 18% of the background counts based on the count rates. Furthermore, the 499.4-keV peaks – in both the previous and new NbCl$_5$ spectra measurements – were situated on the downward slope of background in close proximity to the 511-keV annihilation peak and the intense 517-keV γ-ray from ^{35}Cl neutron capture, as shown

in Figure 4.10 for the new measurement. It was found that the peak fit for the 499.4-keV γ-ray varied considerably even though each fit had a chi-square goodness-of-fit less than 1, likely from the complexity of the background spectrum in this region. The variability of the 499.4-keV peak fit and the presence of the interfering background peak could account for the high σ_γ for the 499.4-keV γ-ray (relative to this work).
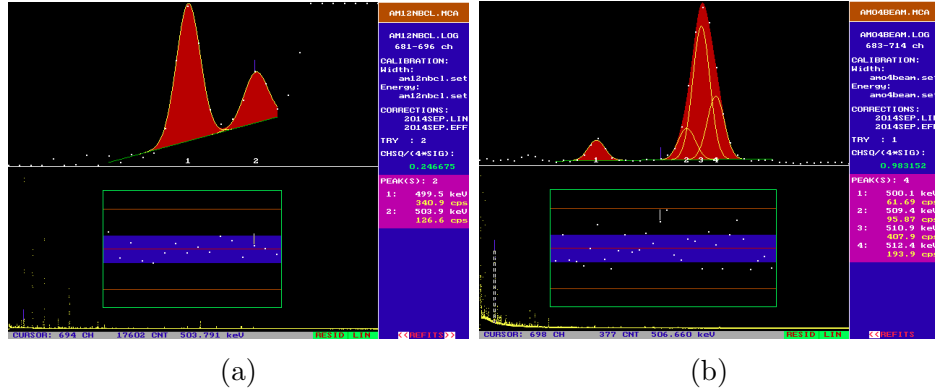
Figure 4.9: The (a) 499.4-keV peak in the NbCl$_5$ spectrum and (b) the interfering peak in the background spectrum

Since the 1.15(5) b [28] thermal neutron capture cross section σ_0 of niobium is small compared to that of ^{35}Cl (43.6 b [28]), the γ-ray intensities are far lower than those of chlorine, thus limiting the choices for standardization peaks. All of the highest intensity niobium-capture peaks were considered, including the γ-ray peaks with the following energies (in keV): 99.4, 113.4, 253.1, 255.9, 293.2, 309.9, 337.5, 458.5, 518.1, 562.3, 835, 957.3, 1118.5 and 1206.3. However, all of these peaks – except for the the 99.4-, 113.4 and 255.9-keV peaks – suffered from large peak area uncertainties due to chlorine and background interferences and/or weak intensities. The 99.4- and 113.4- peaks were not considered because of their sensitivity to the effective thickness used in γ-ray self-absorption correction. The 255.9-keV γ-ray, with the second highest
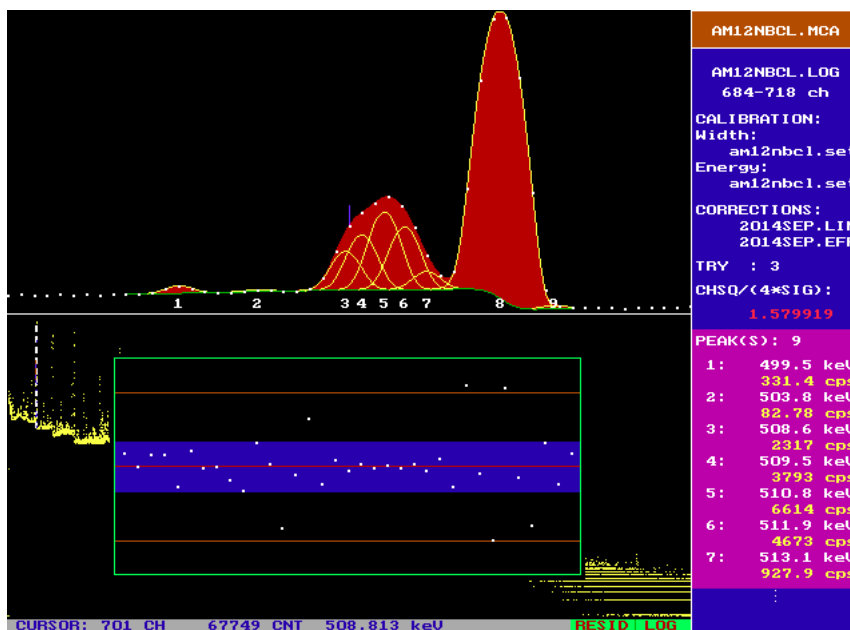
Figure 4.10: The 499.4-keV γ-ray peak from the remeasured NbCl$_5$ spectrum.

intensity of ^{94}Nb prompt γ-rays, was found to have a good fit with little variability, making it the best candidate for the standardization peak. The intensity ratio of the 253.1-keV γ-ray to the 255.9-keV γ-ray was 0.746 ± 0.025, 0.799 ± 0.010, 0.744 ± 0.005 for the ENSDF data, NbCl$_5$ spectrum and Nb$_2$O$_5$ spectrum, respectively. An interfering background peak, found at 253.3 keV, accounted for the discrepancy in the NbCl$_5$ measurement. The intensity ratio, corrected for the background interference, was 0.741 – within the uncertainty of the other data. Figure 4.11 shows the 255.9-keV peak in the NbCl$_5$ spectrum and a 253.3-keV peak interfering in the background spectrum.

On the discussion of background interferences, the low thermal neutron capture cross section of niobium and its low mass in the NbCl$_5$ sample (approximately 69 mg of the 200 mg sample), which is necessitated to reduce γ-ray self-absorption, make the niobium peaks susceptible to background interferences. Consider the Nb$_2$O$_5$ sample

60
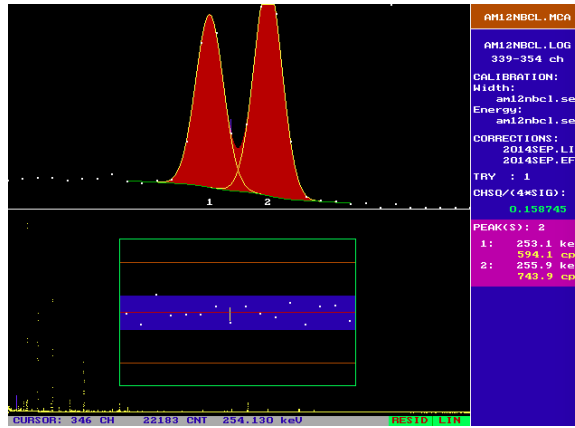
(a)
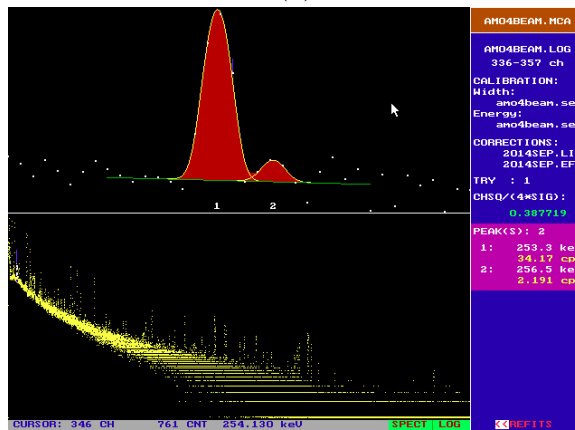
(b)

Figure 4.11: The (a) 255.9-keV standardization peak in the NbCl$_5$ spectrum and (b) the interfering peak in the background spectrum

with 329 mg of niobium (of the 470 mg sample) – the interfering peak had a count rate that was only 0.5% of the 253.1-keV peak in the NbCl$_5$ spectrum due to its higher intensity (9040 cps).

The σ_γ for the 255.9-keV standardization peak was (0.1377 ± 0.0016) b. The corresponding calibration factor for the 255.9-keV γ-ray peak in the Nb$_2$O$_5$ spectrum was (1.317E-10 ± 0.016E-10) b/count. This σ_γ was also calculated using the previous NbCl$_5$ measurement. The effective thickness was found to be 1 mm using the 436-

and 1951.1-keV ^{36}Cl peaks, which is roughly half of the 0.6 cm^2/g thickness [7], and resulted in a 2.2% increase in the standardization σ_γ. The (0.1509 ± 0.0025) b σ_γ from the previous spectrum is 9.6% higher that the value obtained in the new NbCl$_5$ measurement. Since the neutron spectrum was the main difference in these two measurements – a thermal-neutron spectrum in the previous measurement and a cold-neutron spectrum in the new measurement – accounting for the neutron spectral influences on the ^{93}Nb and ^{35}Cl reaction rates could explain the difference in the standardization. Figure 4.8 suggests that the effective g-factor is slightly greater than 1 for ^{93}Nb(n,γ) and negligibly less than 1 for ^{35}Cl(n,γ), which could close the gap between the two measurements. Table 4.4 presents the efficiency-corrected peak areas, $A_\gamma/\epsilon(E_\gamma)$, self-absorption fractions, F_γ, effective g-factors, $\hat{g}$, for the 255.9- and 1951.1-keV γ-ray peaks from the previous and new NbCl$_5$ spectra. For the previous measurement, the Westcott g-factors were calculated for niobium and chlorine using a Maxwell-Boltzmann distribution of thermal neutrons at 293 kelvin. These had minimal impact on the σ_γ for the previous measurement, but could be missing the contribution of epithermal neutrons in resonance capture. Due to the lack of first-hand knowledge about the experimental details, the standardization σ_γ from this measurement was selected for use in this work.

Table 4.4: Comparison of the niobium standardization using the previous and new NbCl$_5$ spectra.

E_γ (keV)	$A_\gamma/\epsilon(E_\gamma)$	F_γ (b)	$\hat{g}$	σ_γ
Previous measurement				
1951.1	4.242E+09 ± 0.5%	0.988 ± 0.001	0.9999 ± 0.0001	6.51 ± 0.04
255.9	1.926E+07 ± 1.4%	0.967 ± 0.004	1.0014 ± 0.0010	0.1509 ± 0.0025
New measurement				
1951.1	9.5823E+09 ± 0.4%	0.993 ± 0.001	1.0000 ± 0.0000	6.51 ± 0.04
255.9	3.9738E+07 ± 0.8%	0.980 ± 0.004	0.9937 ± 0.0010	0.1377 ± 0.0016

The γ-ray intesities from the Nb_2O_5 were normalized into σ_γ using the the 255.9-keV standardization peak. In the next section, these σ_γ were compared with normalized ENSDF data.

4.1.5 Energy and Intensity Comparison

Primary γ-rays

The ENSDF primary γ-ray data were from the experiment by Kennett et al in which high-statistical precision was obtained by irradiating niobium powder for 450 hours in tangential beam of the 2 MW McMaster research reactor [33]. 334 γ-rays with energy greater than 3.9 MeV were associated with niobium neutron capture. The 5103.33(12)-keV γ-ray, with 1560(25) intensity per 10^5 neutron captures, was the most intense. This γ-ray energy was used for energy calibration in this work.

In this work, 290 of the 334 γ-rays were identified. The intensities were adopted from normalized ENSDF values for missing γ-rays and when background interferences were found. The missing γ-rays could have been missed in the automatic peak fitting due to their very weak intensities. The sum of the σ_γ for these 334 γ-rays was 0.587(38) b. This was statistically similar the 0.579(21) b value obtained by normalizing the ENSDF data with the 0.01749(30) b σ_γ for the 5103.33-keV γ-ray. The sum of the primary σ_γ was significantly less than the 1.15(5) b σ_0 in literature [28], which exemplifies the reason why statistical modeling of γ-ray cascades is important for estimating the contribution of quasi-continuum γ-rays. Table 4.5 shows the data from this measurement compared to the normalized ENSDF data for primary γ-rays feeding levels below 1 MeV. The ENSDF data were significantly higher than those determined in this work. This was not a concern for the statistical model calculations since only a few of the most intense primary γ-ray intensities were more 1 percent of the total intensity. The neutron separation energy based on the primary γ-ray feeding

the ground state was 7227.61(29) keV after correction for nucleus recoil, which is in agreement with ENSDF.

Table 4.5: Comparison of primary γ-rays feeding levels below 1 MeV measured in this work to those in ENSDF.

ENSDF [33]		This Work				
E_γ	σ_γ	E_γ	E_f	ΔE	σ_γ	$\Delta\sigma_\gamma$ (%)
6,257.25(14)	0.00061(2)	6,256.96(28)	970.43	0.30	0.00057(5)	-5.3
6,270.57(11)	0.00082(3)	6,270.09(28)	957.29	0.48	0.00046(5)	-43.9
6,292.19(7)	0.00312(9)	6,292.06(17)	935.32	0.13	0.00282(10)	-9.5
6,331.74(7)	0.00256(7)	6,331.70(18)	895.68	0.04	0.00210(9)	-17.7
6,410.64(14)	0.00056(2)	6,410.78(29)	816.59	-0.14	0.00046(5)	-18.8
6,434.78(6)	0.00314(9)	6,434.63(18)	792.74	0.15	0.00275(26)	-12.3
6,586.88(22)	0.00030(1)	6,585.80(48)	641.55	1.08	0.00017(5)	-44.4
6,595.97(6)	0.00198(6)	6,595.67(20)	631.68	0.30	0.00159(8)	-19.7
6,831.18(4)	0.01368(39)	6830.98(18)	396.35	0.20	0.01258(23)	-8.0
6,893.39(16)	0.00044(2)	6892.60(29)	334.74	0.80	0.00041(6)	-6.8
6,915.73(4)	0.00302(9)	6915.38(19)	311.95	0.35	0.00245(30)	-18.8
7,114.31(6)	0.00133(4)	7113.63(28)	113.69	0.69	0.00091(9)	-32.0
7,149.4(6)	0.00019(1)					
7,168.91(5)	0.00166(5)	7168.42(24)	58.89	0.49	0.00113 (8)	-31.6
7,186.54(2)	0.00764(22)	7186.30(19)	41.01	0.24	0.00724 (34)	-5.2
7,227.78(9)	0.00082(3)	7227.31(29)	0.00	0.47	0.00034 (4)	-58.5

Secondary γ-rays

The intensities of secondary γ-rays of ENSDF, EGAF and this work were compared after normalization to the 255.9-keV γ-ray intensity. The normalized intensities are shown in Table 4.6 for all significant γ-rays placed in the decay scheme below the 932 keV level. Δ is the relative difference of intensities to ENSDF. Missing values in this work had background interferences or were missing, and were adopted from normalized ENSDF data. The comparison of intensities are presented graphically in Figure

4.12. It is apparent that the previous EGAF data have significantly lower intensities for low-energy γ-rays, such as the 78.7-keV γ-ray. Overall, the data determined in this work were mostly within 1σ of the ENSDF data.
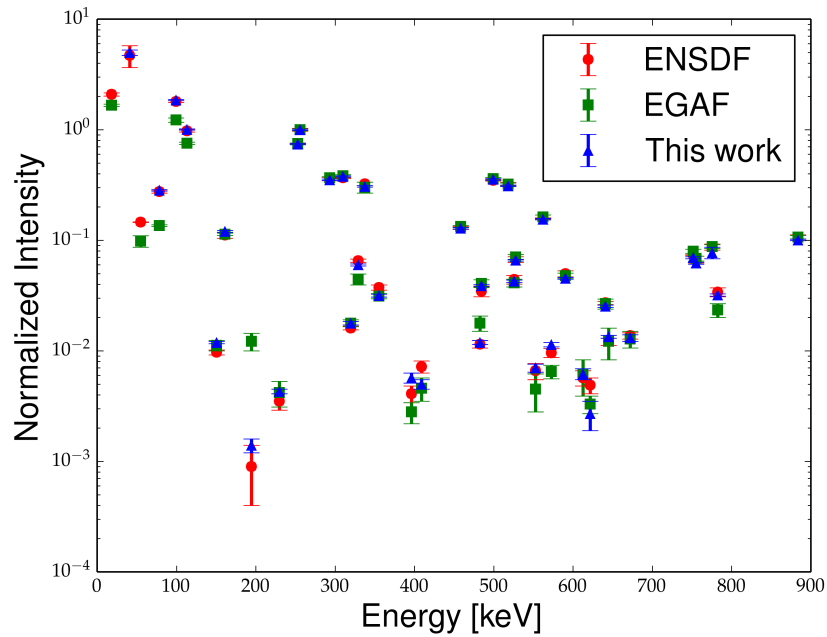

Figure 4.12: Comparison of intensities $\sigma_\gamma(1+\alpha)$ normalized to the 255.9-keV transition for ENSDF, EGAF and this work. Data that are adopted from ENSDF are omitted for this work.

Table 4.6: Comparison of normalized secondary γ-ray intensities

	ENSDF	EGAF		This work		
E_γ (keV)	$I_\gamma/I_{\gamma,255.9keV}$	$\sigma_\gamma/\sigma_{\gamma,255.9keV}$	Δ (%)	$\sigma_\gamma/\sigma_{\gamma,255.9keV}$	Δ (%)	
17.98	0.4113 ± 0.0276	0.3221 ± 0.0095	-21.7			
54.71	0.0489 ± 0.0029	0.0978 ± 0.0042	100.0			
78.67	0.1952 ± 0.0131	0.1357 ± 0.0028	-30.5	0.2007 ± 0.0039	2.8	$< 1\sigma$
99.41	1.6371 ± 0.1007	1.2233 ± 0.0541	-25.3	1.6876 ± 0.0319	3.1	$< 1\sigma$
113.40	0.8589 ± 0.0537	0.7547 ± 0.0209	-12.1	0.8850 ± 0.0165	3.0	$< 1\sigma$
138.61	0.0742 ± 0.0151	0.0495 ± 0.0106	-33.3			
140.10	0.0242 ± 0.0162	0.0126 ± 0.0012	-47.9			
161.26	0.1056 ± 0.0089	0.1135 ± 0.0034	7.5	0.1143 ± 0.0024	8.2	$< 1\sigma$
253.11	0.7460 ± 0.0437	0.7482 ± 0.0164	0.3	0.7443 ± 0.0138	-0.2	$< 1\sigma$
255.93	1.0000 ± 0.0666	1.0000 ± 0.0236	0.0	1.0000 ± 0.0184	0.0	$< 1\sigma$
293.21	0.3613 ± 0.0247	0.3669 ± 0.0108	1.5	0.3560 ± 0.0066	-1.5	$< 1\sigma$
309.91	0.3742 ± 0.0219	0.3883 ± 0.0115	3.8	0.3864 ± 0.0072	3.3	$< 1\sigma$
319.62	0.0165 ± 0.0012	0.0178 ± 0.0013	7.9	0.0181 ± 0.0007	9.7	$< 2\sigma$
329.17	0.0669 ± 0.0046	0.0445 ± 0.0051	-33.5	0.0611 ± 0.0016	-8.7	$< 2\sigma$
337.53	0.3298 ± 0.0227	0.3016 ± 0.0338	-8.6	0.3129 ± 0.0063	-5.1	$< 1\sigma$
355.36	0.0381 ± 0.0030	0.0313 ± 0.0017	-17.8	0.0321 ± 0.0011	-15.7	$< 3\sigma$
458.46	0.1323 ± 0.0087	0.1335 ± 0.0036	0.9	0.1314 ± 0.0026	-0.7	$< 1\sigma$
482.64	0.0117 ± 0.0011	0.0178 ± 0.0028	52.1	0.0122 ± 0.0005	4.3	$< 1\sigma$
484.36	0.0355 ± 0.0045	0.0406 ± 0.0034	14.4	0.0396 ± 0.0009	11.5	$< 1\sigma$
499.43	0.3565 ± 0.0215	0.3605 ± 0.0117	1.1	0.3630 ± 0.0067	1.8	$< 1\sigma$
518.12	0.3282 ± 0.0226	0.3221 ± 0.0090	-1.9	0.3181 ± 0.0064	-3.1	$< 1\sigma$
525.77	0.0452 ± 0.0048	0.0412 ± 0.0034	-8.8	0.0436 ± 0.0012	-3.5	$< 1\sigma$
527.57	0.0685 ± 0.0057	0.0707 ± 0.0041	3.2	0.0675 ± 0.0016	-1.5	$< 1\sigma$
562.34	0.1613 ± 0.0095	0.1630 ± 0.0067	1.1	0.1586 ± 0.0030	-1.7	$< 1\sigma$
590.60	0.0508 ± 0.0044	0.0478 ± 0.0029	-5.9	0.0463 ± 0.0010	-8.9	$< 2\sigma$
598.80	0.0116 ± 0.0011	0.0077 ± 0.0010	-33.6	0.0106 ± 0.0006	-8.6	$< 1\sigma$
641.05	0.0278 ± 0.0018	0.0267 ± 0.0028	-4.0	0.0258 ± 0.0007	-7.2	$< 2\sigma$
645.19	0.0123 ± 0.0011	0.0122 ± 0.0039	-0.8	0.0137 ± 0.0005	11.4	$< 2\sigma$
672.50	0.0140 ± 0.0013	0.0128 ± 0.0022	-8.6	0.0133 ± 0.0009	-5.0	$< 1\sigma$
751.78	0.0752 ± 0.0044	0.0796 ± 0.0036	5.9	0.0712 ± 0.0018	-5.3	$< 1\sigma$
755.28	0.0685 ± 0.0063	0.0684 ± 0.0035	-0.1	0.0635 ± 0.0016	-7.3	$< 1\sigma$
775.99	0.0887 ± 0.0077	0.0879 ± 0.0036	-0.9	0.0790 ± 0.0097	-10.9	$< 2\sigma$
782.57	0.0347 ± 0.0038	0.0234 ± 0.0034	-32.6	0.0327 ± 0.0009	-5.8	$< 1\sigma$
854.40	0.0125 ± 0.0013	0.0156 ± 0.0028	24.8	0.0130 ± 0.0007	4.0	$< 1\sigma$
883.80	0.1081 ± 0.0090	0.1068 ± 0.0043	-1.2	0.1030 ± 0.0021	-4.7	$< 1\sigma$
932.90	0.0105 ± 0.0017	0.0111 ± 0.0022	5.7	0.0128 ± 0.0008	21.9	$< 2\sigma$

4.2 Statistical Model Calculations

Extensive statistical model simulations with DICEBOX were conducted for the purposes of checking the experimental data and the nuclear structure evaluation. This section divided into four parts. The first discusses the adopted models used in the DICEBOX calculations. The second part used the ^{94}Nb decay scheme to investigate the nuclear structure evaluation. The third and fourth parts are devoted to determining σ_m and σ_0.

4.2.1 Adopted Models

The simulated populations of the levels below E_{crit} depend upon the assumed experimental decay scheme, the capture-state spin composition ($J = J_{gs}(\text{target})\pm 1/2$ for odd-odd and odd-A targets), and the choice of adopted level density (LD) and photon strength function (PSF) models.

Gilbert and Cameron [67] explored the energy dependence of the level density over the entire mass range with the CTF and BSFG models. Results indicated that that the level density is expected to follow the CTF model in the range of the ^{94}Nb excitation energy. Kennett et al. [33] found that the disposition of the 334 observed levels can be described by the CTF model. The enhanced generalized Lorentzian (EGLO) [74] and the constant temperature formula (CTF) [67] models were selected for the $E1$ PSF and LD models, respectively. All level density parameters used in this work, summarized in Table 4.7, were taken from von Egidy and Bucurescu [1] in which these parameters were determined by fitting function forms of the CTF and BSFG models (Equations 3.20 and 3.20, respectively) to experimentally-observed neutron resonance spacings in the region of the capture state above the neutron-separation energy.

Table 4.7: Level density parameters for the CTF (T and E_0) and BSFG (a and E_1), pairing energies (Δ), and average resonance spacings (D_0) used in the [94]Nb simulations with DICEBOX, taken from Ref. [1].

T [MeV]	E_0 [MeV]	a [MeV^{-1}]	E_1 [MeV]	Δ [MeV]	D_0 [eV]
0.86	-2.44	10.880	-1.37	1.129	84.8(46)

PSF Parameters

In this section, the parameters for fitting the GDER are discussed. These parameters, which drive the shape of the fitting, are the centroid of the GDER (E_{G_i}, [MeV]), the width of the resonance (Γ_{G_i}, [MeV]) and the cross section of the resonance (σ_{G_i}, [mb]). For the statistical model calculations, the low energy portion of PSF predictions is most important, but there the experimental data are limited to non-existent. Furthermore, predictions are different at low energy region for different models. From experience, predicted population for levels from DICEBOX simulations are less affected by these changes. A sensitivity study was conducted for this study to find out how the parameterization of the PSF for [94]Nb has on the overall population-depopulation plot as well as fitting to the absorption data and reproduction of the total gamma width.

Total photonuclear cross-section data derived from [93]Nb photoabsorption measurements by Lepretre et al [75] can be used to test the validity for a variety of PSFs near the GDER. The (γ,abs) experiment conducted measured two components of the overall absorption cross sections:

1. (γ,n) + (γ,np)

2. (γ,2n).

The (γ,2n) process is a weaker contribution that only affects the higher-energy portion of the spectrum. Thus, it should have insignificant influence on the part of the

spectrum of interest. For this reason, the data from the $(\gamma,n)+(\gamma,np)$ spectrum was used for comparison. Lepretre et al stated that the total photoneutron cross sections were fit for the data in the range of 14-18 MeV to establish the parametrization of the GDER. These parameters are shown in Table 4.8, along with:

- The parameters from the "Atlas of Photoneutron Cross Sections Obtained With Monoenergetic Photons" by Dietrich and Berman [76]. Though the work by Lepretre et al is cited as the source, the parameterizations are different and thus considered for this work.

- The default parameters used by DICEBOX. In the absence of experimental parameterization – as is the case for ^{94}Nb – the scripts used by DICEBOX search for the nearest neighboring nucleus of the type, which is the odd-Z $_{37}$Rb. The Rb data are from the measurement of a natural-abundance sample of Rb (^{nat}Rb) by Lepretre et al.

- Parameters determined by fitting the BA function to the photoabsorption data in the 14-18 MeV (recommended by Lepretre et al.) to establish the parametrization of the GDER. Figure 4.13 shows the fit of the BA function and the other PSF models using the parameterization determined by the fit.

Table 4.8: Lorentz GDER resonance parameters for ^{94}Nb.

E_{G_1} [MeV]	Γ_{G_1} [MeV]	σ_{G_1} [mb]	Ref.
16.5 ± 0.05	4.7 ± 0.2	202 ± 10	Lepretre et al [75]
16.59	5.05	200	Dietrich et al [76]
16.58	4.95	200.4	RIPL-3 (for SLO) [11]
16.70	5.18	198.6	RIPL-3 (for MLO) [11]
16.80	4.47	190.0	^{nat}Rb [76]
16.29 ± 0.01	4.07 ± 0.05	199.9 ± 1.0	Fit to (γ, abs) data: 14-18 MeV (γ,n)
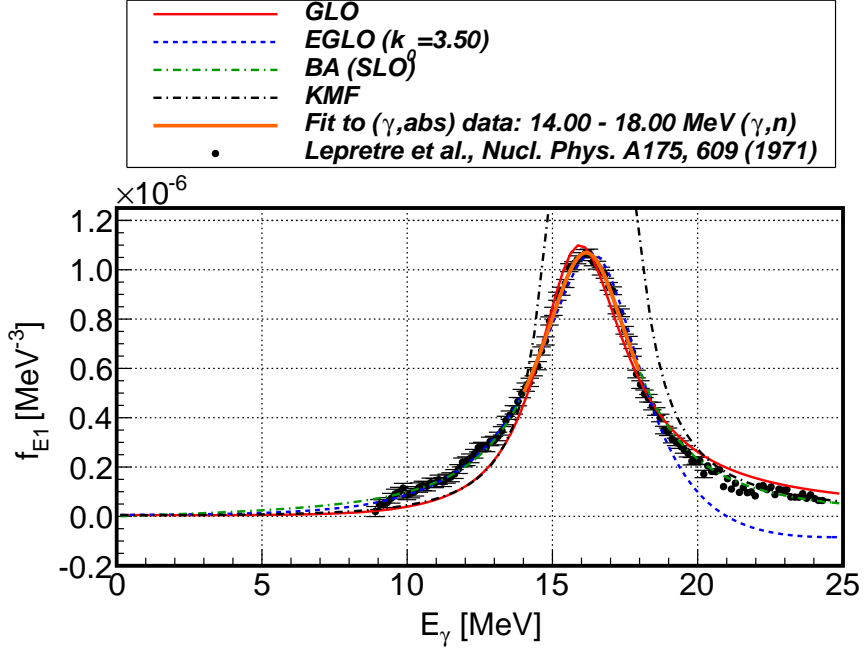
Figure 4.13: The fitting of the experimental photoabsorption data in the 14-18 MeV range and the various PSFs using the parametrization of the fit.

Figure 4.14 shows the EGLO with the parameters in the Table 4.8. The parameterization (with $k_0 = 3.5$) from fitting the BA function resembles the PSF from experimental data in the range from E_γ above 10 MeV and is quite similar to the default parameterization in DICEBOX from ^{nat}Rb.

To test the sensitivity of the final results to the parameterization of EGLO, DICE-BOX simulations were done for the assuming EGLO/CTF for the PSF/LD model combinations for parameters from 1) Lepretre et al, 2) ^{nat}Rb and 3) the BA fitting. The ENSDF intensity data were normalized to the 0.0648(18) b [4] cross section of the 499.4 keV peak. The sensitivity study focused on the total radiative capture width Γ_0, which has a literature value $\Gamma_0 = 0.173 \pm 0.004$, and the probability $P(GS)$ that the ground state is fed directly from the continuum above E_{crit}. The results
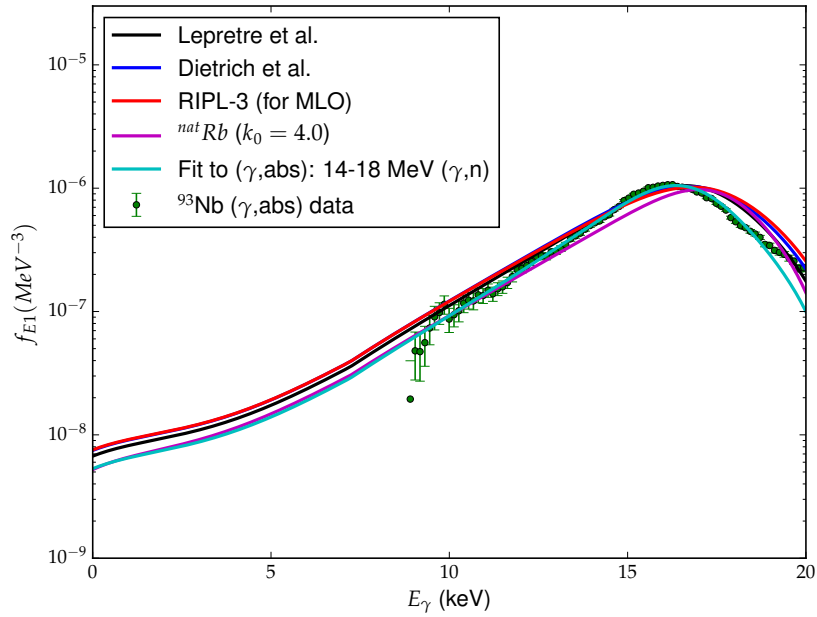
Figure 4.14: The EGLO function with the parameters in Table 4.8 compared to the experimental data. The k_0 enchancement factor was assumed to be 3.5 except for the ^{nat}Rb, which has a default of 4.0 in RIPL.

were largely insensitive to the parameters. The parameters from the fitting of the experimental data were adopted.

4.2.2 Capture-state Spin Distribution

The ground state of the ^{93}Nb target nucleus is $J^{\pi} = 9/2^{+}$, allowing s-wave neutron capture to populate resonances with $J^{\pi} = 4^{+}$, 5^{+}. The *Atlas of Neutron Resonances* [28] indicates the that 4^{+} and 5^{+} account for 2.1% and 5.9% of the observed total-capture cross section, respectively. The remaining 92% of the cross section is attributed to *bound* resonances at $E_0 = $ -129.6 eV and $E_0 = $ -255.4 eV (with respect to the separation energy) with spin-parities of 4^{+} and 5^{+}, respectively. Thus, the capture-state spin distribution is assumed to be unknown and ranges from $J^{\pi} = 4^{+}(2.1\%) + 5^{+}(97.9\%)$ to $J^{\pi} = 4^{+}(94.1\%) + 5^{+}(5.9\%)$.

Insights into the capture-state spin distribution can be found in the primary γ-rays depopulating the capture state. With $J^{\pi}_{CS} = 4^{+}, 5^{+}$, both the 7^{+} and 2^{+} states are weakly populated by $E2$ primary transitions. The following suggest that the predominant capture state is 4^{+}:

- the relative weakness of the primary γ-rays to the 6^{+} ground state to the relative strength of those to the 3^{+} isomeric state;

- and, likewise, the relative weakness of those to the 7^{+} [33] to the relative strength of those to the 2^{+} state (assumed here as the 334.1-keV level) – both of which are very weak, as would be expected for $E2$ transitions.

Since the cross sections of these bound resonances are unknown, the capture-state spin compositions were varied in DICEBOX simulations in order to choose an appropriate capture-state fraction. In this section, the aim is to investigate capture-state spin composition.

The experimental decay scheme for this study was performed with the decay scheme developed in this work with E_{crit} selected as 396.2 keV, which included 9 levels above the ground state. The σ_{γ} data were adopted from normalized ENDSDF values

for the 17.98-, 40.90-, 54.71- and 148.69-keV γ-rays. Though the J^π assignments were tentative except for the ground state and the 40.9-keV level, DICEBOX simulations and analysis of the level scheme and literature had shown that the assignments were less ambiguous than appears. Figure 4.15 shows the corresponding decay scheme below E_{crit}. The 301.6- and 334.1-keV levels were assumed as $J^\pi = 1^-$ and 2^+, respectively, as was found in the following section.
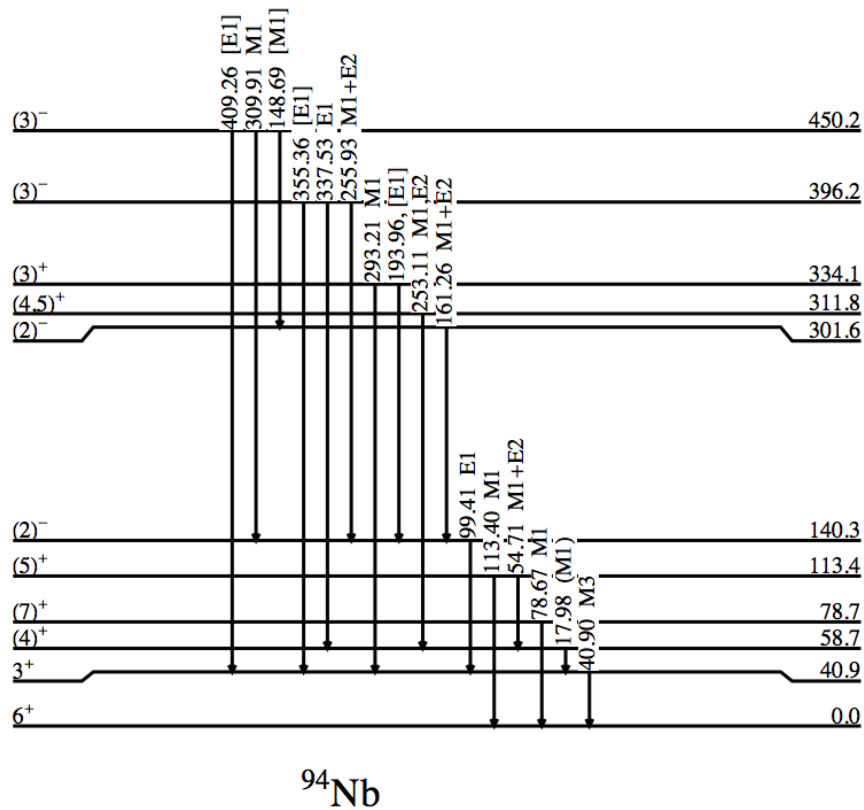
Figure 4.15: The ENSDF [6] level scheme below $E_{crit} = 450 keV$.

The effect of the assumed capture-state spin distribution was investigated for the four combinations of PSF/LD models: EGLO/BSFG, EGLO/CTF, BA/BSFG and

BA/CTF. DICEBOX simulations with 50 nuclear realizations and 50,000 cascades were performed for each PSF/LD combination with capture-state spin distributions between $J^\pi = 4^+(40\%) + 5^+(60\%)$ and $J^\pi = 4^+(94.1\%) + 5^+(5.9\%)$. The main considerations in estimating the capture-state spin distribution were the total radiative width and the consistency of the population-depopulation plots. The population-depopulation plots are shown in Figure 4.16 for the EGLO/CTF and EGLO/BSFG model combinations and Figure 4.17 for the BA/CTF and BA/BSFG model combinations. The EGLO/BSFG and EGLO/CTF model combinations both produced consistent population-depopulation plots, whereas it is apparent that the BA/BSFG and BA/CTF model combinations under-populate the negative-parity levels. The effects of the model choices and capture-state spin distribution on continuum feeding of the ground state and first-excited state and on the thermal neutron capture cross section are shown in Figure 4.18 and Figure 4.19(a), respectively. Figure 4.19(b) shows the total radiative width Γ_0 versus the capture-state spin distribution for the various PSF/LD model combinations. The EGLO/CTF model combination was found to have the best agreement with the literature value of 0.173 ± 0.004 eV [28] and adopted as the models going forward.
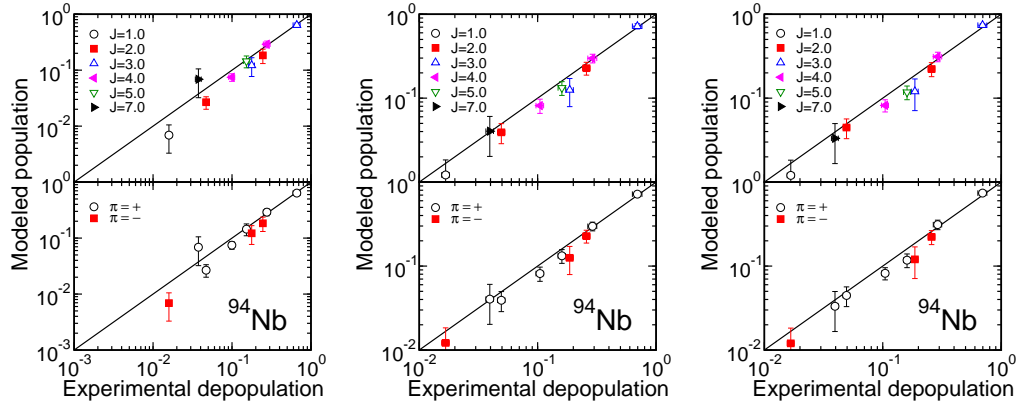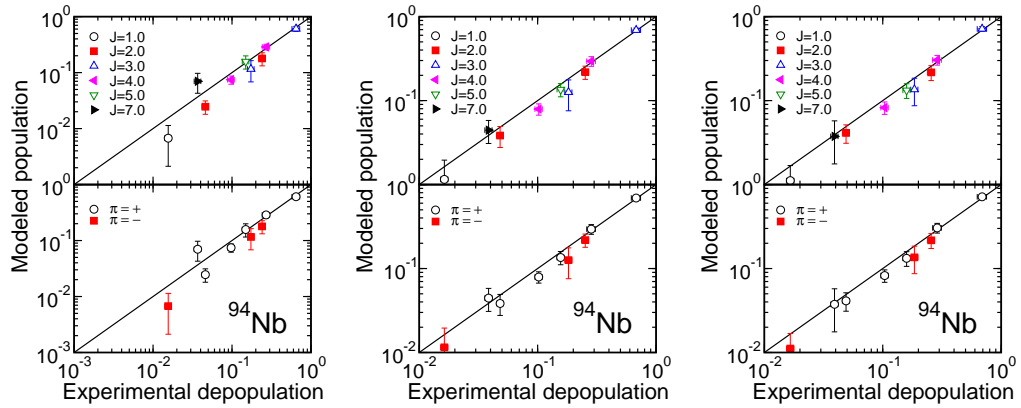
Figure 4.16: Depopulation-population plots for various capture-state spin distributions with $E_{crit} = 396.2 keV$ for the EGLO/CTF and EGLO/BSFG PSF/LD model combinations.
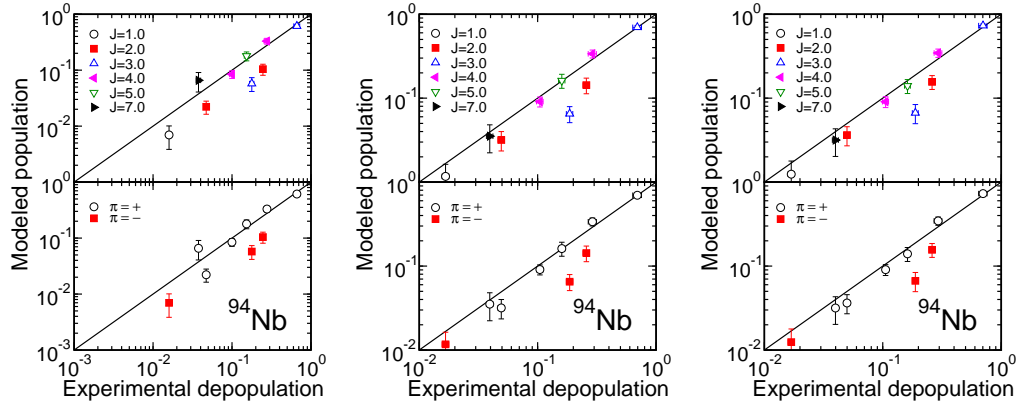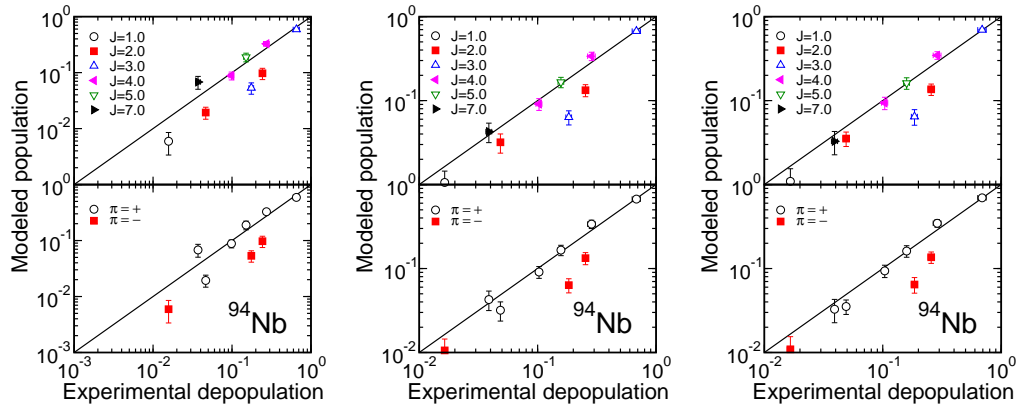
Figure 4.17: Depopulation-population plots for various capture-state spin distributions with $E_{crit} = 396.2 keV$ for the BA/CTF and BA/BSFG PSF/LD model combinations.

76
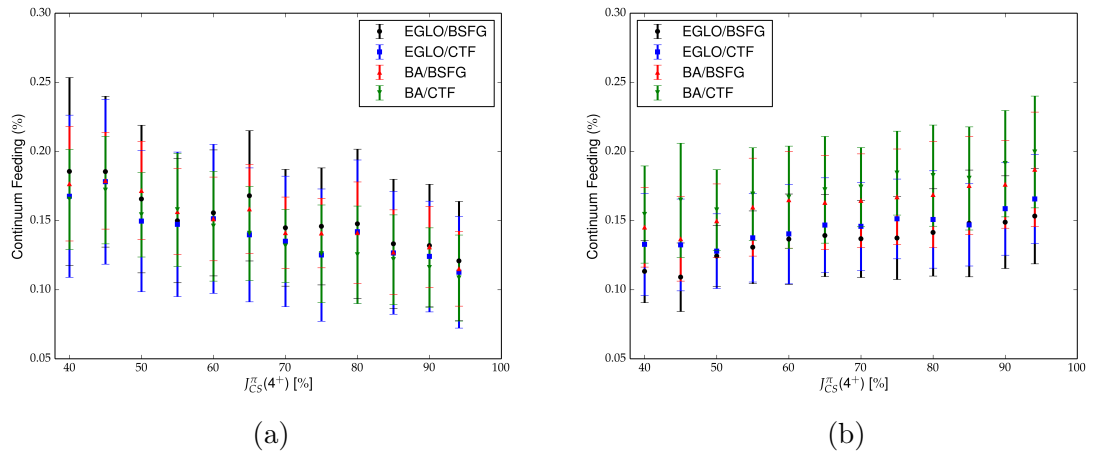
Figure 4.18: Continuum feeding of the ground state (a) and lowest-lying level (b) for the various PSF/LD model combinations.
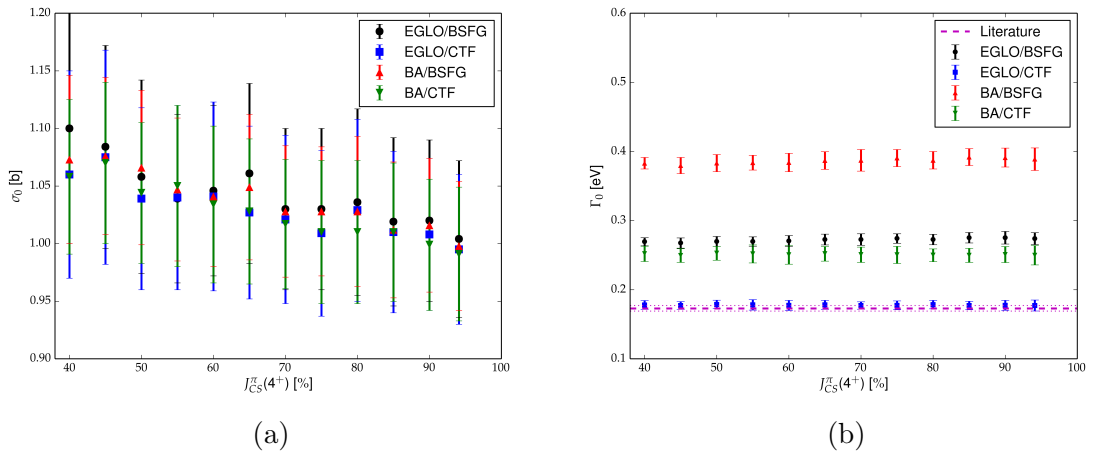
Figure 4.19: The (a) thermal neutron capture cross section (σ_0) and (b) total radiative width (Γ_0) versus the capture-state spin distribution for the various PSF/LD model combinations.

Lastly, the differences in modeled population P_L^{sim} and experimental depopulation P_L^{exp} of the 7^+ and 2^+ for the various capture-state spin distributions were plotted as shown in Figure 4.20. As expected, the modeled population of the 7^+ state decreased as the capture-state spin distribution shifted toward 4^+ while that of the 2^+ state increased. These results indicate that $J_{CS}^\pi(4^+)$ is likely greater than 75%.
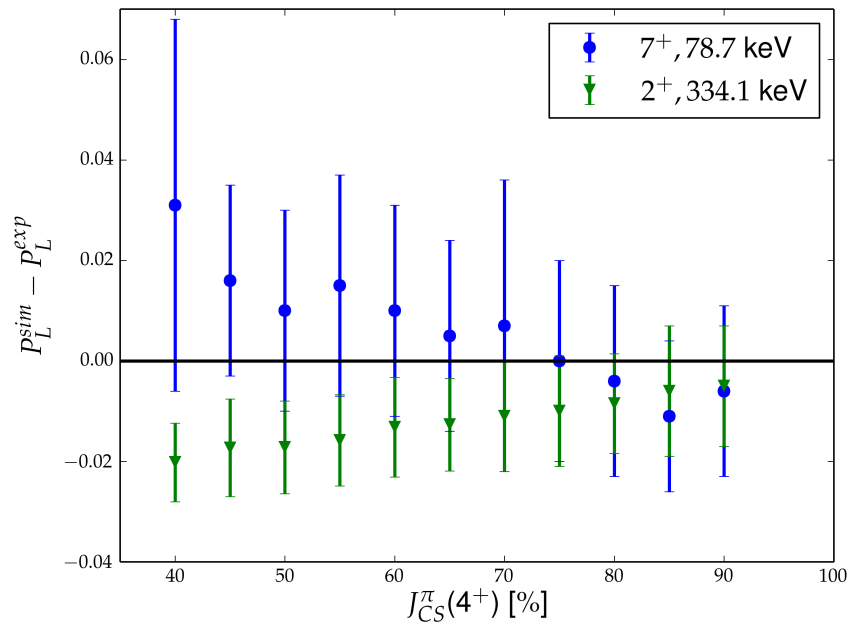
Figure 4.20: Differences in modeled population P_L^{sim} and experimental depopulation P_L^{exp} of the 7^+ and 2^+ states for various capture-state spin distributions.

4.2.3 Investigation of Level Scheme

Figure 4.21 shows the cumulative plot of known ^{94}Nb discrete levels with increasing excitation energy. The line at 40.9 keV indicates N_c, the number of levels with complete spin and parity – that is, only two levels in the ^{94}Nb level scheme, the
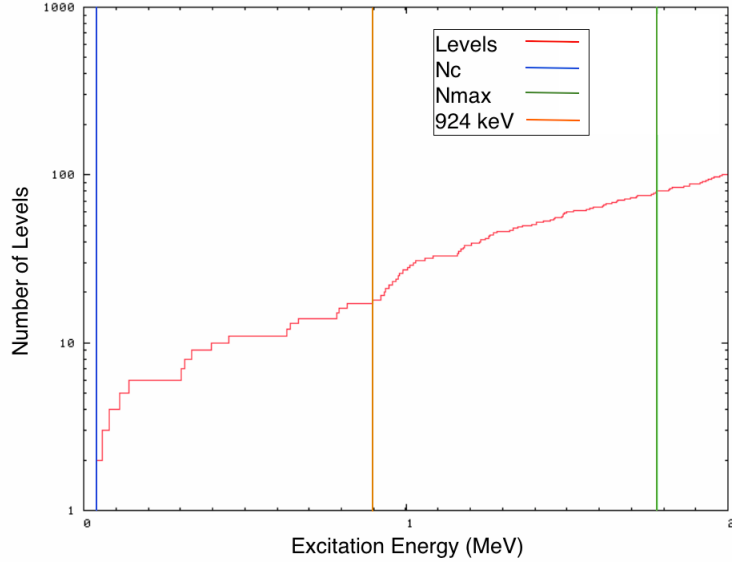
Figure 4.21: The cumulative plot of known ^{94}Nb discrete levels with increasing excitation energy.

ground state and the metastable state at 40.9 keV, have assigned spin and parity. The remaining levels have tentatively assigned spin and/or parity. Since there is an decrease in the level spacing and missing tentative J^π assignments above 924 keV, the focus of this section is to develop the level scheme for the 19 levels up to 924 keV level with the standardized σ_γ data measured in this work. The multipolarities for transitions, where missing, were assumed from selection rules for the purpose of calculating ICCs using the BrIcc calculator, though these were expected to have minimal impact.

In this section, I perform DICEBOX simulations starting with $E_{crit} = 40.9 keV$, the lowest-lying level, and increase E_{crit} by one level up to 817 keV. DICEBOX-simulation results are compared to experimental data by plotting the modeled population against the experimental depopulation for each level below E_{crit} in population-depopulation plots. For the purpose of investigating the level scheme consistency and

J^π assignments, the following capture-state spin distributions were compared for each iteration of the level scheme:

- $J_{CS}^\pi = 4^+(60\%) + 5^+(40\%)$

- $J_{CS}^\pi = 4^+(75\%) + 5^+(25\%)$

- $J_{CS}^\pi = 4^+(90\%) + 5^+(10\%)$.

The DICEBOX simulations were performed with 50 realizations consisting of 50,000 cascades.

The factors affecting the simulated population and experimental depopulation of each level are discussed. At the onset, it is worth noting that the parity assignments were firm for 17 levels up to $E_{crit} = 816.83$ keV. Thus, the main factor from the aspect of nuclear structure is the spin assignment. The spin assignments, where necessary, were adjusted within the selection rules of known multipolarities. Since the spin assignments above E_{crit} were also tentative, the main consideration in adjusting the spin assignment was the decay scheme below E_{crit}, which had DICEBOX-simulation results confirming or suggesting correct J^π assignments.

6^+ Ground State

Until recently, the J^π assignment was not certain with an adopted value $(6)^+$ [77]. Support for this assignment comes from the ^{93}Nb$(d, p)^{94}$Nb experiment [34], the $M3$ γ-ray transition from $J^\pi = 3^+$ and the beta decay only to 4^+ with a $log_{10}ft = 12.0$ [6]. The value 6^+ was adopted by Marginean et al for their analysis of heavy-ion vapor-evaporation measurements [37], citing shell model calculations predicting a 6^+ ground state and a low-lying 7^+ state.

40.9-keV Level

The 40.892(12)-keV level is the lowest-lying and highest-populating level. It is a metastable-excited state with a half life of (6.263 ± 0.004) minutes[78]. Support in the firm J^π assignment 3^+ comes from the ^{93}Nb$(d,p)^{94}$Nb experiment [34], the $M3$ γ-ray transition from $J^\pi = 3^+$ and beta decays to 2^+ with a $log_{10}ft = 7.4$ and 4^+ with a $log_{10}ft = 7.4$[6]. The transition to the ground state is dominated by internal conversion electron emission with the ICC value 1366, with the $\alpha(K)$ value 784, in ENSDF [78]. The BrIcc Frozen Orbital approximation was adopted for calculation of all ICCs in this evaluation. The resulting ICCs for the 40.9-keV M3 transition are a 1323(19) total α with shell contributions $\alpha(K) = 766(11)$, $\alpha(L) = 456(7)$, $\alpha(M) = 88.8(13)$, $\alpha(N) = 12.11(17)$ and $\alpha(O) = 0.353(5)$. The 40.9-keV γ-ray, below the low-energy threshold in our measurement, is difficult to experimentally observe due to the very high ICC. The ENSDF intensity (per 100 neutron captures) for this γ-ray is 0.045(10) [31]. As with other γ-ray transitions not observed in this work or interfered with by background, the ENSDF intensity was normalized to a σ_γ of 0.00050(11) b using the 255.9-keV σ_γ. However, the large relative error (22 percent) of this σ_γ resulted in a large uncertainty in the σ_0 determined by DICEBOX simulations. Consequently, the σ_γ for the 40.891-keV level was determined as the balance of the level feeding using the σ_γ data determined in this work.

The depopulation-population plots with $E_{crit} = 40.9 keV$ are shown in Figure 4.22. The results gave insight into the effect of capture-state spin distribution on the continuum feeding of the 6^+ ground state and 3^+ 40.9-keV level. Table 4.9 shows the comparison of DICEBOX-simulation results for the three capture-state spin distributions. Feeding of the 6^+ ground state is favored by the statistical model when the capture-state spin distribution was skewed toward 5^+, while the same is true with the 3^+ 40.9-keV level when skewed to the 4^+ capture-state.

(a) $4^+(60\%) + 5^+(40\%)$ (b) $4^+(75\%) + 5^+(25\%)$ (c) $4^+(90\%) + 5^+(10\%)$
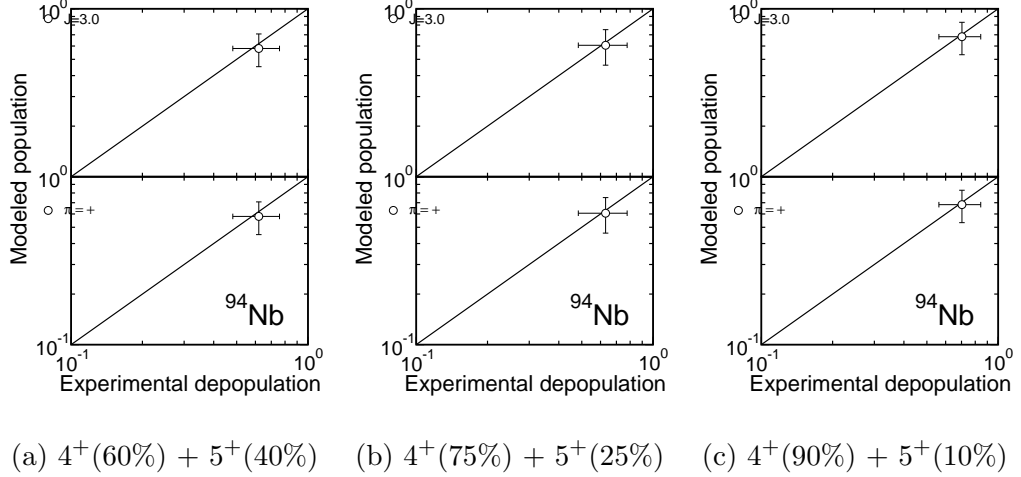
Figure 4.22: Population-depopulation plots for various capture-state spin distributions with $E_{crit} = 40.9$ keV.

Table 4.9: Comparison of results for DICEBOX simulations assuming different PSF parameterizations

	Continuum feeding			
$J_{CS}^{\pi}(4^+)[\%]$	G.S.	40.9 keV	$P_L^{sim} - P_L^{exp}$	σ_0
60	0.37980 ± 0.13364	0.58004 ± 0.12792	-0.04 ± 0.19	1.11 ± 0.24
75	0.36943 ± 0.14232	0.60625 ± 0.14483	-0.02 ± 0.21	1.09 ± 0.25
90	0.29667 ± 0.13509	0.68154 ± 0.14884	-0.02 ± 0.21	0.98 ± 0.19

58.7-keV Level

The 58.7-keV level has the tentative spin assignment in $J^{\pi} = (4)^+$. Support for the spin assignment of 4 comes from the $^{93}\text{Nb}(d,p)^{94}\text{Nb}$ experiment [34] and primary γ-ray feeding from a 5^- resonance. The 17.98-keV γ-ray from this level feeds the 3^+ 40.9-keV level with σ_γ of 0.0566(27) b adopted from renormalized ENSDF data [31]. The multipolarity can only be $M1$, as tentatively assigned, on the basis of depopulation-population in DICEBOX results; the ICC for $E2$ multipolarity is 563(8) – contrasted with the 4.18(6) ICC for the $M1$ multipolarity – would disturb the

intensity balance for the level and rule out the possibility that the level has spin greater than 4. Though $J = 3$ produced a consistent depopulation-population, the feeding to this level from the 5^- resonance, which can only be $E1$, rules out the possibility. The DICEBOX results, with population-depopulation shown in Figure 4.23, support the 4^+ assignment.

(a) $4^+(60\%) + 5^+(40\%)$ (b) $4^+(75\%) + 5^+(25\%)$ (c) $4^+(90\%) + 5^+(10\%)$

Figure 4.23: Population-depopulation plots for various capture-state spin distributions with $E_{crit} = 58.7$ keV with $J^\pi = 4^+$ for the 58.7-keV level.

78.7-keV Level

The 78.7-keV level has an $M1$ transition, based on the ICC measurement [31], to the 6^+ ground state, suggesting $J^\pi = (5, 6, 7)^+$. However, J = (7) was suggested on the basis that is the only candidate for the shell-model expectation of a low-lying 7^+ state [34][30]. The level was not observed in the (p,nγ) reaction, suggesting J>6. It was suggested that cascade seen in the heavy-ion vapor-evaporation measurements represents the yrast positive-parity sequence with the $J^\pi = 7^+$ for this level [37]. The

DICEBOX results, with population-depopulation shown in Figure 4.24, support the 7^+ assignment.

(a) $4^+(60\%) + 5^+(40\%)$ (b) $4^+(75\%) + 5^+(25\%)$ (c) $4^+(90\%) + 5^+(10\%)$

Figure 4.24: Depopulation-population plots for various capture-state spin distributions with $E_{crit} = 78.7$ keV with $J^\pi = 7^+$ for the 78.7-keV level.

Since the 78.7-keV γ-ray with 0.443(7) ICC is the only transition depopulating this level, insights can be gained from the intensity balance of this level. DICEBOX simulations revealed that depopulation-population was consistent with the capture-state spin distribution skewed toward the 4^+ capture-state; otherwise, the modeled population of this level was higher than experimental depopulation. Thus, the balance of this level suggests that $J^\pi = 4^+$ comprises greater than 75% of the capture state.

113.4-keV Level

The 113.4-keV level has γ-rays feeding the 6^+ ground state and $(4)^+$ 58.7-keV level, both of which are $M1$ transitions; thus, selection rules dictate that $J^\pi = 5^+$ for this

level. Additionally, this level was suggested as a possible member of the ground-state multiplet [34][30][31]. The population-depopulation plots in Figure 4.25 show consistency for the three capture-state spin distributions.

(a) $4^+(60\%) + 5^+(40\%)$ (b) $4^+(75\%) + 5^+(25\%)$ (c) $4^+(90\%) + 5^+(10\%)$

Figure 4.25: Population-depopulation plots for various capture-state spin distributions with $E_{crit} = 113.4$ keV with $J^\pi = 5^+$ for the 113.4-keV level.

140.3-keV Level

The 140.3-keV level is the first with negative parity and has a tentative spin assignment $J = (2)$ based on an $E1$ transition to the 3^+ 40.9-keV level and Hauser-Feshbach calculations in (p,nγ) data [35][36]. The lack of primary feeding, which must be $E1$ in nature, supports $J < 3$. DICEBOX results, shown in Figure 4.26, indicate population-depopulation agreement for this spin assignment. Furthermore, the simulations with $J^\pi_{CS} = 4^+(75\%) + 5^+(25\%)$ show good agreement for all five levels.

(a) $4^+(60\%) + 5^+(40\%)$ (b) $4^+(75\%) + 5^+(25\%)$ (c) $4^+(90\%) + 5^+(10\%)$
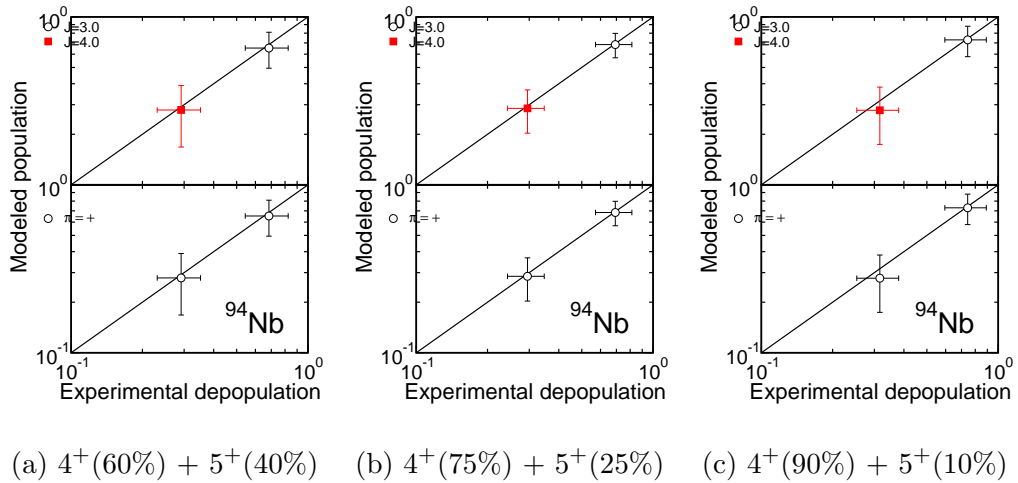
Figure 4.26: Depopulation-population plots for various capture-state spin distributions with $E_{crit} = 140.3$ keV with $J^\pi = 2^-$ for the 140.3-keV level.

301.6-keV Level

With the $M1 + E2$ transition to the $(2)^-$ 140.3-keV level, the 301.6-keV level could have $J^\pi = (1, 2, 3)^-$ based on selection rules. J^π was tentatively assigned as $(2)^-$ based on Hauser-Feshbach calculations in (p,nγ) data [36]. The lack of primary γ-rays feeding this level supports $J < 3$. With only the 161.3-keV γ-ray with 0.0157(3) b σ_γ and 0.0741(23) ICC (and no other unplaced γ-rays to assign to this level), modeled population far exceeds the experimental depopulation for the $J = 2$ spin assignment. On the other hand, the $J = 1$ spin assignment, being further from the capture state, shows better agreement in population-depopulation. If this level is $J^\pi = 1^-$, the 140.3- and 301.6-keV levels could form the negative-parity doublet with $J^\pi = 1^-, 2^-$ predicted by the shell model with the interaction $\pi(2p_{1/2})^{-1}_{1/2} \otimes v(2d_{5/2})^3_{3/2}$. A necessary consideration is that the 301.6-keV level is fed by the $M1$ γ-ray transition from the 450.2-keV level with $J^\pi = (3)^-$, which must be $J^\pi = (2)^-$ in adherence with selection rules. As discussed later, DICEBOX simulations support this change to $J^\pi = 2^-$.

86

Thus, DICEBOX results shown in Figure 4.27 support $J^\pi = 1^-$ for the 301.6-keV level, and this change is consistent with the available nuclear structure information.

(a) $J^\pi = 1^-$
$4^+(60\%) + 5^+(40\%)$

(b) $J^\pi = 1^-$
$4^+(75\%) + 5^+(25\%)$

(c) $J^\pi = 1^-$
$4^+(90\%) + 5^+(10\%)$
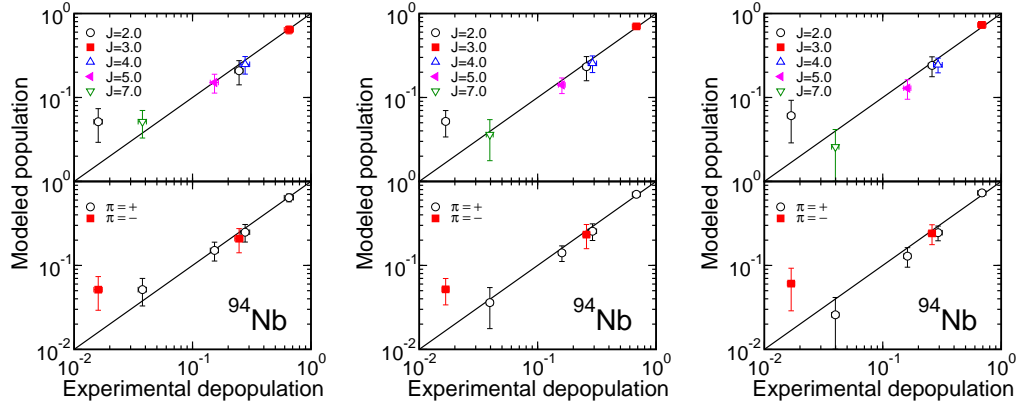
(d) $J^\pi = 2^-$
$4^+(60\%) + 5^+(40\%)$

(e) $J^\pi = 2^-$
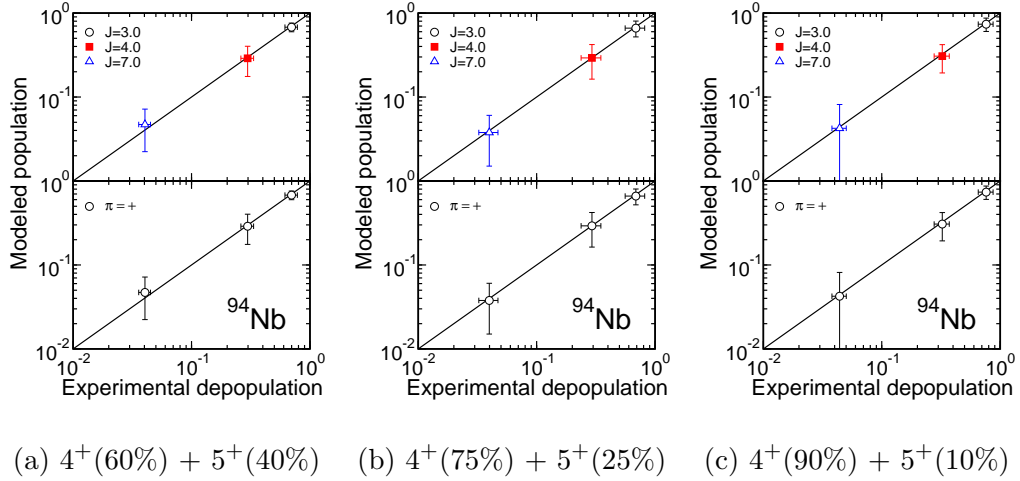$4^+(75\%) + 5^+(25\%)$

(f) $J^\pi = 2^-$
$4^+(90\%) + 5^+(10\%)$

Figure 4.27: Population-depopulation plots for various capture-state spin distributions with $E_{crit} = 301.6$ keV and $J^\pi = 1^-$ and 2^- for the 301.6-keV level.

311.8-keV Level

This level is fed by primary γ-rays from a 5^- resonance and feeds the $(4)^+$ 58.7-keV level with a 253.1-keV γ-ray. The $E2$ multipolarity was assigned by Bogdanovic et al. [31] based on the measured internal conversion electron intensities and comparison to the Hager-Seltzer ICC (HsIcc) values. The measured 0.033(12) $\alpha(K)$ was relative to the HsIcc-calculated 789(11) $\alpha(K)$ for the 40.9-keV γ-ray. Since ICC cannot be calculated for E_γ above 150 keV using the HsIcc treatment, the BrIccFO calculated values for the $E2$ and $M1+E2$ multipolarities were 0.0412(13) and 0.026(10), respectively, for the K-shell ICCs. It was assumed that the transition is mixed-multipolarity $M1 + E2$ on the basis of the ICC, which was supported by DICEBOX results that indicate low modeled population if the $J^\pi = 6^+$. Thus, the level could be $J^\pi = (4, 5)^+$ [6]. Jurney et al calculated the positive-parity levels using theory to correctly predict the five low-lying positive-parity levels as well as a doublet of 5^+ and 2^+ levels at around 350 keV, isolated from other positive-parity states [30]. Based on the DICE-BOX population-depopulation plots shown in Figure 4.28 for these two possibilities, the $J^\pi = 4^+$ had better agreement with the three capture-state spin distributions considered. The $J^\pi = 5^+$ possibility should be considered if the J^π_{CS} is skewed toward populating the 5^+ state; however, the results thus far suggest that is not the case.
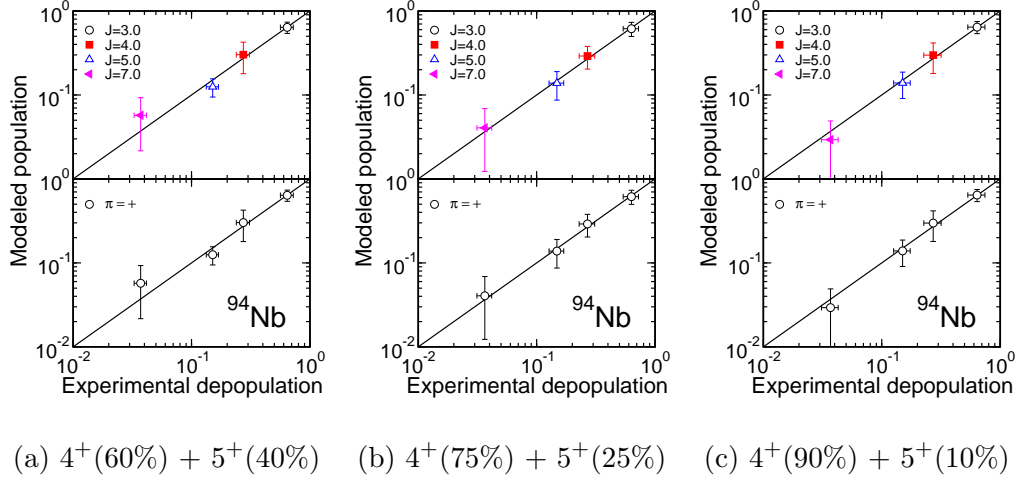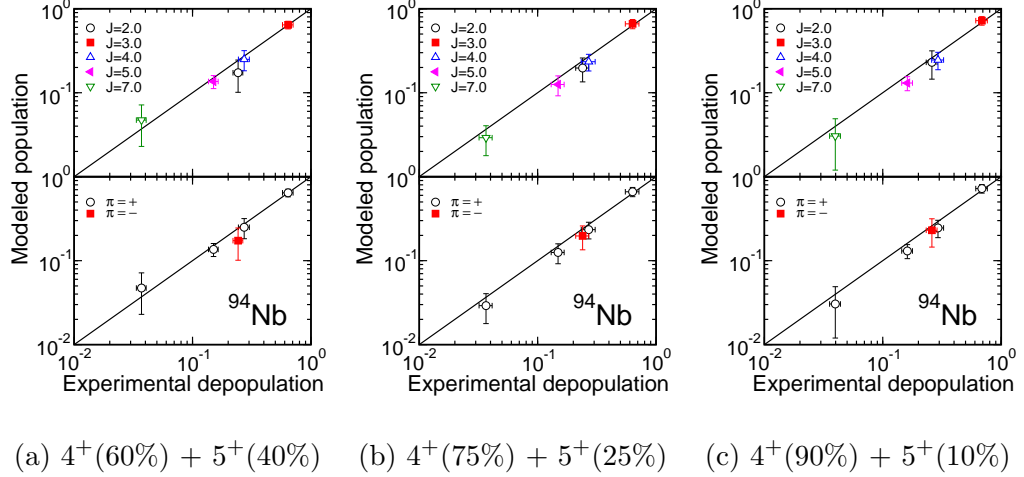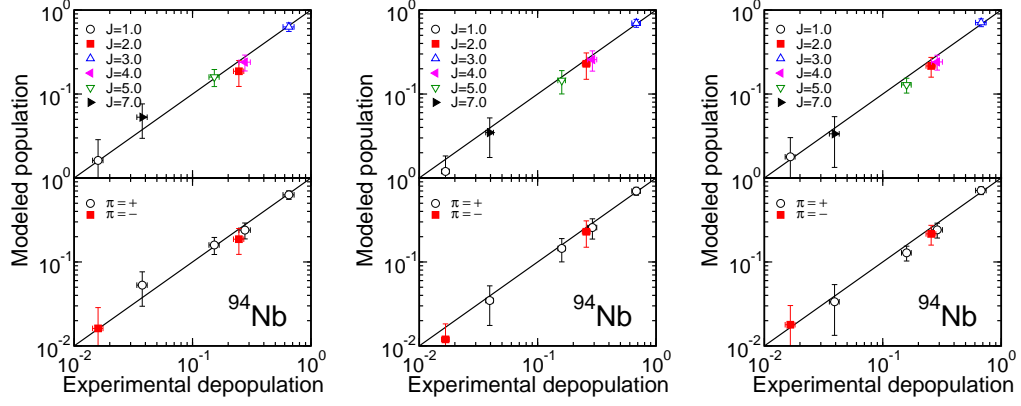
Figure 4.28: Population-depopulation plots for various capture-state spin distributions with $E_{crit} = 311.8$ keV and the $J^\pi = 4^+$ and 5^+ for the 311.8-keV level.

334.1-keV Level

This level has 293.2-keV γ-rays feeding the 3^+ 40.9-keV level with $M1$ multipolarity [6]. J^π was tentatively assigned as $(3)^+$ based on Hauser-Feshbach calculations in (p,nγ) data [36]. However, the aforementioned theoretical calculations predict it be a 2^+ state in the ground state multiplet [30][31]. Population-depopulation plots shown in Figure 4.29 support both possibilities, but the assignment $J^\pi = (2)^+$ was made based on the shell model predictions.

(a) $J^\pi = 2^+$
$4^+(60\%) + 5^+(40\%)$

(b) $J^\pi = 2^+$
$4^+(75\%) + 5^+(25\%)$

(c) $J^\pi = 2^+$
$4^+(90\%) + 5^+(10\%)$

(d) $J^\pi = 3^+$
$4^+(60\%) + 5^+(40\%)$

(e) $J^\pi = 3^+$
$4^+(75\%) + 5^+(25\%)$

(f) $J^\pi = 3^+$
$4^+(90\%) + 5^+(10\%)$
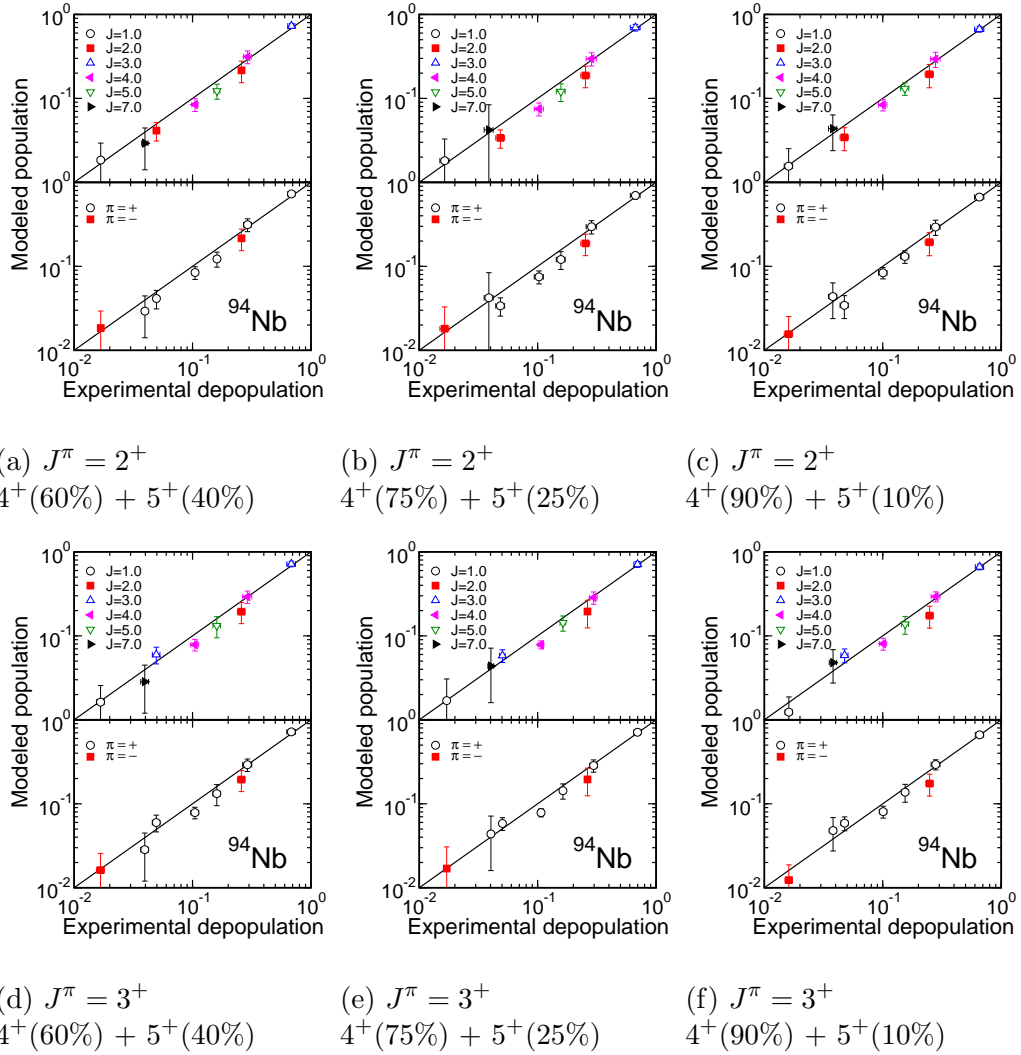
Figure 4.29: Population-depopulation plots for various capture-state spin distributions with $E_{crit} = 334.1$ keV and $J^\pi = 4^+$ and 5^+ for the 334.1-keV level.

396.2-keV Level

This level is negative parity with tentatively-assigned $J^\pi = (3)^-$ with $E1$ γ-rays to feeding the 4^+ level at 58.7 keV and mixed $M1 + E2$ γ-rays feeding the 2^- level at 140.3 keV. Additionally, intense primary γ-rays feed this level. The ENSDF J^π assignment for this level is $(3)^-$ [6], which is supported by consistency in the population-depopulation plots shown in Figure 4.30.

(a) $4^+(60\%) + 5^+(40\%)$ (b) $4^+(75\%) + 5^+(25\%)$ (c) $4^+(90\%) + 5^+(10\%)$
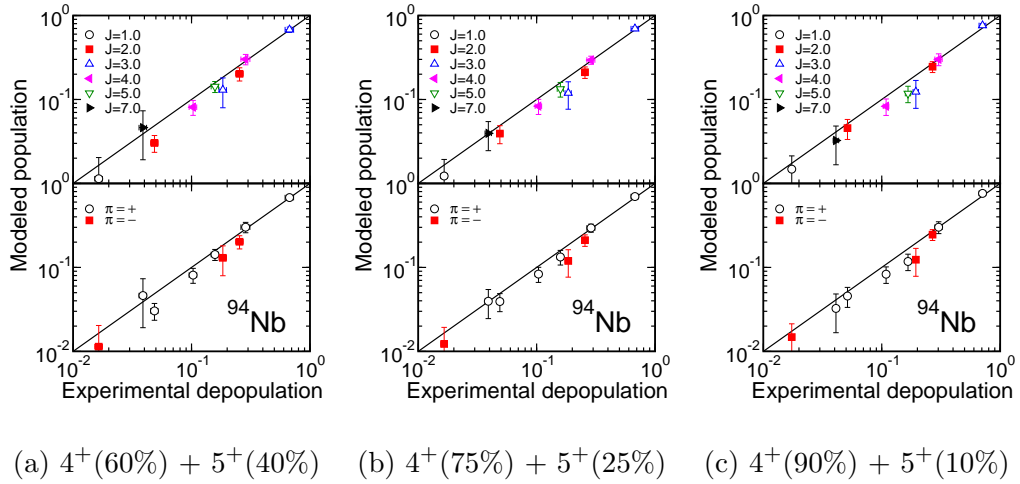
Figure 4.30: Population-depopulation plots for various capture-state spin distributions with $E_{crit} = 396.2$ keV.

450.2-keV Level

The ENSDF J^π assignment for this level was $(3)^-$, where the spin $J = 3$ was made on the basis of Hauser-Feshbach calculations in $(p,n\gamma)$ data [35][36] that suggested $J^\pi = 3^+$. Support for the negative-parity assignment comes from an $M1$ transition to the 140.3-keV level with $J^\pi = (2)^-$ [6]. Bogdanovic et al [31] suggested $J^\pi = 3^{(-)}$ with a tentative parity assignment. The population-depopulation plots, shown in Figure

4.31 with $J^\pi = 2^-, 3^-$, and 3^+ suggest that the best agreement is with $J^\pi = 3^+$. The modeled population is significantly lower and significantly higher than experimental depopulation for the $J^\pi = 2^-$ and 3^-, respectively. Although $J^\pi = 3^+$ produced the best consistency in population-depopulation, the parity assignment is at odds with the $M1$ multipolarity of the 309.9-keV transition. However, $J^\pi = 2^-$ was chosen because it seems consistent with the other negative-parity levels that are under-populated in the statistical model simulations. An observation worth noting is seen in Figure 4.31 in the case when $J^\pi = 3^-$; the presence of another 3^- state affects the other 3^- state at 396.2 keV by decreasing its modeled population. This is an example of the interdependence of the level scheme the statistical model simulations.

631.5-keV Level

The ENSDF J^π assignment for this level is $(4)^+$. Most of the intensity $(> 80\%)$ depopulates this level with the 518.1-keV γ-ray with $M1$ multipolarity to the 113.4-keV level with $J^\pi = 5^+$ [6]. Thus, this level could be $J^\pi = 4^+, 5^+$ or 6^+. For analysis of this level and the following levels, the J^π_{CS} is assumed $4^+(75\%) + 5^+(25\%)$. The population-depopulation plots for $J^\pi = 4^+$ and 5^+ are shown in Figure 4.32. Better agreement was found for $J^\pi = 4^+$.

(a) $J^\pi = 2^-$ (b) $J^\pi = 2^-$ (c) $J^\pi = 2^-$

(d) $J^\pi = 3^-$ (e) $J^\pi = 3^-$ (f) $J^\pi = 3^-$

(g) $J^\pi = 3^+$ (h) $J^\pi = 3^+$ (i) $J^\pi = 3^+$
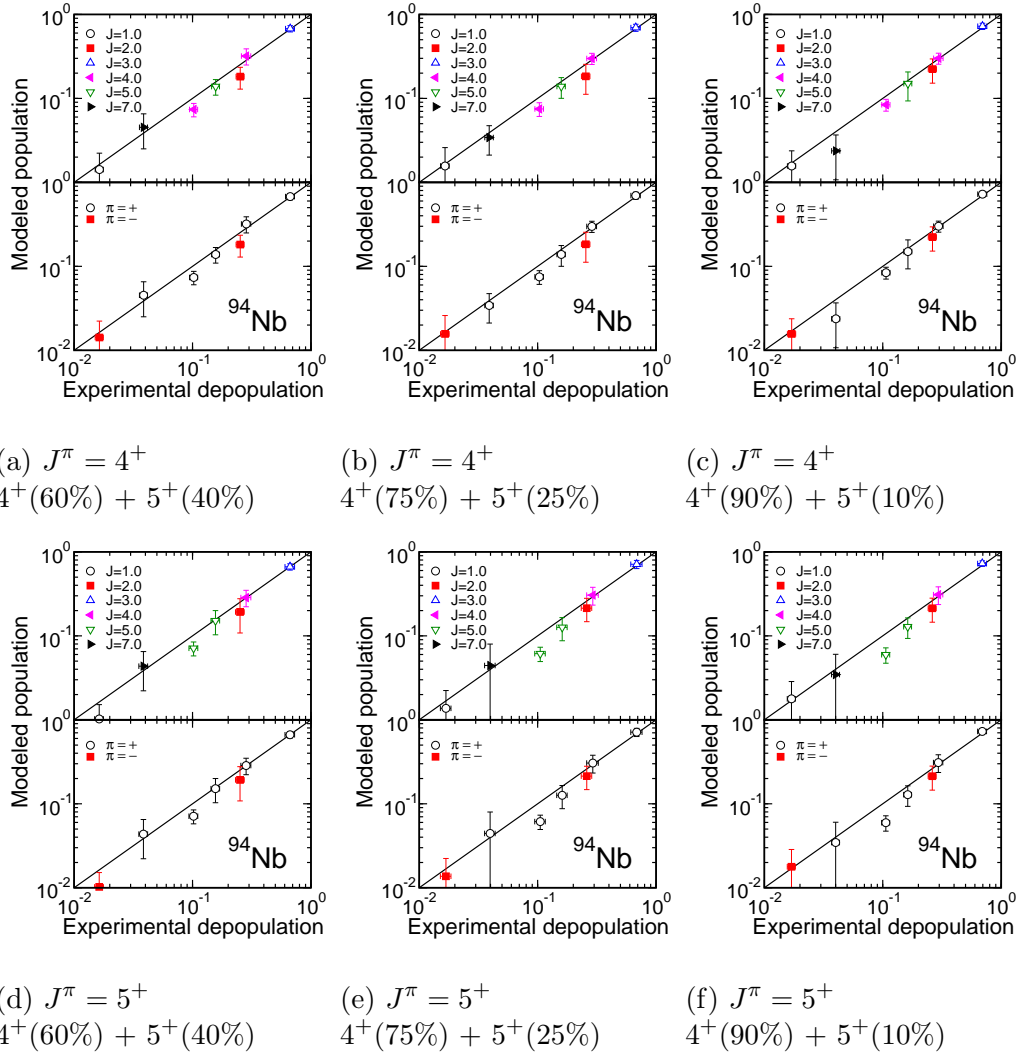$4^+(60\%) + 5^+(40\%)$ $4^+(75\%) + 5^+(25\%)$ $4^+(90\%) + 5^+(10\%)$
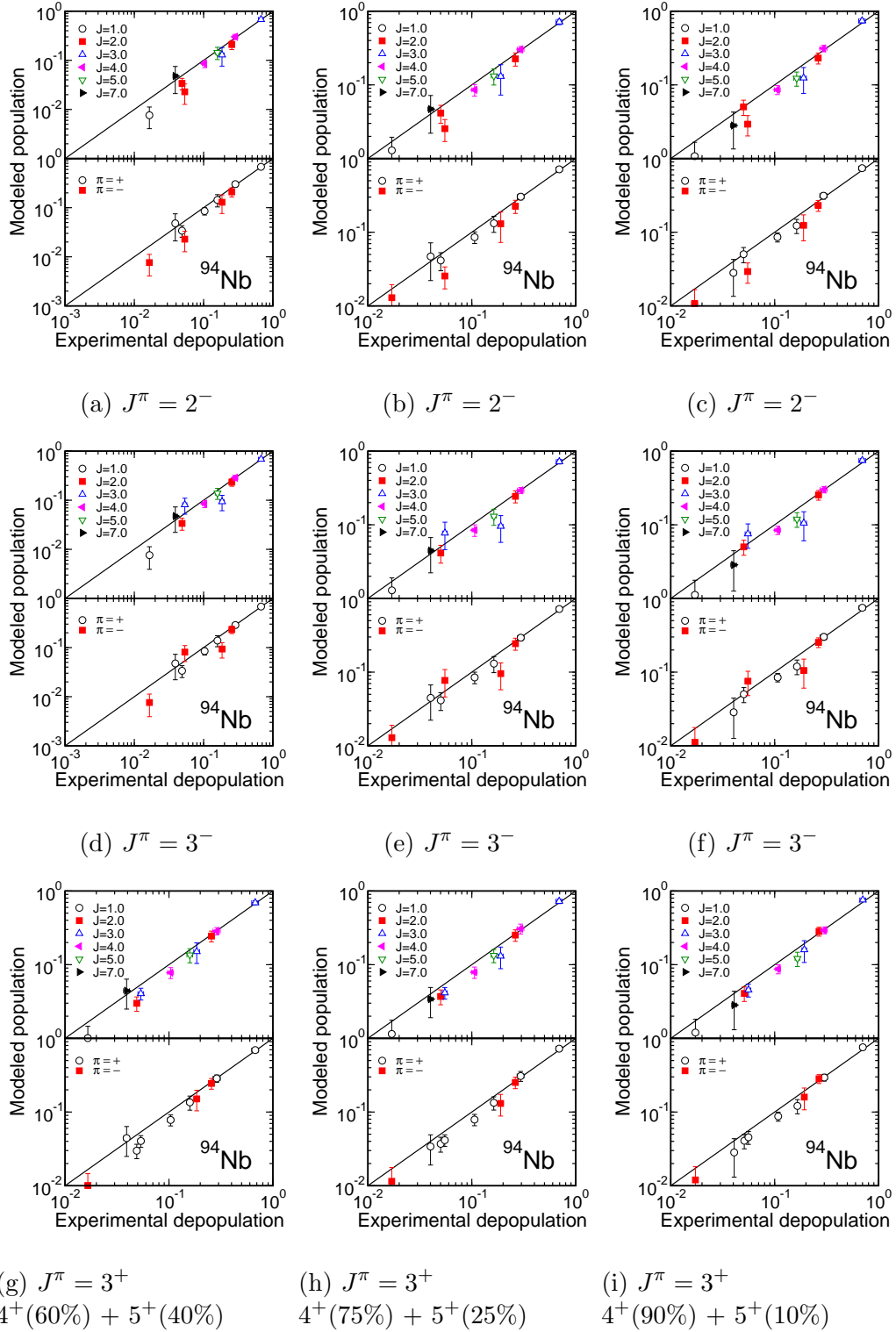
Figure 4.31: Depopulation-population plots for various capture-state spin distributions with $E_{crit} = 450.2$ keV and the $J^\pi = 2^-$, 3^- and 3^+ for the 450.2-keV level.

94

(a) $J^\pi = 4^+$ (b) $J^\pi = 5^+$

Figure 4.32: Population-depopulation plots for $E_{crit} = 631.5$ keV with $J^\pi = 4^+$ and 5^+ for the 631.5-keV level and assuming $J^\pi_{CS} = 4^+(75\%) + 5^+(25\%)$.

(a) $J^\pi = 5^+$
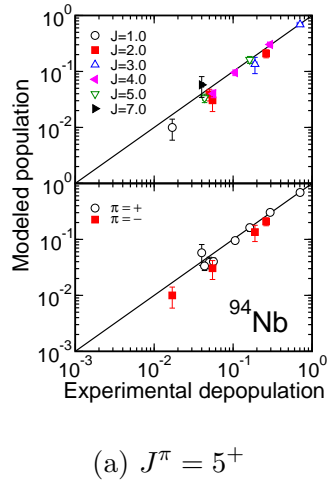
Figure 4.33: Population-depopulation plots for $E_{crit} = 641.0$ keV with 5^+ for the 641.0-keV level and assuming $J^\pi_{CS} = 4^+(75\%) + 5^+(25\%)$.

641.0-keV Level

The ENSDF J^π assignment for this level is $(5)^+$. Feeding from a 4^- resonance limits the possibilities of J^π to $3^+, 4^+$ or 5^+. Considering that this level feeds the ground state, 78.7-, 113.4- and 311.8-keV levels with $J^\pi = 6^+$, 7^+, 5^+ and 4^+, the likeliest J^π is 5^+. This was supported by the population-depopulation consistency as shown in Figure 4.33

666.1-keV Level

The ENSDF J^π assignment for this level is $(3)^+$ based on the placement of the 525.77-keV γ-ray with $E1$ multipolarity depopulating this level to the 140.3-keV level with $J^\pi = 2^-$ [6] and the Hauser-Feshbach calculations [36]. Based on selection rules, this level can have $J^\pi = (1, 2, 3)^+$. The lack of primary γ-ray feeding to this level also supports $J^\pi < 2$. Two γ-rays depopulating this level in ENSDF were removed: the 364.4- and 552.8-keV γ-rays. The 364.4-keV γ-ray was not observed in this work nor in the work of Bogdanovic et al [31].The 552.8-keV γ-ray was multiply placed as depopulating the 631.5-keV level also; on the basis of selection rules, the transition probably depopulates the 631.5-keV level, which would be $J^\pi = (4)^+ \to 5^+$. Additional γ-rays were unable to be placed in this level. With weak depopulation of this level, population-depopulation plots shown in Figure 4.34 indicate that $J^\pi = 1^+$ is more consistent.
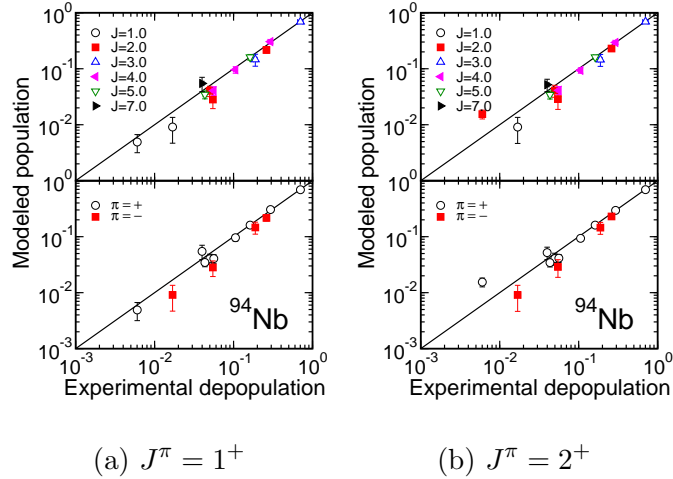
Figure 4.34: Population-depopulation plots for $E_{crit} = 666.1$ keV with $J^\pi = 1^+$ and 2^+ for the 666.1-keV level and assuming $J^\pi_{CS} = 4^+(75\%) + 5^+(25\%)$.

785.7-keV Level

The ENSDF J^π assignment for this level is $(3)^+$ based on the placement of the 484.3-keV γ-ray with $E1$ multipolarity depopulating this level to the 301.6-keV level with $J^\pi = 2^-$ [6] and the Hauser-Feshbach calculations [36]. DICEBOX results indicated that $J^\pi = 1^-$ was more consistent for the 301.6-keV level. As seen in Figure 4.35, $J^\pi = 2^+$ shows good agreement in population-depopulation for this level and is consistent with the $E1$ transition feeding the 1^- level.
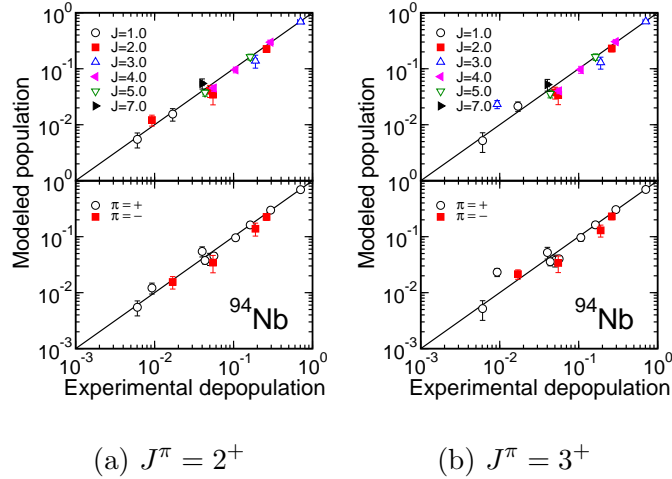
Figure 4.35: Population-depopulation plots for $E_{crit} = 785.7$ keV with $J^\pi = 1^+$ and 2^+ for the 785.7-keV level and assuming $J^\pi_{CS} = 4^+(75\%) + 5^+(25\%)$.

792.6-keV Level

The ENSDF J^π assignment for this level is $(3,4)^+$ based on the placement of the 458.5-keV γ-ray with $M1$ multipolarity depopulating this level to the 334.1-keV level with $J^\pi = (3)^+$ [6] and the Hauser-Feshbach calculations [36]. DICEBOX results indicated that both $J^\pi = 2^+$ and 3^+ were consistent for the 334.1-keV level, with $J^\pi = 2^+$ selected due to shell model predictions. Although $J^\pi = 4^+$ had better agreement as seen in Figure 4.36, 3^+ is consistent with the $M1$ transition feeding the 2^+ level.
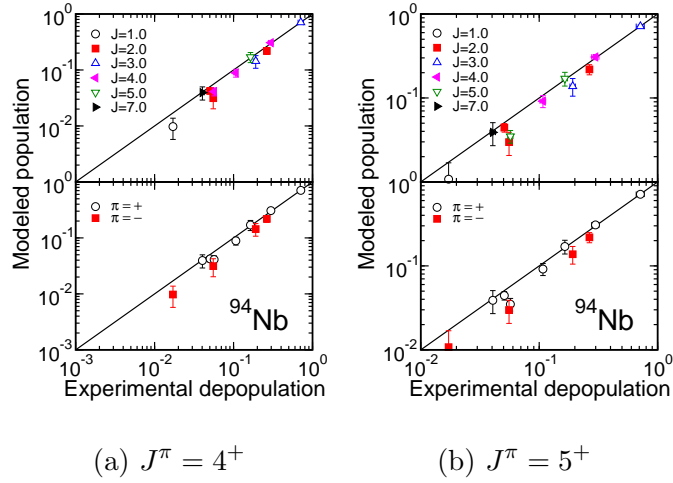
(a) $J^\pi = 3^+$　　　　　　(b) $J^\pi = 4^+$
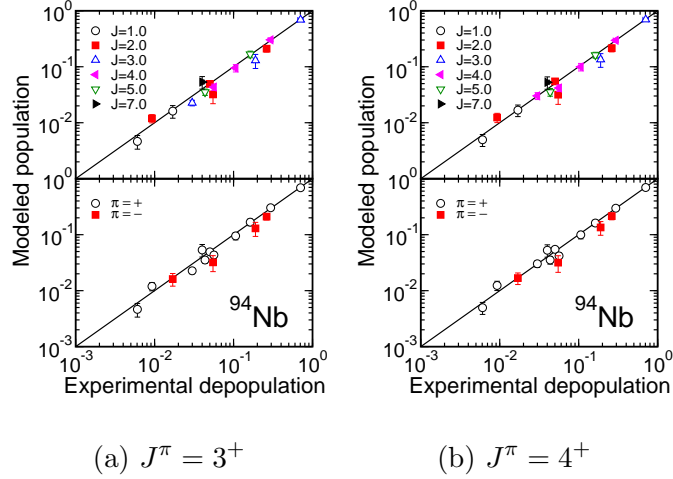
Figure 4.36: Population-depopulation plots for $E_{crit} = 792.6$ keV with $J^\pi = 1^+$ and 2^+ for the 792.6-keV level and assuming $J^\pi_{CS} = 4^+(75\%) + 5^+(25\%)$.

816.8-keV Level

This level is negative parity based on the $E1$ transition with $E_\gamma = 482.6$ keV to the positive-parity level at 334.1 keV with $J^\pi = 2^+$ [6]. Hauser-Feshbach calculations suggested that $J^\pi = 3^-$ [35][36]. The ENSDF J^π assignment for this level is $(3)^+$ based [6] and the Hauser-Feshbach calculations [35][36]. This level is fed by primary γ-rays that must be $E1$ transitions and has an $E1$ transition to 2^+, thus limiting the possibilities to $J^\pi = 3^-$. However, population-depopulation plot shown in Figure 4.37 suggest that there is missing intensity depopulating this level if $J^\pi = 3^-$. This level is fed by 150.7-keV γ-rays from the 816.8-keV level with $J^\pi = 3^-$; the multipolarity of this transition depends on the J^π of ths 666.1-keV level. The transition is likely $E1$ if this level is 2^+ with $\alpha = 0.036$ and or $M2$ if this level is 1^+ with $\alpha = 0.549$. The 816.8-keV level is missing intensity depopulating the level, supporting the higher ICC as discussed later, the $J^\pi = 1^+$ was still supported with $E_{crit} = 816.8$ keV.
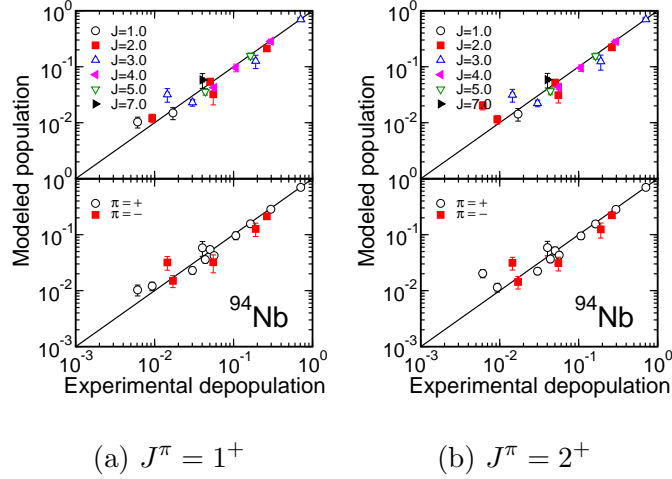
Figure 4.37: Population-depopulation plots for $E_{crit} = 816.8$ keV with $J^{\pi} = 1^{+}$ and 2^{+} for the 666.1-keV level (see text for explanation) and assuming $J^{\pi}_{CS} = 4^{+}(75\%) + 5^{+}(25\%)$.

Summary

The summary of ^{94}Nb nuclear structure information for the 16 levels up to the 816.8-keV level is shown in Table 4.10. The statistical-model calculations using DICEBOX suggest changes to the spin assignments of 7 of these 16 level from the current ENSDF assignment. The 301.6-keV level was proposed to be $J^{\pi} = 1^{-}$ and to form a doublet with the 140.3-keV level with $J^{\pi} = 2^{-}$. The next two positive-parity levels at 311.8 and 334.1 keV are proposed to be 4^{+} and 2^{+}. The DICEBOX results suggest that $J^{\pi} = 3^{+}$ for the 450-keV level, but the negative parity was not overturned because of the $M1$ transition to a negative-parity state. Because negative parity does not provide consistent population-depopulation, the recommended E_{crit} from this work is 396 keV.

100

Table 4.10: Comparison of J^π assignments

E_{level}	Ref [30] (1968)	Ref [32] (1971)	Ref [32][36] (1976, 1977)	Ref [31] (1985)	Ref [6] (2006)	This work
0.0	6^+	6^+	6^+	6^+	6^+	6^+
40.9	3^+	3^+	3^+	3^+	3^+	3^+
58.7	4^+	$(4)^+$	4^+	4^+	$(4)^+$	4^+
78.7	7^+	$(7)^+$	7^+	7^+	$(7)^+$	7^+
113.4	5^+	5^+	5^+	5^+	$(5)^+$	5^+
140.3	2^-	(2^-)	$2^{(-)}$	2^-	$(2)^-$	2^-
301.6	–	(2^-)	$2^{(-)}$	2^-	$(2)^-$	1^-
311.8	5^+	$(5)^+$	$(5)^+$	$(4,5)^+$	$(4,5)^+$	4^+
334.1	2^+	$(3)^+$	3^+	$(2,3)^+$	$(3)^+$	2^+
396.2	–	(4^-)	3^-	3^-	$(3)^-$	3^-
450.2	–	(3^+)	(3^+)	$3^{(-)}$	$(3)^-$	(2^-)
631.5	4^+	$(4)^+$	$(4)^+$	$(4,5)^+$	$(4)^+$	$(4)^+$
641.0	6^+	$(6)^+$	$(6)^+$	$(5,6^+$	$(5)^+$	$(5)^+$
666.1	–	$(\leq 4)^+$	(3^+)	$2^-, (3^-)$	$(3)^+$	$(1)^+$
785.7	–	$(\leq 4)^+$	$3^{(+)}$	$(3^+, 4^-)$	$(3)^+$	$(2)^+$
792.6	3^+	$(3)^+$	3^+	$(3,4)^+$	$(3,4)^+$	$(3)^+$
816.8	(3^+)	(3^+)	3^+	$(3,4)^+$	$(3)^-$	$(3)^-$

4.2.4 Determining σ_m

The 40.9 keV γ-ray, below the low-energy threshold in our measurement, is difficult to experimentally observe because the M3 transition of this level is dominated by internal conversion with an ICC of 1323(19) calculated with BrIcc. The ENSDF intensity (per 100 neutron captures) for this γ-ray is 0.045(10) [31]. As with other γ-ray transitions not observed in this work or interfered with by background, the ENSDF intensity was normalized to a σ_γ of 0.00050(11) b using the 255.9-keV standardization peak. This σ_γ, combined with the ICC as $\sigma_\gamma(1 + \alpha)$, represents the decay to the ground state with the 0.995(6) branching ratio [79]. The metastable state also beta decays to ^{94}Mo, as shown in Figure 4.38, with a branching ratio of 0.0050(6). The branching was insignificant relative to the uncertainty of the σ_γ and was, thus, neglected for this case.

The large uncertainty (22 percent) of this σ_γ resulted in a large uncertainty in the σ_0, 0.96(17) b, found in DICEBOX simulations with $E_{crit} = 396.2$ keV. Consequently, alternative methods were explored in estimating the σ_m, which includes decay to the [94]Nb ground state and to [94]Mo, for the 40.891-keV level.
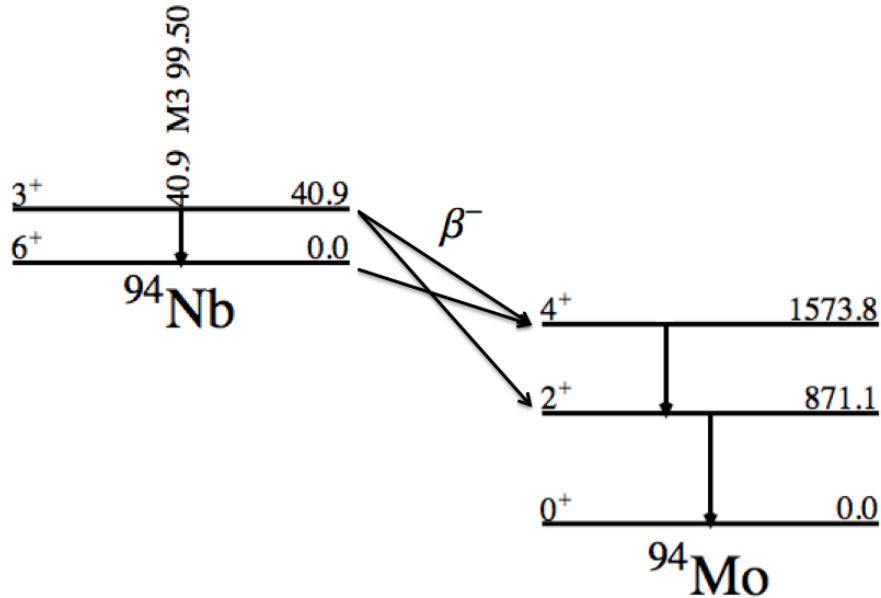
Figure 4.38: The decay scheme for the beta decay of [94m]Nb and [94]Nb.

The first estimate was found as the balance of known level feeding using the σ_γ data determined in this work. This level is fed by fourteen secondary γ-rays up to the 1332-keV level and one primary γ-ray. The intensities of these γ-rays are shown in Table 4.11 This approach is susceptible to γ-rays that are missing in the decay scheme, which could be the result of missing levels, and also γ-rays misplaced in the level scheme such that they feed the metastable state. Nonetheless, the major contributions are from the low-lying levels. The total feeding was 0.710(25) b, with 41% and 37%

of the contribution from the 17.98- and 99.4-keV transitions, respectively. The 17.98-keV γ-ray intensity was adopted from ENSDF data measured by Bogdanovic et al. [31]. Despite being very thin (0.05 mm), an important consideration is whether this intensity was corrected for γ-ray self-absorption. The mass attenuation coefficients for the 17.98-, 40.9- and 99.4-keV γ-rays in niobium metal are 15.16, 11.10 and 0.9767 (cm^2/g), respectively. Assuming the effective sample thickness for the purpose of γ-ray self-absorption correction is half the sample thickness (0.025 mm), these γ-rays are self-absorbed in the sample 23%, 18% and 2%, respectively. After correcting for γ-ray self-absorption, the sum of transitions feeding the metastable state yields 0.799(31) b and the 40.9-keV transition has an intensity of 0.80(18). The corresponding σ_γ values, calculated from $\sigma_m = \sigma_\gamma^{exp}(1 + \alpha)$, were 0.00060(3) and 0.00061(14) b, respectively. The similarity of these values supports the case that the low-energy γ-rays should be corrected for γ-ray self absorption.

The second approach used DICEBOX simulations to estimate continuum feeding of the metastable state. The total feeding, (σ_m), was calculated as the sum of the experimentally-observed feeding up to E_{crit} corrected for the simulated feeding from the continuum above E_{crit} as

$$\sigma_m = \sum \sigma_\gamma^{exp}(1 + \alpha) + \sum \sigma_\gamma^{sim} = \frac{\sum \sigma_\gamma^{exp}(1 + \alpha)}{1 - P_L}, \tag{4.2}$$

where P_L is the probability that the metastable state is fed directly from the continuum. Both the uncorrected and corrected 17.98-keV γ-ray intensities were considered. Fig. 4.39 shows the variation of σ_m, the experimentally-observed cross section up to E_{crit} (σ^{exp}), and cross section from continuum feeding above E_{crit} (σ^{sim}) up to $E_{crit} = 450$ keV for both cases. The values for σ_m with $E_{crit} = 396.2$ keV for the uncorrected and corrected cases were 0.718(27) and 0.830(54) b, respectively. The corresponding σ_γ values were 0.00054(2) and 0.00063(4) b, which includes the small-branching contribution of the beta decay.

Table 4.11: Transitions feeding the metastable state.

E_L [keV] [6]	E_γ [keV]	σ_γ b	α	$\sigma_\gamma(1 + \alpha)$
58.71	17.98(7)	0.0566(27)[a] [b]	4.18(8)	0.293(15)[c]
140.30	99.31(2)	0.2323(32)	0.1219(17)	0.261(5)
334.10	293.16(2)	0.0490(7)	0.0129(2)	0.050(1)
396.23	355.26(9)	0.00442(14)		0.0044(3)
450.20	409.13(7)	0.00250(9)		0.0025(2)
631.53	590.60(2)	0.00637(11)		0.0064(3)
792.60	751.57(3)	0.00980(21)		0.0098(2)
816.83	775.64(7)	0.0109(13)		0.0109(13)
924.25	883.74(2)	0.01418(23)		0.0142(2)
1023.35	982.39(3)	0.00111(34)		0.0011(3)
1158.71	1117.94(10)	0.00908(16)		0.0091(2)
1169.88	1128.92(3)	0.01257(20)		0.0126(2)
1247.26	1206.57(2)	0.01776(27)		0.0178(3)
1332.60	1291.44(3)	0.00683(23)		0.0068(2)
7227.54	7186.30(3)	0.00724(34)		0.0072(3)
			Total:	**0.710(25)[d]**

[a] Adopted from ENSDF data [6][31].
[b] 0.0738(51) b when corrected for γ-ray self-absorption.
[c] 0.382(21) b when corrected for γ-ray self-absorption.
[d] 0.799(31) b when corrected for γ-ray self-absorption.

The third approach for estimating σ_m was balancing the modeled population and experimental depopulation of the metastable state in DICEBOX simulations. The previously-calculated σ_γ values for the 40.9-keV γ-ray were used in DICEBOX simulations with 50 nuclear realizations of 50,000 cascade events. Additionally, the two possibilities for the σ_γ of the 17.98-keV transition were 0.0566(27) and 0.0738(51) b were considered. In all cases, the modeled populations of the metastable state and 58.7-keV level were 0.719(51) and 0.298(35), respectively. The difference of the modeled population and experimental depopulation, $P_L^{sim} - P_L^{exp}$, for the different combinations of σ_γ are presented in Table 4.12. These values show consistency for Cases 1-6 when both σ_γ are either uncorrected or corrected. However, Case 7, with
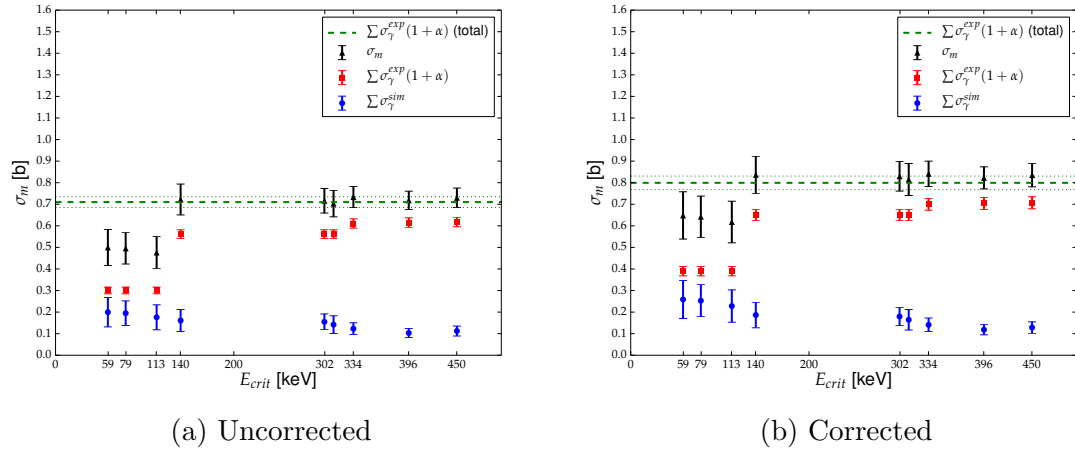
Figure 4.39: Total feeding of the 40.891-keV level (σ_m) with increasing E_{crit} for the cases when the 17.98-keV intensity is uncorrected and corrected for γ-ray self-absorption.

the corrected σ_γ for the 40.9-keV transition and uncorrected σ_γ for the 17.98-keV transition, showed a disagreement for the 48.7-keV level, as seen in Figure 4.40. Case 6 had excellent agreement in population-depopulation for the two low-lying levels and was adopted going forward.

Table 4.12: Balance of modeled population and experimental depopulation for the 40.9- and 58.7-keV levels.

Case	σ_γ (b) 40.9 keV	σ_γ (b) 17.98 keV	$P_L^{sim} - P_L^{exp}$ $E_L = 40.9$ keV	$P_L^{sim} - P_L^{exp}$ $E_L = 58.7$ keV
1	0.00050(11)	0.0566(27)	0.019 ± 0.206	0.005 ± 0.066
2	0.00052(2)	0.0566(27)	0.027 ± 0.073	0.014 ± 0.045
3	0.00054(2)	0.0566(27)	0.021 ± 0.073	1.025 ± 0.065
4	0.00061(14)	0.0738(51)	0.443 ± 0.058	-0.038 ± 0.077
5	0.00060(3)	0.0738(51)	0.007 ± 0.080	-0.045 ± 0.049
6	0.00063(4)	0.0738(51)	0.000 ± 0.088	-0.031 ± 0.049
7	0.00063(4)	0.0566(27)	0.000 ± 0.088	0.045 ± 0.042
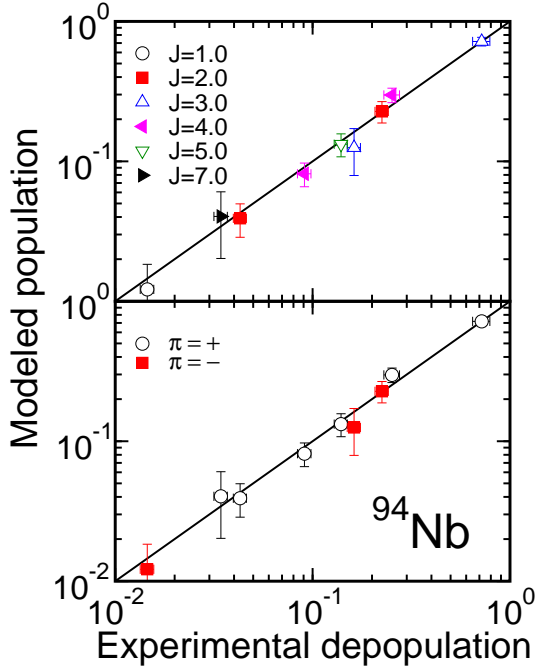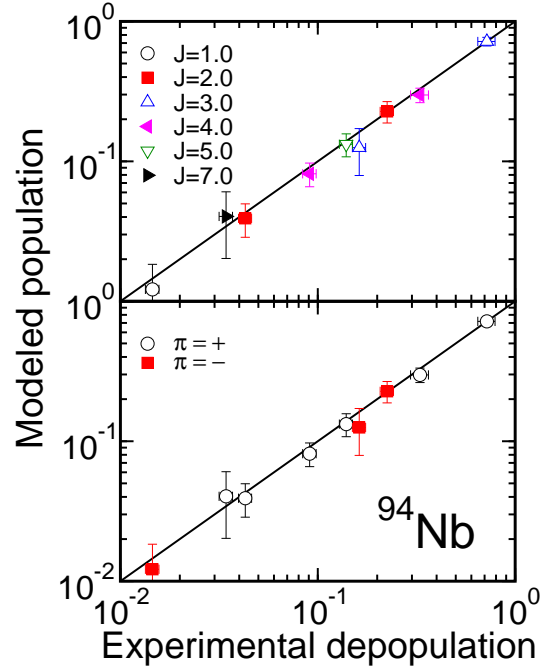
(a) Case 6   (b) Case 7

Figure 4.40: Population-depopulation plots with the σ_γ for the 40.9-keV transition 0.00062(3) b and when the σ_γ of the 17.98-keV transition is (a) 0.0738(51) and (b) 0.0566(27)

The fourth approach for estimating σ_m used the intensity of the 871.1-keV γ-ray, which is emitted in each ^{94m}Nb beta decay as seen in Figure 4.38. The beta-decay branching ratio is 0.0050(6) [79]. The ^{94}Nb ground state also beta decays to excited-states in ^{94}Mo, but the long half-life of 20,300 years makes this contribution negligible. With an irradiation time (1436 minutes) of greater than 100 half-lives ($T_{1/2} = 6.26$ minutes) of the meta-stable state, the contribution from un-decayed ^{94m}Nb atoms was insignificant, but was accounted for by correcting the 871.1-keV peak area, A_γ, with the in-beam saturation factor

$$B = 1 - \frac{1 - e^{-\lambda t}}{\lambda t},$$ (4.3)

where λ is the decay constant and t is the irradiation time [80]. With $B = 0.994$, the 871.1-keV peak, shown in Figure 4.41, had a 0.00508(14) b σ_γ. Using the branching ratio, the resulting σ_m was 1.02(12) b. This was considerably higher than previous estimates and almost as high as σ_0. The discrepancy was attributed to the imprecise branching ratio. A new branching ratio, calculated as the ratio of the 871.1-keV σ_γ to $\sigma_m = 0.830(54)$ b, was 0.0061(4). This more precise value was within the uncertainty of the ENSDF data.
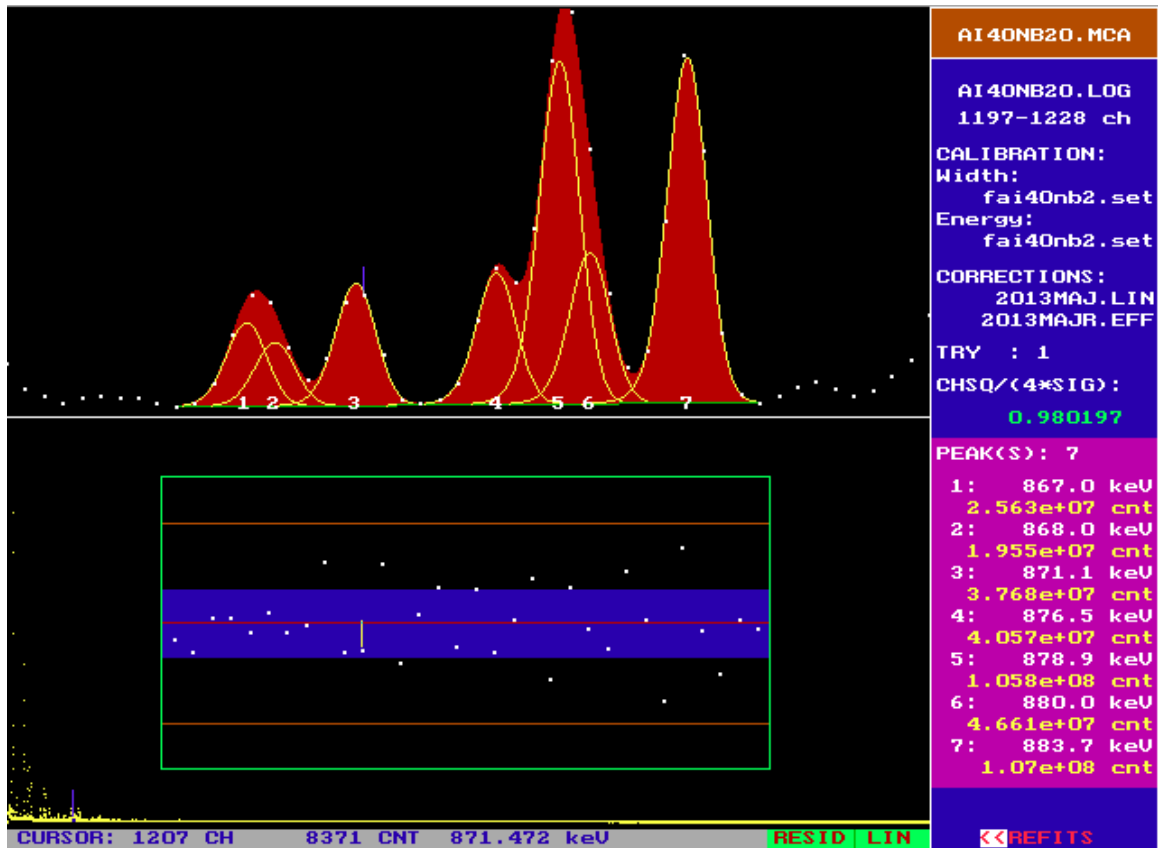
Figure 4.41: The 871.1-keV γ-ray peak from ^{94}Mo in ^{94m}Nb beta decay.

In summary, the adopted σ_m was 0.830(54) b from the DICEBOX technique combining experimental feeding below E_{crit} and the simulated continuum feeding from above E_{crit}. This value hinged on the assumption that the ENSDF intensity of the 17.98-keV γ-ray needed to be corrected for γ-ray self-absorption. It was supported by 40.9-keV σ_γ corrected for γ-ray self-absorption, which leads to $\sigma_m = 0.81(18)$ b using the branching ratio 0.0061(4) calculated in this work. The updated decay scheme is displayed in Table 4.13.

Table 4.13: Experimental γ-ray cross sections, corresponding to both primary and secondary γ-ray transitions, measured in this work up to the 816-keV level. Quantities in brackets represent tentative assignments. Multipolarities, XL, in square brackets were assumed based on selection rules; other values were taken from ENSDF unless otherwise noted.

E_L [keV] [6]	J^π	E_γ [keV]	σ_γ	α	ML
0.0	$6+$				
40.891(12)	3^+	40.90(5)	$0.00063(4)^a$	1323(19)	M3
58.708(10)	4^+	17.98(7)	$0.0738(51)^b$	4.18(6)	M1
78.6683(8)	7^+	78.562(11)	0.0276(9)	0.443(7)	M1
113.4009(8)	5^+	54.706(13)	$0.0074(3)^b$	2.05(7)	M1+E2
		113.306(9)	0.1218(40)	0.1597(23)	M1
140.298(12)	2^-	99.306(10)	0.2323(72)	0.1219(17)	E1
301.558(12)	$1^{-\dagger}$	161.145(10)	0.0157(5)	0.0741(23)	M1+E2
311.821(10)	$4^{+\dagger}$	253.062(7)	0.1025(32)	0.030(12)	M1,E2
334.102(12)	$2^{+\dagger}$	194.61(16)	0.00020(4)	0.01752(25)	[E1]
		293.157(8)	0.0490(15)	0.0129(2)	M1
396.227(12)	3^-	255.881(8)	0.1377(42)	0.0212(3)	M1+E2
		337.444(11)	0.0431(14)	0.00377(6)	E1
		355.256(74)	0.00442(24)	0.00329(5)	[E1]
450.204(14)	$(2)^{-\dagger}$	148.69(11)	0.00009(4)	0.0761(11)	[M1]
		309.854(14)	0.0532(16)	0.01126(16)	M1
		409.130(72)	0.00071(10)	0.00228(4)	[E1]
631.533(13)	$(4)^+$	319.603(32)	0.00250(12)	0.01042(15)	[M1]
		518.124(13)	0.0438(14)	0.00323(5)	M1
		552.811(56)	0.0010(1)		
		572.696(37)	0.00160(9)	0.00255(4)	[M1]
		590.600(17)	0.00637(21)	0.00238(4)	[M1]
640.988(10)	$(5)^+$	329.135(10)	0.00841(28)	0.00969(14)	[M1]
		527.609(16)	0.00929(32)	0.00310(5)	[M1]
		562.245(15)	0.02183(69)	0.00317(5)	[E2]
		641.0(33)	0.00356(13)	0.00197(3)	[M1]
666.11(3)	$(1)^{+\dagger}$	525.751(21)	0.00601(21)	0.001229(18)	E1
		552.811(56)	0.00098(9)		
785.657(25)	$(2)^{+\dagger}$	484.349(22)	0.00545(19)	0.001498(21)	E1
		645.053(32)	0.00189(10)	0.00077(1)	[E1]
		672.273(48)	0.00183(15)		
792.595(16)	$(3)^{+\dagger}$	396.257(58)	0.00080(10)	0.00432(6)	[E1]
		458.473(24)	0.01808(60)	0.001450(21)	M1
		734.2(4)	0.0010(1)	0.001375(20)	[M1]

Continued on next page

Table 4.13 – *Continued from previous page*

E_L [keV] [6]	J^π [6]	E_γ [keV]	σ_γ	α	XL
		751.568(34)	0.00980(35)	0.0363(5)	[M1]
816.83(3)	$(3)^-$	150.497(14)	0.00168(6)	0.00382(6)	[E1]
		482.561(69)	0.00168(9)	0.000514(8)	E1
		775.638(69)	0.0109(15)		[E1]
7227.54(8)	$4^+,5^+$	6331.70(18)	0.00210(9)		[E1]
		6410.78(29)	0.00046(5)		[E1]
		6434.63(18)	0.00275(26)		[M1]
		6585.80(48)	0.00017(5)		[M1]
		6595.67(20)	0.00159(8)		[M1]
		6830.98(18)	0.01258(23)		[E1]
		6892.60(29)	0.00041(6)		[E2]
		6915.38(19)	0.00245(30)		[M1]
		7113.63(28)	0.00091(9)		[M1]
		7168.42(24)	0.00113(8)		[M1]
		7186.30(19)	0.00724(34)		[M1]
		7227.31(28)	0.00034(4)		[M1]

[a] Determined in this work from experimental and continuum feeding.
[b] Adopted from normalized ENSDF values corrected for γ-ray self-absorption.
[†] Assignment made on the basis of statistical model calculations with DICEBOX.

4.2.5   Determining σ_0

The total radiative thermal-neutron capture cross section, σ_0, was calculated as

$$\sigma_0 = \sum \sigma^{exp}(1+\alpha) + \sum \sigma_\gamma^{sim}, \tag{4.4}$$

where $\sum \sigma_\gamma^{exp}(1+\alpha)$ is the total cross section of transitions feeding the ground state from levels below E_{crit} and $\sum \sigma_\gamma^{sim}$ is the contribution of ground state feeding from the continuum. The $\sum \sigma_\gamma^{sim}$ is found from the experimentally-determined feeding of the ground state below E_{crit} corrected for the probability, $P(GS)$, that the ground state is directly populated from levels above E_{crit}:

$$\sum \sigma_\gamma^{sim} = \sum \sigma_\gamma^{exp}(1+\alpha)\frac{P(GS)}{1-P(GS)}. \tag{4.5}$$

Table 4.14: Transitions feeding the ground state.

E_γ [keV]	σ_γ b	α	$\sigma_\gamma\,(1+\alpha)$
40.90(5)	0.00063(4)[a]	1323(19)	0.830(54)
78.56(20)	0.02762(41)	0.443(7)	0.0399(9)
113.31(19)	0.1218 (16)	0.1597(23)	0.1413(28)
640.95(32)	0.00356(8)		0.00356(8)
932.94(56)	0.00176(11)		0.00176(11)
957.31(28)	0.01774(28)		0.01774(28)
976.94(44)	0.00179(13)		0.00179(13)
1022.80(13)	0.00097(9)		0.00097(9)
1230.21(64)	0.00394(9)		0.00394(9)
1257.19(60)	0.00434(45)		0.00434(45)
1281.80(53)	0.00518(24)		0.00518(24)
1484.47(10)	0.00212(10)		0.00212(10)
7227.31(28)	0.00034(4)		0.00034(4)
		Total:	**1.053(60)**

DICEBOX simulations with 50 nuclear realizations and 100,000 cascade events were carried out with increasing E_{crit} up to 640 keV and assuming $J^\pi_{CS} = 4^+(75\%) + 5^+(25\%)$. Figure 4.42 shows the depopulation-population plots for increasing E_{crit} and assuming $J^\pi_{CS} = 4^+(75\%) + 5^+(25\%)$. Figure 4.43 shows the variation of the experimental ($\sum \sigma_\gamma^{exp}(1+\alpha)$) and continuum ($\sum \sigma_\gamma^{sim}$) feedings for these E_{crit}. In this figure, $\sum \sigma_\gamma^{exp}(1+\alpha)$ (*total*) is the sum of the transitions feeding the ground as shown in Table 4.14. The uncertainties of the ICCs were also propagated. $E_{crit} = 396.2$ keV was adopted as the highest level at which the decay scheme is complete and used to calculate the σ_0 determined in this work. The population-depopulation plot with $E_{crit} = 396$ keV is shown Figure 4.44. The sum of the experimental data for transitions feeding the ground state was (1.011 ± 0.056) b. σ_m contributed the majority (0.054 b) of the uncertainty. The fraction of direct feeding from the continuum above E_{crit} was $P(GS) = 0.1256 \pm 0.0042$. The contribution from continuum feeding, $\sum \sigma_\gamma^{sim}$, was (0.145 ± 0.049) b. These combine to give σ_0 as (1.156 ± 0.105) b.

These values are compared in Table 4.15 with those with $J_{CS}^{\pi} = 4^+(60\%) + 5^+(40\%)$ and $J_{CS}^{\pi} = 4^+(90\%) + 5^+(10\%)$. The effect of the capture-state spin distribution was found to be small relative to the uncertainties. Thus, the σ_0 determined in this work was (1.16 ± 0.11) b with $J_{CS}^{\pi} = 4^+(75\%) + 5^+(25\%)$. Though this value has a relatively large uncertainty, the mean agreed with the currently accepted literature value of (1.15 ± 0.05) b [28] and was statistically similar to the other measured values shown in Table 4.16.

Table 4.15: The effect of the capture-state spin distribution on σ_0.

J_{CS}^{π}	$P(GS)$	$\sum \sigma\gamma^{sim}$	σ_0
$4^+(60\%) + 5^+(40\%)$	0.1418 ± 0.0435	0.1671 ± 0.0521	1.178 ± 0.108
$4^+(75\%) + 5^+(25\%)$	0.1256 ± 0.0417	0.1452 ± 0.0489	1.156 ± 0.105
$4^+(90\%) + 5^+(10\%)$	0.1158 ± 0.0481	0.1324 ± 0.0555	1.143 ± 0.111

Table 4.16: Summary of ^{93}Nb(n,γ) σ_0 and σ_m measurements.

Reference	Ref	Method	σ_0	σ_m
Seren et al	[81] (1947)		1.0(4)	
Colmer et al	[82] (1950)	Pile oscillation	1.26(13)	
Tattersall et al	[83] (1960)	Pile oscillation	1.17(2)	
Druschel and Halperin	[84] (1968)		1.100(165)	
Schuman	[85] (1969)	Activation	1.0(1)	
RNAL	[2] (2000)	Evaluation	1.1589	0.79964
S.F. Mughaghab	[28] (2006)	Evaluation	1.15(5)	
This work		PGNAM	1.16(11)	0.83(5)

(a) $E_{crit} = 58.7$ keV (b) $E_{crit} = 78.7$ keV (c) $E_{crit} = 113.4$ keV

(d) $E_{crit} = 140.3$ keV (e) $E_{crit} = 301.6$ keV (f) $E_{crit} = 311.8$ keV

(g) $E_{crit} = 334.1$ keV (h) $E_{crit} = 396.2$ keV (i) $E_{crit} = 450.2$ keV
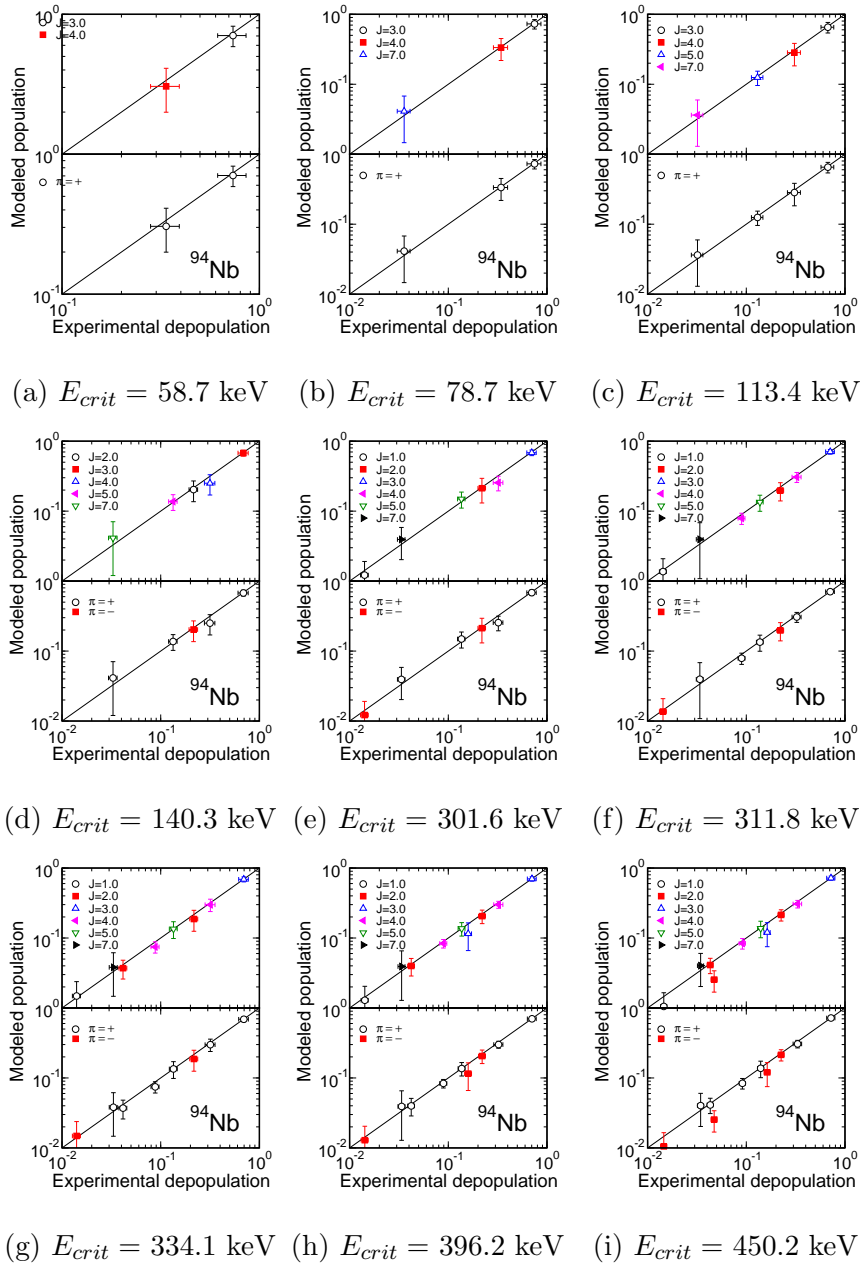
Figure 4.42: Depopulation-population plots for increasing E_{crit} and assuming $J^{\pi}_{CS} = 4^+(75\%) + 5^+(25\%)$.
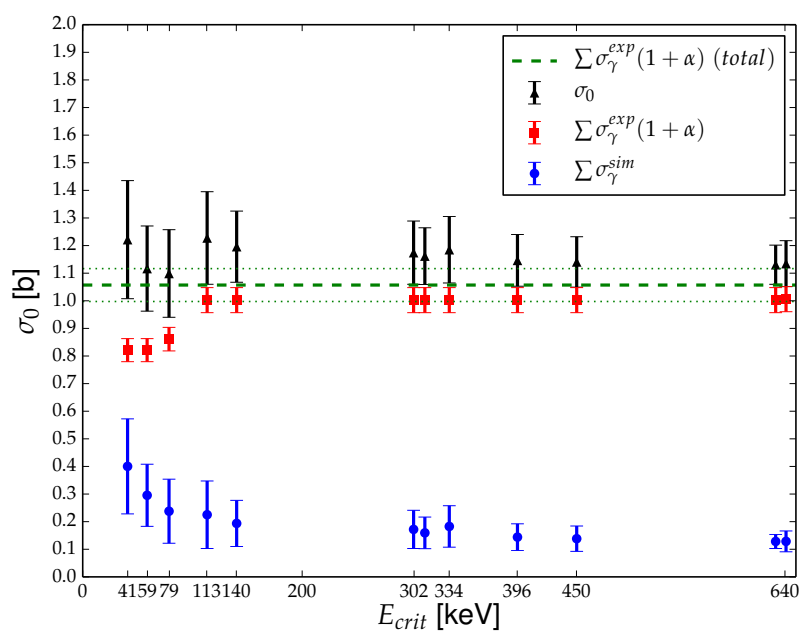
Figure 4.43: Total feeding of the ground state (σ_0) with increasing cut-off energy for the reaction ^{93}Nb(n,γ)^{94}Nb.
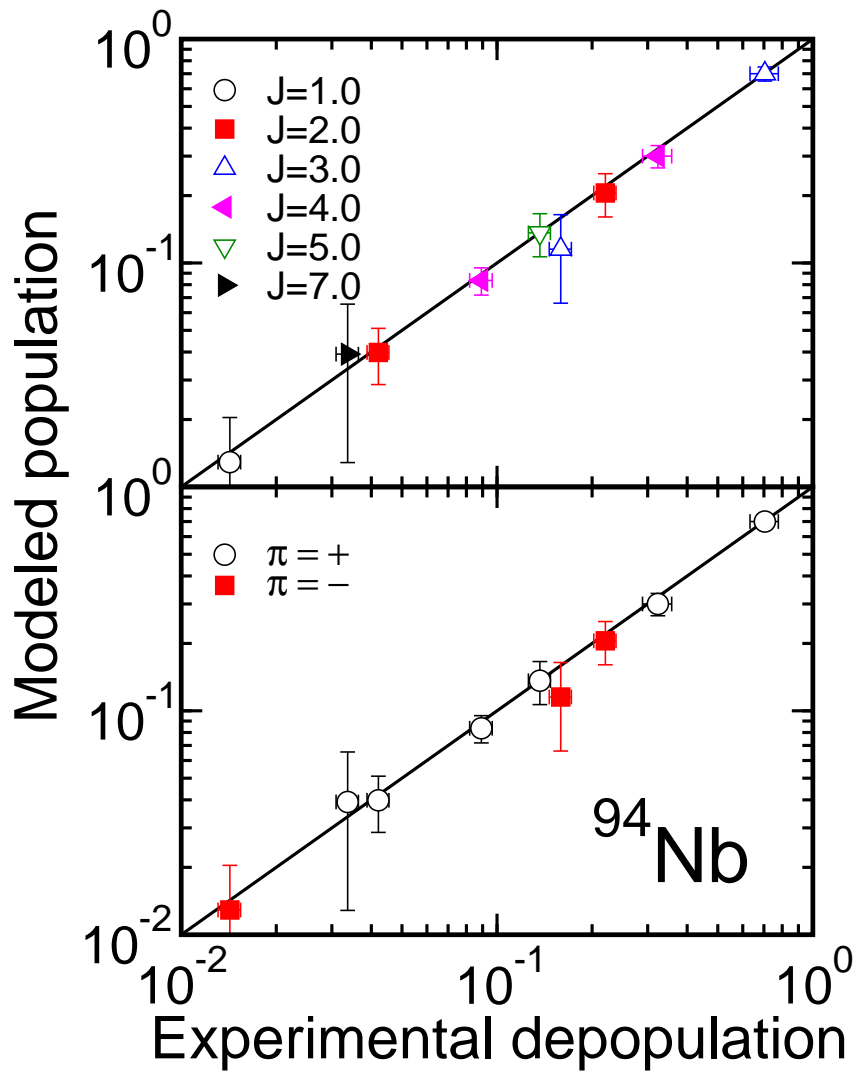
Figure 4.44: Population-depopulation plots with $E_{crit} = 396$ keV and assuming $J_{CS}^{\pi} = 4^{+}(75\%) + 5^{+}(25\%)$.

4.3 High-Resolution Experiment

After finishing the analyses already presented in this work, additional measurements of a new NbCl$_5$ sample and the previously-measured Nb$_2$O$_5$ sample using a low-energy germanium (LeGe) detector with Compton suppression. The experimental setup was the same as the previous experiments with the LeGe detector system in place and the aluminum window with 0.5 mm thickness absent. The efficiency calibration and non-linearity curves for LeGe detector system are shown in Figure 4.45. With the spectrum ranging from 6.5 to 3100 keV and high resolution (0.2% FWHM/E_γ at 436 keV), these measurements had two purposes: 1) measure the low-energy γ-rays that are very important to this work and 2) check the standardization.
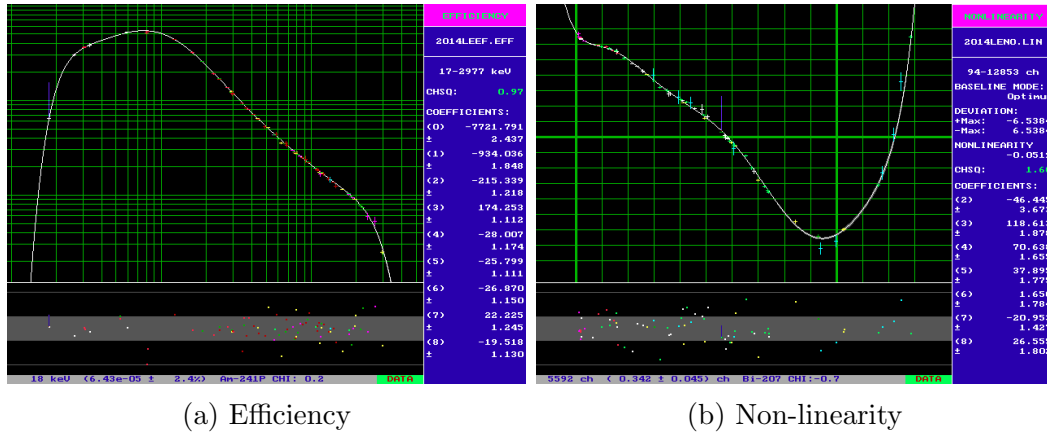

(a) Efficiency (b) Non-linearity

Figure 4.45: The efficiency calibration and non-linearity curves for LeGe detector system.

The NbCl$_5$ sample had a mass of 0.251 g and a thickness of about 2 mm. It was sealed in a Teflon bag and irradiated for 14.7-hours live time. The 255.9-keV peak was again standardized relative to the 1951.1-keV peak from ^{36}Cl. These peaks are

shown in Figure 4.46. The high resolution of the detector system was evident by the complete resolving of the 253.1- and 255.9-keV peaks. The effective thickness for the purpose of γ-ray self-absorption correction was found to be 0.6 mm using the intensity ratios of the 99.4- to 255.9-keV peaks. The standardization σ_γ of the 255.9-keV peak was found to be 0.1406(30) b, which was 2.1% higher than the 0.1377(18) b σ_γ determined with the previous standardization measurement in this work. The average of these statistically-similar results was 0.1392(35) b. The second measurement provides confirmation that the calibration factor is substantially lower than in the previous EGAF.

(a) ^{94}Nb 255.9-keV peak   (b) ^{36}Cl 1951.1-keV peak
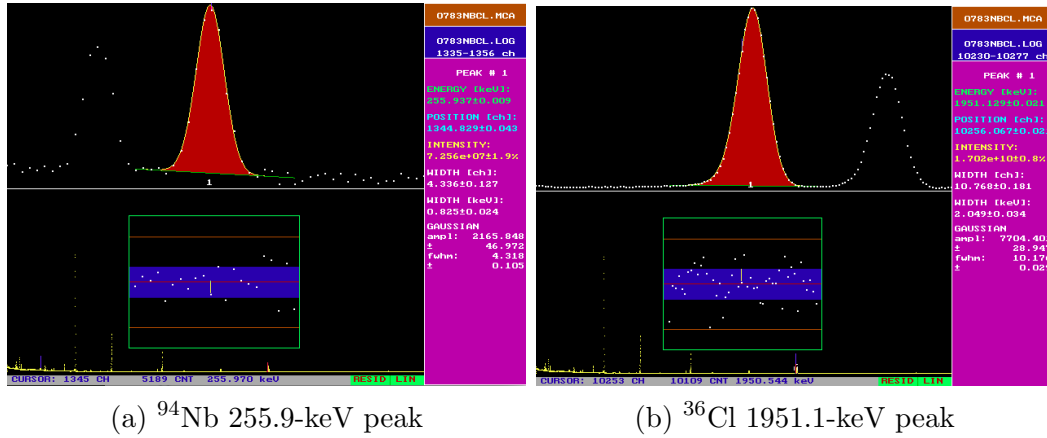
Figure 4.46: The peak fits for the (a) standardization peak from ^{94}Nb and (b) comparator peak from ^{36}Cl

The Nb$_2$O$_5$ sample, as previously described, had a mass of 0.47144 and approximate dimensions of 8 mm $\times$ 24 mm with a thickness less than 1 mm. It was irradiated for 16.7 hours. The low-energy peaks for the 18-, 41- and 55-keV γ-rays – that were previously adopted from normalized ENSDF intensities – were measured in the spectrum. These peaks are shown in Figure 4.47. As seen for the 18- and 55-keV peaks,

the high resolution of the detector was necessary for resolving the peaks from the K x-rays (16.5, 16.6, 18.6 keV) and background peaks (53.5, 56.3 keV), respectively. A nuance was found in fitting the 18-keV peak that arose from Hypermet-PC fitting the 16.5- and 16.6-keV x-ray peaks as a single peak as shown in Figure 4.47(a), and thus applying the FWHM of this dominant peak to the other peaks in the region. Without this peak, as shown in Figure 4.47(b), the FWHM of 17.9-keV peak was lower (0.445 keV versus 0.472 keV). As a result, the peak area was 6.2% lower. The 40.9-keV peak area had 13.1% uncertainty, which reinforced the challenge of a high-precision measurement of the σ_m from the 40.9-keV γ-ray intensity.

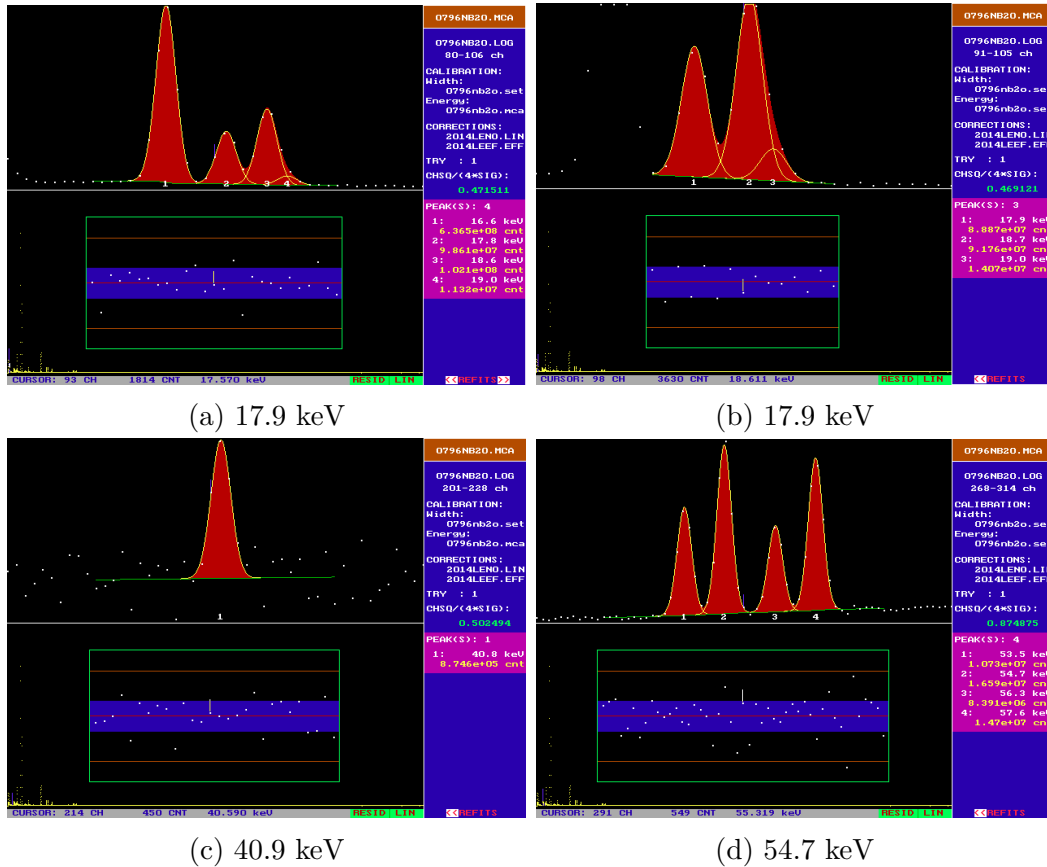(a) 17.9 keV   (b) 17.9 keV

(c) 40.9 keV   (d) 54.7 keV

Figure 4.47: The low-energy peaks in the Nb_2O_5 spectrum measured with the LeGe detector system.

Correcting for γ-ray self-absorption was very important for these low-energy peaks. The effective thickness of the Nb_2O_5 sample was previously estimated to be 0.2 mm. However, the low-energy peaks (18, 41 and 55 keV) were more sensitive to the estimated effective thickness, thus requiring a more finely-tuned estimation of the effective thickness. The effective thickness of the Nb_2O_5 sample was found by iterating it until the low-energy σ_γ agreed with those of ENSDF. Figure 4.48 shows the comparison of the intensities (normalized to the 255.9-keV γ-ray intensity) of the low-energy γ-rays determined in this work and from ENSDF with and without correcting for γ-ray self-absorption. Comparison of the 18-keV γ-ray intensities suggested that the assumption that the ENSDF data were not corrected for γ-ray self-absorption was valid. The ENSDF data were corrected for γ-ray self-absorption with an effective thickness of 0.025 mm, as previously discussed. The 0.22 mm effective thickness for the Nb_2O_5 sample was selected because of the agreement in the 40.9-keV intensity with ENSDF and the previously-determined σ_m. The 18-keV intensity did not produce agreement, but its lower intensity makes it less significant than the 40.9-keV peak.
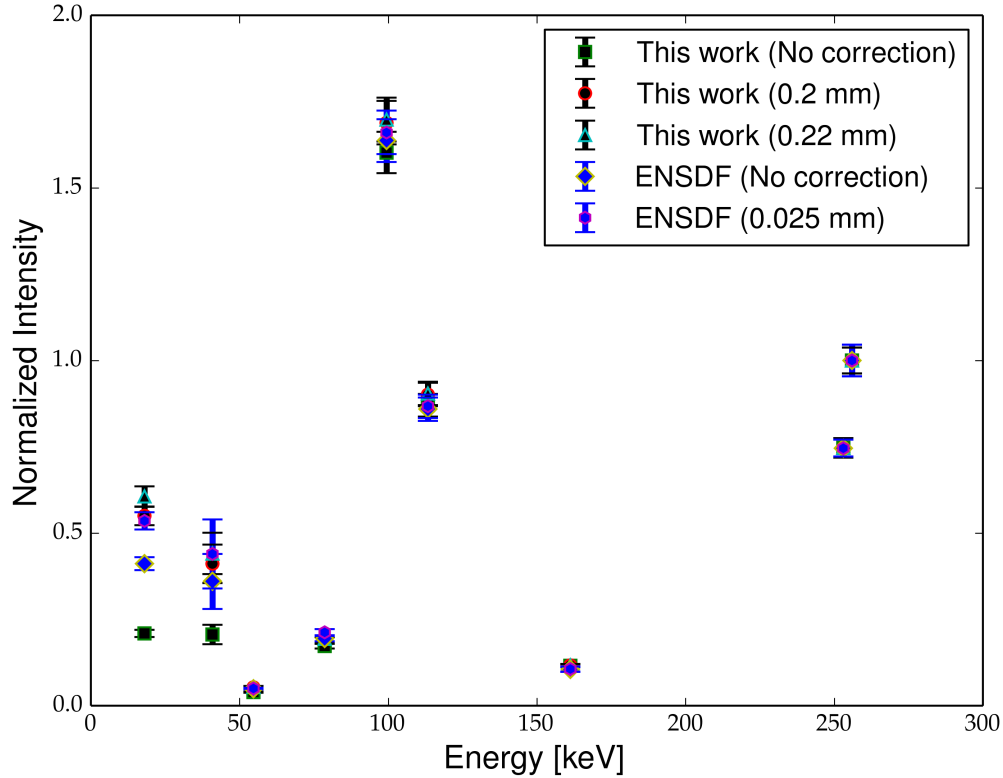
Figure 4.48: Comparison of the intensities (normalized to the 255.9-keV γ-ray intensity) of the low-energy γ-rays determined in this work and from ENSDF with and without γ-ray self-absorption correction. The 40.9-keV intensity was multiplied by 100 to better differentiate the points.

DICEBOX simulations of 50 nuclear realizations consisting of 50,000 cascade events were performed with $E_{crit} = 396\ keV$ with the decay scheme shown in Table 4.17 and the EGLO/CTF model combination. The capture-state spin distribution was assumed, in separate cases, as $J_{CS}^{\pi} = 4^{+}(75\%) + 5^{+}(25\%)$ and $J_{CS}^{\pi} = 4^{+}(90\%) + 5^{+}(10\%)$, producing σ_0 values of 1.18(15) b and 1.14(13) b, respectively. The resulting population-depopulation plots are shown in Figure 4.49. Although these

120

results agree with those in the previous section, more investigation of the effective thickness and capture-state spin distribution is required.

Table 4.17: Experimental γ-ray cross sections measured with the Nb_2O_5 sample using the Compton-suppressed LeGe detector.

E_L [keV] [6]	J^π	E_γ [keV]	σ_γ	α	ML
0.0	6+				
40.891(12)	3^+	40.887(34)	0.00062(8)	1323(19)	M3
58.708(10)	4^+	17.894(6)	0.0840(35)	4.18(6)	M1
78.6683(8)	7^+	78.687(3)	0.02689(73)	0.443(7)	M1
113.4009(8)	5^+	54.705(5)	0.00757(24)	2.05(7)	M1+E2
		113.417(3)	0.1254(33)	0.1597(23)	M1
140.298(12)	2^-	99.414(3)	0.2354(62)	0.1219(17)	E1
301.558(12)	$1^{-\dagger}$	161.253(4)	0.01620(46)	0.0741(23)	M1+E2
311.821(10)	$4^{+\dagger}$	253.119(3)	0.1035(28)	0.030(12)	M1,E2
334.102(12)	$2^{+\dagger}$	293.218(4)	0.0495(13)	0.0129(2)	M1
396.227(12)	3^-	255.934(3)	0.1387(37)	0.0212(3)	M1+E2
		337.569(6)	0.0443(12)	0.00377(6)	E1
		355.357(16)	0.00443(12)	0.00329(5)	[E1]

† Assignment made on the basis of statistical model calculations with DICEBOX.
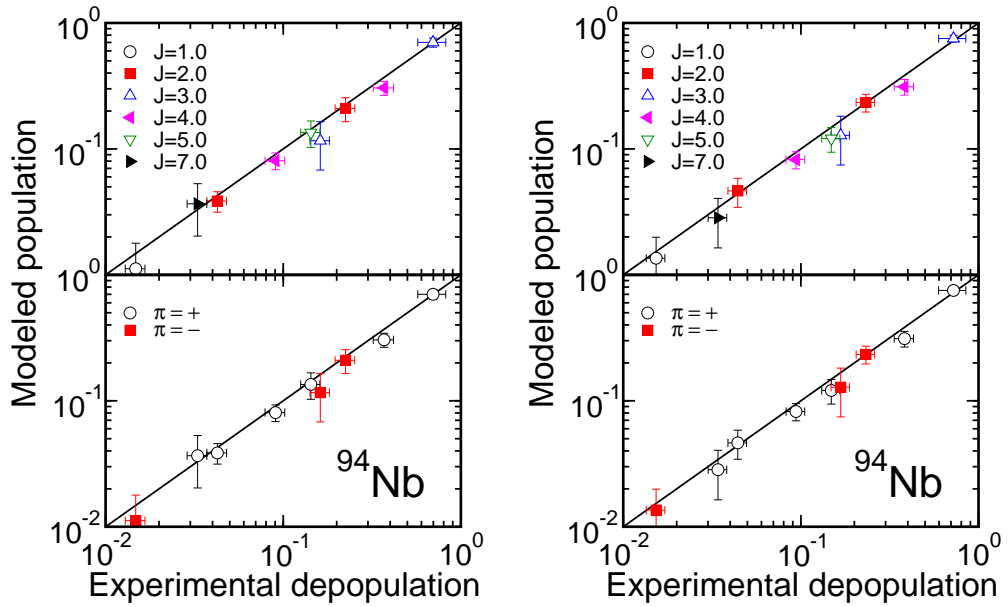
(a) $J^{\pi}_{CS} = 4^+(75\%) + 5^+(25\%)$ (b) $J^{\pi}_{CS} = 4^+(90\%) + 5^+(10\%)$

Figure 4.49: Population-depopulation plots for $E_{crit} = 396.2$ keV performed using the decay scheme in Table 4.17, the EGLO/CTF model combination and assuming the capture-state spin distribution is $J^{\pi}_{CS} = 4^+(75\%) + 5^+(25\%)$ and $J^{\pi}_{CS} = 4^+(90\%) + 5^+(10\%)$.

CHAPTER 5

CONCLUSIONS AND FUTURE WORK

5.1 Conclusions

The statistical model calculations with DICEBOX were insightful in evaluation of the ^{93}Nb(n,γ) prompt γ-ray data measured in this work and the ^{94}Nb nuclear structure. For tentative spin assignments of low-lying ^{94}Nb excited states, comparison of the modeled population and experimental depopulation confirmed assignments and suggested changes for several levels:

- Confirmation of spin assignments of the low-lying positive-parity multiplet and the suggestion that the 334.1-keV level, previously $J^\pi = 3^+$, is the $J^\pi = 2^+$ member;

- The 301.6-keV level, previously $J^\pi = (2)^-$, is suggested to be $J^\pi = 1^-$ and form a doublet with the 140.3-keV level with J^π confirmed as 2^-;

- $J^\pi = 4^+$ produced better agreement than 5^+ in population-depopulation for the 311.8-keV level that was previously $J^\pi = (4, 5)^+$.

From this work, the decay scheme up to the ninth excited state at 396 keV produced a consistent population-depopulation plot and is proposed to be complete, which includes eight more levels than RIPL currently recommends.

The thermal-neutron cross sections were deduced for the ^{93}Nb(n,γ)^{94m}Nb and ^{93}Nb(n,γ)^{94g}Nb reactions using the Prompt γ-ray Neutron Activation Method. The (1.16 $\pm$ 11) b σ_0 agreed with literature values. Although this σ_0 value lacks the precision of previous measurements, the agreement with literature supports the calibration factor measured with NbCl$_5$ internal standardization in this work that is 23% lower than previously measured for EGAF. Despite being the strongest transition, the γ-ray intensity for the transition from the metastable state to the ground is difficult to experimentally measure because internal conversion dominates the decay. The σ_m, previously unmeasured, was determined to be (0.83 $\pm$ 0.05) b using the PGNAM method. The unknown capture-state spin distribution of ^{93}Nb neutron capture hindered the application of PGNAM to the measurement of the σ_0 and σ_m because these results show minor variation with the assumed capture-state spin distribution. Although final results were obtained with $J_{CS}^{\pi} = 4^+(75\%) + 5^+(25\%)$, this work suggested that $J_{CS}^{\pi} = 4^+$ constitutes $\geq 75\%$ of the capture-state.

The decay-scheme improvements suggested in this work will be used to improve the ENSDF nuclear-structure evaluations that contribute to the RIPL nuclear-reaction database. The new thermal-capture (n,γ) data will be added to the EGAF database and will also be used to help produce a more extensive and complete thermal capture γ-ray library for the ENDF neutron-data library.

5.2   Future Work

For the final EGAF, the full-energy and low-energy spectra of the Nb$_2$O$_5$ sample need to be integrated. The peak area uncertainty for the 40.9-keV γ-ray in the low-energy spectrum was 13.1%; the PGNAM could be applied to determine the σ_m and the corresponding σ_γ for this transition, as it was for the full-energy spectrum. Given the

sensitivity of the low-energy γ-rays to the estimated effective thickness, a niobium-metal foil with 0.025 mm thickness is recommended as the target to minimize the γ-ray self-absorption and provide a defined geometry for its correction. The caveat is that there is significant trade off in peak count rate with the reduced mass, which is important for a low cross section isotope like ^{93}Nb. Because of this, the measurement should be preformed in a high-flux PGNAA facility, such as the one at the Garching FRM II research reactor or the one being upgraded at the National Institute of Standards and Technology Center for Neutron Research, in order to maximize the signal-to-noise ratio. The detector must be a high-resolution γ-ray spectrometer, such as the low-energy germanium detector tested in this work, in order to resolve the low-energy γ-rays from the internal conversion x-rays and background peaks. Additionally, γ-γ coincidence data will be beneficial in improving the decay scheme for levels above 800 keV.

BIBLIOGRAPHY

[1] T. von Egidy and D. Bucurescu, "Systematics of nuclear level density parameters," *Physical Review C*, vol. 72, no. 4, p. 044311, 2005.

[2] IAEA, "Reference neutron activation library (RNAL)."

[3] R. Lindstrom and Z. Revay, "Beams and facilities," in *Handbook of Prompt Gamma Activation Analysis with Neutron Beams* (G. Molnar, ed.), ch. 2, Kluwer Academic Publishers, 2004.

[4] H. Choi, R. Firestone, R. Lindstrom, G. L. Molnár, S. Mughabghab, Z. Revay, A. Trkov, V. Zerkin, and C. Zhou, *Database of prompt gamma rays from slow neutron capture for elemental analysis.* International Atomic Energy Agency, 2007.

[5] T. Belgya, Z. Kis, and L. Szentmiklósi, "Neutron flux characterization of the cold beam PGAA-NIPS facility at the budapest research reactor," *Nuclear Data Sheets*, vol. 119, no. 0, pp. 419 – 421, 2014.

[6] A. D and S. AA, "Nuclear data sheets for A = 94," *Nuclear Data Sheets*, vol. 107, pp. 2423–2578, 2006.

[7] Z. Révay and G. Molnár, "Standardisation of the prompt gamma activation analysis method," *Radiochimica Acta*, vol. 91, no. 6, pp. 361–369, 2003.

[8] R. Firestone, G. Molnar, Z. Revay, T. Belgya, D. McNabb, and B. Sleaford, "The evaluated gamma-ray activation file (EGAF)," *International Conference on Nuclear Data for Science and Technology*, 2004.

[9] E. N. S. D. F. ENSDF, "maintained by the national nuclear data center at brookhaven national laboratory, published in nuclear data sheets."

[10] A. Hurst, R. Firestone, N. Summers, B. Sleaford, Z. Revay, M. Krtička, T. Belgya, M. Basunia, R. Capote, H. Choi, *et al.*, "Data evaluation methods and improvements to the neutron-capture γ-ray spectrum," in *SECOND INTERNATIONAL ULAANBAATAR CONFERENCE ON NUCLEAR PHYSICS AND APPLICATIONS*, vol. 1342, pp. 24–31, AIP Publishing, 2011.

[11] R. Capote, M. Herman, P. Obložinský, P. Young, S. Goriely, T. Belgya, A. Ignatyuk, A. J. Koning, S. Hilaire, V. A. Plujko, *et al.*, "RIPL–reference input parameter library for calculation of nuclear reactions and nuclear data evaluations," *Nuclear Data Sheets*, vol. 110, no. 12, pp. 3107–3214, 2009.

[12] M. Chadwick, P. Obložinský, M. Herman, N. Greene, R. McKnight, D. Smith, P. Young, R. MacFarlane, G. Hale, S. Frankle, *et al.*, "Endf/b-vii. 0: Next generation evaluated nuclear data library for nuclear science and technology," *Nuclear data sheets*, vol. 107, no. 12, pp. 2931–3060, 2006.

[13] B. Sleaford, R. Firestone, N. Summers, and J. Escher, "Improved capture gamma-ray libraries for nuclear applications," *Bulletin of the American Physical Society*, vol. 57, 2012.

[14] F. Becvar, "Simulation of γ cascades in complex nuclei with emphasis on assessment of uncertainties of cascade-related quantities," *Nuclear Instruments and Methods in Physics Research Section A: Accelerators, Spectrometers, Detectors and Associated Equipment*, vol. 417, no. 2, pp. 434–449, 1998.

[15] M. Krtička, R. Firestone, D. McNabb, B. Sleaford, U. Agvaanluvsan, T. Belgya, and Z. Revay, "Thermal neutron capture cross sections of the palladium isotopes," *Physical Review C*, vol. 77, no. 5, p. 054615, 2008.

[16] C. Porter and R. Thomas, "Fluctuations of nuclear reaction widths," *Physical Review*, vol. 104, no. 2, p. 483, 1956.

[17] A. Borella, T. Belgya, S. Kopecky, F. Gunsing, M. Moxon, M. Rejmund, P. Schillebeeckx, and L. Szentmiklosi, "Determination of the ^{209}Bi(n,γ)^{210m,g}Bi reaction cross sections in a cold neutron beam," *Nuclear Physics A*, vol. 850, pp. 1–21, 2011.

[18] R. Firestone, M. Krtička, Z. Révay, L. Szentmiklosi, and T. Belgya, "Thermal neutron capture cross sections of the potassium isotopes," *Physical Review C*, vol. 87, no. 2, p. 024605, 2013.

[19] A. Hurst, R. Firestone, B. Sleaford, N. Summers, Z. Révay, L. Szentmiklósi, M. Basunia, T. Belgya, J. Escher, and M. Krtička, "Investigation of the tungsten isotopes via thermal neutron capture," *Physical Review C*, vol. 89, no. 1, p. 014606, 2014.

[20] M. Basunia, R. Firestone, Z. Révay, H. Choi, T. Belgya, J. Escher, A. Hurst, M. Krtička, L. Szentmiklósi, B. Sleaford, *et al.*, "Determination of the $^{151}Eu(n,\gamma)^{152m1,g}Eu$ and $^{153}Eu(n,\gamma)^{154}Eu$ reaction cross sections at thermal neutron energy," *Nuclear Data Sheets*, vol. 119, pp. 88–90, 2014.

[21] H. Choi, R. Firestone, M. Basunia, A. Hurst, B. Sleaford, N. Summers, J. Escher, Z. Révay, L. Szentmiklósi, T. Belgya, *et al.*, "Radiative capture cross sections of ^{155,157}Gd for thermal neutrons," *NUCLEAR SCIENCE AND ENGINEERING*, vol. 177, no. 219-232, 2014.

[22] A. G. Lerch, "Nuclear structure of rhenium-186 revealed by neutron-capture gamma rays," tech. rep., DTIC Document, 2014.

[23] A. Nikulina, "Zirconium-niobium alloys for core elements of pressurized water reactors," *Metal science and heat treatment*, vol. 45, no. 7-8, pp. 287–292, 2003.

[24] R. D. Mariani, J. I. Cole, and A. Aitkaliyeva, "A novel Zr-1Nb alloy and a new look at hydriding," tech. rep., Idaho National Laboratory (INL), 2013.

[25] D. Goldberg, G. Dicker, and S. Worcester, "Niobium and niobium alloys in nuclear power," *Nuclear Engineering and Design*, vol. 22, no. 1, pp. 124 – 137, 1972.

[26] V. Likhanskii, I. Evdokimov, T. Aliev, V. Kon'kov, V. Markelov, V. Novikov, and T. Khokhunova, "Corrosion model for zirconium-niobium alloys in pressurized water reactors," *Atomic Energy*, vol. 116, no. 3, pp. 186–193, 2014.

[27] R. D. Mariani, P. Medvedev, D. L. Porter, S. L. Hayes, J. I. Cole, and X.-M. Bai, "Novel accident-tolerant fuel meat and cladding," tech. rep., Idaho National Laboratory (INL), 2013.

[28] S. Mughabghab, *Atlas of Neutron Resonances*. Elsevier, 5 ed., 2006.

[29] U. Gruber, R. Koch, B. Maier, O. Schult, J. Ball, K. Bhatt, and R. K. Sheline, "Energies and character of low-lying levels in ^{94}Nb," *Nuclear Physics*, vol. 67, no. 2, pp. 433–442, 1965.

[30] E. Jurney, H. Motz, R. Sheline, E. Shera, and J. Vervier, "Energy levels and configurations in ^{94}Nb," *Nuclear Physics A*, vol. 111, no. 1, pp. 105–128, 1968.

[31] M. Bogdanović, H. Seyfarth, H. Börner, S. Kerr, F. Hoyler, K. Schreckenbach, and G. Colvin, "Low-lying states of ^{94}Nb," in *Capture Gamma-Ray Spectroscopy and Related Topics-1984: 5th International Symposium*, vol. 125, pp. 382–385, AIP Publishing, 1985.

[32] R. Chrien, K. Rimawi, and J. Garg, "Resonance neutron capture in ^{93}Nb," *Physical Review C*, vol. 3, no. 5, p. 2054, 1971.

[33] T. Kennett, W. Prestwich, and J. Tsai, "Energy levels of ^{94}Nb populated directly via the (n, γ) reaction," *Canadian Journal of Physics*, vol. 66, no. 11, pp. 947–959, 1988.

[34] R. K. Sheline, R. T. Jernigan, J. B. Ball, K. H. Bhatt, Y. E. Kim, and J. Vervier, "The ^{93}Nb(d, p)^{94}Nb reaction and the low-lying states of ^{94}Nb," *Nuclear Physics*, vol. 61, no. 2, pp. 342–351, 1965.

[35] E. Hagen, B. Kern, F. Snyder, and D. Miracle, "Low-lying levels of ^{94}Nb," *Physical Review C*, vol. 13, no. 2, p. 620, 1976.

[36] I. D. Fedorets, V. M. Mishchenko, A. I. Popov, and V. E. Storizhko, "The differential cross sections of the ^{94}Zr(p, n)^{94}Nb reaction," *Izv.Akad.Nauk*, vol. SSSR, pp. Ser.Fiz. 41, 1665, 1977.

[37] N. Marginean, D. Bucurescu, G. Cata-Danil, I. Cata-Danil, M. Ivascu, and C. Ur, "High-spin states in the ^{94}Nb nucleus," *Physical Review C*, vol. 62, no. 3, p. 34309, 2000.

[38] Z. Revay, R. Firestone, T. Belgya, and G. Molnar, "Prompt gamma-ray spectrum catalog," in *Handbook of Prompt Gamma Activation Analysis with Neutron Beams* (G. Molnar, ed.), ch. 7, Kluwer Academic Publishers, 2004.

[39] Z. Revay and T. Belgya, "Principles of the pgaa method," in *Handbook of Prompt Gamma Activation Analysis with Neutron Beams* (G. Molnar, ed.), ch. 1, Kluwer Academic Publishers, 2004.

[40] W. D. Loveland, D. J. Morrissey, and G. T. Seaborg, *Modern nuclear chemistry*. John Wiley & Sons, 2005.

[41] T. Kibédi, T. Burrows, M. Trzhaskovskaya, P. M. Davidson, and C. Nestor Jr, "Evaluation of theoretical conversion coefficients using *BrIcc*," *Nuclear Instruments and Methods in Physics Research Section A: Accelerators, Spectrometers, Detectors and Associated Equipment*, vol. 589, no. 2, pp. 202–229, 2008.

[42] R. Lindstrom, "Using k_0 in pgaa: Perspectives," *Journal of Radioanalytical and Nuclear Chemistry*, vol. 257, no. 3, pp. 557–560, 2003.

[43] A. Couet, A. T. Motta, R. J. Comstock, and R. L. Paul, "Cold neutron prompt gamma activation analysis, a non-destructive technique for hydrogen level assessment in zirconium alloys," *Journal of Nuclear Materials*, vol. 425, no. 1, pp. 211–217, 2012.

[44] I. Meric, G. A. Johansen, M. B. Holstad, J. Wang, and R. P. Gardner, "Produced water characterization by prompt gamma-ray neutron activation analysis," *Measurement Science and Technology*, vol. 22, no. 12, p. 125701, 2011.

[45] A. Buffler and J. Tickner, "Detecting contraband using neutrons: challenges and future directions," *Radiation Measurements*, vol. 45, no. 10, pp. 1186–1192, 2010.

[46] T. Schmitz, K. Appelman, P. Kudejova, C. Schütz, J. Kratz, R. Moss, G. Otto, and G. Hampel, "Determination of boron concentration in blood and tissue samples from patients with liver metastases of colorectal carcinoma using prompt gamma ray activation analysis (PGAA)," *Applied Radiation and Isotopes*, vol. 69, no. 7, pp. 936–941, 2011.

[47] J. Gräfe, F. McNeill, S. Byun, D. Chettle, and M. Noseworthy, "The feasibility of in-vivo detection of gadolinium by prompt gamma neutron activation analysis following gadolinium-based contrast-enhanced mri," *Applied Radiation and Isotopes*, vol. 69, no. 1, pp. 105–111, 2011.

[48] J. Gräfe, F. McNeill, D. Chettle, and S. Byun, "Characteristic x ray emission in gadolinium following neutron capture as an improved method of *in vivo* measurement: A comparison between feasibility experiment and monte–carlo simulation," *Nuclear Instruments and Methods in Physics Research Section B: Beam Interactions with Materials and Atoms*, vol. 281, pp. 21–25, 2012.

[49] G. Szakmány, Z. Kasztovszky, V. Szilágyi, E. Starnini, O. Friedel, and K. T. Biró, "Discrimination of prehistoric polished stone tools from hungary with non-destructive chemical prompt gamma activation analyses (pgaa)," *European Journal of Mineralogy*, vol. 23, no. 6, pp. 883–893, 2011.

[50] L. Groshev, A. Demidov, V. Lutsenko, and V. Pelekhov, "Atlas of the spectra of gamma rays from the radiative capture of thermal neutrons," 1961.

[51] G. Bartholomew, A. Doveika, K. Eastwood, S. Monaro, L. Groshev, A. Demidov, V. Pelekhov, and L. Sokolovskii, "Compendium of thermal-neutron-capture γ-ray measurements Part I Z $\leq$ 46," *Nuclear Data Sheets. Section A*, vol. 3, no. 4, pp. 367–645, 1967.

[52] R. C. Greenwood and J. Reed, "Prompt gamma rays from radiative capture of thermal neutrons. volumes 1 and 2. final report.," tech. rep., IIT Research Inst., Chicago, Ill., 1965.

[53] N. C. Rasmussen, Y. Hukai, T. Inouye, and V. J. Orphan, "Thermal neutron capture gamma-ray spectra of the elements," tech. rep., DTIC Document, 1969.

[54] V. Orphan, N. C. Rasmussen, and T. Harper, "Line and continuum gamma-ray yields from thermal-neutron capture in 75 elements.," tech. rep., DTIC Document, 1970.

[55] M. Lone, R. Leavitt, and D. Harrison, "Prompt gamma rays from thermal-neutron capture," *Atomic Data and Nuclear Data Tables*, vol. 26, no. 6, pp. 511–559, 1981.

[56] R. C. Reedy and S. C. Frankle, "Prompt gamma rays from radiative capture of thermal neutrons by elements from hydrogen through zinc," *Atomic data and nuclear data tables*, vol. 80, no. 1, pp. 1–34, 2002.

[57] R. Firestone, K. Abusaleem, M. Basunia, F. Bečvář, T. Belgya, L. Bernstein, H. Choi, J. Escher, C. Genreith, A. Hurst, *et al.*, "EGAF: Measurement and analysis of gamma-ray cross sections," *Nuclear Data Sheets*, vol. 119, pp. 79–87, 2014.

[58] J. Vervier, "Effective nucleon-nucleon interactions in the Y, Zr, Nb, Mo and Tc isotopes," *Nuclear Physics*, vol. 75, no. 1, pp. 17–78, 1966.

[59] T. Haste and B. Thomas, "Investigations of resonance capture γ-ray spectra in the ^{93}Nb(n, γ)^{94}Nb reaction," *Journal of Physics G: Nuclear Physics*, vol. 1, no. 9, p. 967, 1975.

[60] "Hypermet-pc version 5.01 (v512)," (1995-1997).

[61] G. W. Phillips and K. W. Marlow, "Automatic analysis of gamma-ray spectra from germanium detectors," *Nuclear Instruments and Methods*, vol. 137, no. 3, pp. 525–536, 1976.

[62] T. Belgya and Z. Revay, "Gamma-ray spectrometry," in *Handbook of Prompt Gamma Activation Analysis with Neutron Beams* (G. Molnar, ed.), ch. 4, Kluwer Academic Publishers, 2004.

[63] R. Lindstrom and C. Yonezawa, "Samples and standards," in *Handbook of Prompt Gamma Activation Analysis with Neutron Beams* (G. Molnar, ed.), ch. 3, Kluwer Academic Publishers, 2004.

[64] J. H. Hubbell and S. M. Seltzer, "Tables of x-ray mass attenuation coefficients and mass energy-absorption coefficients," *National Institute of Standards and Technology*, 1996.

[65] G. Sun, S. Byun, and H. Choi, "Prompt k_0-factors and relative gamma-emission intensities for the strong non-1/v absorbers ^{113}Cd, ^{149}Sm, ^{151}Eu and ^{155,177}Gd," *Journal of Radioanalytical and Nuclear Chemistry*, vol. 256, no. 3, pp. 541–552, 2003.

[66] N. Bohr, "Neutron capture and nuclear constitution," *Nature*, vol. 137, no. 3461, pp. 344–348, 1936.

[67] A. Gilbert and A. Cameron, "A composite nuclear-level density formula with shell corrections," *Canadian Journal of Physics*, vol. 43, no. 8, pp. 1446–1496, 1965.

[68] T. Newton, "Shell effects on the spacing of nuclear levels," *Canadian Journal of Physics*, vol. 34, no. 8, pp. 804–829, 1956.

[69] J. Dobaczewski, P. Magierski, W. Nazarewicz, W. Satuła, and Z. Szymański, "Odd-even staggering of binding energies as a consequence of pairing and mean-field effects," *Physical Review C*, vol. 63, no. 2, p. 024308, 2001.

[70] D. Brink, "Some aspects of the interaction of fields with matter'," *D. Ph. Thesis, Oxford*, 1955.

[71] P. Axel, "Electric dipole ground-state transition width strength function and 7-mev photon interactions," *Physical Review*, vol. 126, no. 2, p. 671, 1962.

[72] C. M. McCullagh, M. L. Stelts, and R. E. Chrien, "Dipole radiative strength functions from resonance neutron capture," *Physical Review C*, vol. 23, no. 4, p. 1394, 1981.

[73] J. Speth and A. van der Woude, "Giant resonances in nuclei," *Reports on Progress in Physics*, vol. 44, no. 7, p. 719, 1981.

[74] J. Kopecky and M. Uhl, "Test of gamma-ray strength functions in nuclear reaction model calculations," *Physical Review C*, vol. 41, no. 5, p. 1941, 1990.

[75] A. Lepretre, H. Beil, R. Bergere, P. Carlos, A. Veyssiere, and M. Sugawara, "The giant dipole states in the A = 90 mass region," *Nuclear Physics A*, vol. 175, no. 3, pp. 609–628, 1971.

[76] S. S. Dietrich and B. L. Berman, "Atlas of photoneutron cross sections obtained with monoenergetic photons," *Atomic Data and Nuclear Data Tables*, vol. 38, no. 2, pp. 199–338, 1988.

[77] J. Tuli, "Nuclear data sheets update for A = 94," *Nuclear Data Sheets*, vol. 66, no. 1, pp. 1–67, 1992.

[78] A. Abzouzi, M. Antony, V. N. Ndongué, and D. Oster, "Redetermination of several half-lives," *Journal of Radioanalytical and Nuclear Chemistry*, vol. 145, no. 5, pp. 361–368, 1990.

[79] P. Kilian, H. Langhoff, and A. Flammersfeld, "Der zerfall von ^{94m}Nb," *Zeitschrift für Physik*, vol. 169, no. 1, pp. 23–31, 1962.

[80] C. Yonezawa, "Quantitative analysis," in *Handbook of Prompt Gamma Activation Analysis*, pp. 113–135, Springer, 2004.

[81] L. Seren, H. N. Friedlander, and S. H. Turkel, "Thermal neutron activation cross sections," *Physical Review*, vol. 72, no. 10, p. 888, 1947.

[82] F. Colmer and D. Littler, "Pile neutron absorption cross sections of some of the elements," *Proceedings of the Physical Society. Section A*, vol. 63, no. 10, p. 1175, 1950.

[83] R. Tattersall, H. Rose, S. Pattenden, and D. Jowitt, "Pile oscillator measurements of resonance absorption integrals," *Journal of Nuclear Energy. Part A. Reactor Science*, vol. 12, no. 1, pp. 32–46, 1960.

[84] R. Druschel and J. Halperin, "The thermal neutron capture cross sections and resonance integrals of ^{93}nb and ^{94}nb," *Oak Ridge National Laboratory Reports No. 4306*, p. 2, 1968.

[85] R. Schuman, "Activation cross sections of Nb-93 and Nb-94," *Washington AEC Office Reports No.1136*, p. 52, 1969.